

UNIVERSITÉ LIBRE DE BRUXELLES
Faculté des sciences appliquées
Service d'optique non linéaire théorique

Nonlinear aspects of the dynamics induced by dissipative light-matter interaction

Promoteur de thèse :
Paul MANDEL

Année académique 2000-2001

Dissertation originale
présentée par Gregory KOZYREFF
en vue de l'obtention du grade
de docteur en sciences appliquées

© 2001, Gregory KOZYREFF

Cet ouvrage peut être copié et transmis librement pour autant que cette notice soit conservée, qu'aucune modification ne soit apportée au texte ou aux figures et que sa diffusion ne génère aucun profit matériel.

À ma grand-mère.

Remerciements

J'exprime ma profonde gratitude envers le professeur Paul MANDEL pour m'avoir offert de préparer un doctorat au sein du groupe d'Optique nonlinéaire théorique. Ayant fait mon travail de fin d'études sous sa direction, je connaissais déjà ses qualités d'écoute et de rigueur intellectuelle. J'avais déjà pu apprécier aussi l'étendue et la solidité de ses connaissances scientifiques. Au cours de notre travail sur le laser LNP, j'ai pu constater sa remarquable aptitude à en dégager les aspects essentiels et à recourir à un traitement mathématique à la fois précis et souple. D'autre part, à chaque occasion, il m'a poussé à collaborer avec d'autres chercheurs, encouragé à participer à des conférences et inscrit à des écoles doctorales. Dans le même esprit, il m'a permis sans hésiter d'aller poursuivre une collaboration d'un mois à Saint-Pétersbourg. Je suis très conscient qu'il a eu à cœur de me faire connaître ainsi les multiples facettes du métier de chercheur et je lui en suis extrêmement reconnaissant. Je salue aussi en lui l'homme de culture, toujours prêt à partager ses découvertes et impressions (notamment comme spécialiste en chocolat), toujours prêt aussi à converser sur quelque sujet que ce soit.

Mes recherches ont croisé celles de Thomas ERNEUX à propos du laser avec absorbant saturable. Au cours de cette collaboration, Thomas m'a sans cesse étonné par son inventivité. En abordant directement certains problèmes mathématiques avec moi, il m'a appris beaucoup plus que je ne l'aurais fait en compulsant les livres. Je retiens aussi les encouragements qu'il m'a prodigués au long de ce travail, ainsi que sa franchise, qui m'a évité de commettre des erreurs dans certains cas. Malgré les activités si nombreuses qu'il mène de front, Thomas s'est toujours montré disponible pour m'aider à effectuer des démarches administratives, à rédiger des projets ou à résoudre des difficultés d'ordre mathématique.

Je remercie Andreï VLADIMIROV d'avoir accepté d'étudier avec Paul MANDEL et moi-même la question des lasers couplés. Partageant le même bureau, Andreï et moi échangions continuellement nos idées, et de préférence sur le mode dialectique. Aussi, nos débats enflammés ont-ils dû traverser plus d'une fois les minces cloisons de notre local. Ces moments furent pour moi parmi les meilleurs et les plus stimulants de mon doctorat (et je souligne ici l'indulgence de mes voisins de couloir). Outre la qualité irréprochable de ses recherches, j'ai apprécié le calme d'Andreï et sa générosité de caractère. Avec le même ton franc et direct, Evgueni (Jenya) VIKTOROV m'a permis de mieux comprendre le fonctionnement des lasers, en particulier du laser LNP. Par ailleurs, je voudrais remercier encore Jenya et Andreï, ainsi que Sonia VLADIMIROV pour l'attention dont ils m'ont entouré lors de mon séjour à Saint-Pétersbourg.

Le professeur Paul MANDEL et moi-même avons eu aussi le plaisir de collaborer avec Rustem SHAKHMURATOV, Jos ODEURS et Romain COUSSEMENT, attachés à l'Instituut voor Kern- en Stralingsphysica. Sur proposition de Rustem, nous avons étudié un schéma électro-nucléaire d'interaction lumière-matière. Il en est résulté une confrontation de points de

vue entre physiciens de spécialités différentes. Plus tard, ce travail a bénéficié du regard pragmatique du spécialiste en télécommunications, Patrice MÉGRET. Je remercie Rustem SHAKHMURATOV d'avoir donné l'impulsion première à cette recherche, qui a été couronnée de succès.

J'ai une énorme dette envers Didier PIEROUX pour la somme des petits gestes qu'il a eus tout au long de son passage dans le groupe ONT. Je le remercie de sa gentillesse et des multiples coups de pouces qu'il m'a fournis en informatique. J'ai toujours trouvé en lui, comme en Mustapha TLIDI et Michel NIZETTE des interlocuteurs scientifiques de haut niveau. En particulier, Michel m'a prêté son aide pour retrouver la solution d'une équation de propagation du dernier chapitre. Je remercie aussi Igor KORYUKIN des entretiens intéressants que nous avons eus sur le modèle TSD⁺.

Je suis reconnaissant à Kenju OTSUKA de m'avoir communiqué sans détour de précieux renseignements expérimentaux relatifs au laser LNP.

Par leur convivialité et leur humour, les membres du Service de physique théorique et mathématique ont assuré une excellente ambiance dans notre couloir et notamment dans la « salle-café ». Je tiens aussi à reconnaître la compétence et la disponibilité de notre secrétaire Fabienne DE NEYN. Par sa gestion rigoureuse des affaires courantes du service, elle ne laissait qu'un minimum de tracas nous atteindre tandis que nous voguions dans l'espace éthétré de la physique théorique.

Ce mémoire n'aurait jamais eu la forme qu'on lui voit sans le concours efficace de Pascal KOCKAERT. Par son habileté au traitement de texte LATEX, il en a rendu la présentation agréable et confortable pour les yeux. Il a aussi grandement contribué à la clarté de l'exposé qui suit par la lecture attentive et critique qu'il en a faite. Je lui suis très obligé de la générosité avec laquelle il m'a donné de son temps. En outre, Pascal n'a cessé de m'offrir l'exemple d'une démarche scientifique honnête, humble et réellement efficace : c'est de cela que je lui suis le plus reconnaissant.

Je remercie Michel HESSE de son agréable compagnie et des nombreuses discussions que nous avons eues durant les pauses du déjeuner. Par leurs conversations aussi, les membres et amis du Service d'optique et acoustique ont largement enrichi ma connaissance des phénomènes lumineux dans les fibres.

La présente thèse et les collaborations dont elle est le fruit n'auraient jamais eu lieu sans le financement procuré par le Pôle d'attraction inter-universitaire du Gouvernement belge.

Enfin, je remercie de tout cœur ma famille et mes amis de leur soutien et de leur présence à mes côtés.

Contents

Remerciements	i
1 Introduction	1
2 Lasers with a weakly saturable absorber	7
2.1 Introduction	7
2.2 Pulse generation by saturable losses	8
2.3 Size of the bifurcation layer	12
2.4 From harmonic to strongly pulsating oscillations	14
2.5 Shape of the intensity pulse	17
2.6 Conclusion	19
2.A The Lotka-Volterra equations	23
2.B Derivation of the solvability condition	23
2.C Asymptotic matching for the pulse	24
2.C.1 Matching first and second segments	25
2.C.2 Matching second and third segments	26
2.C.3 Matching third and last segment	26
References	27
3 Solid state lasers with spatially distributed gain	29
3.1 Introduction	29
3.2 Derivation of the TSD ⁺ model	30
3.3 Antiphase Dynamics	33
3.4 Analysis of a three-mode laser	34
3.4.1 Steady states and stability	36
3.4.2 Self-pulsing solutions: physical mechanism	38
3.4.3 Self-pulsing solutions: analytical treatment	39
3.5 Conclusion	41
3.A Details of the linear stability analysis	43
References	47
4 Global coupling with time delay in semiconductor laser arrays	49
4.1 Introduction	49
4.2 Model	52
4.3 Synchronization below self-pulsing threshold	53
4.3.1 In-phase synchronization	53

4.3.2	Antiphase synchronization	54
4.4	Self-pulsing instabilities	56
4.5	Self-pulsing solutions	59
4.5.1	In-phase periodic solution	61
4.5.2	Antiphase periodic solutions	63
4.6	Conclusion	66
4.A	Linear stability analysis with nonzero local coupling	69
4.A.1	In-phase cw state	69
4.A.2	Anti-phase cw state	70
4.B	Derivation of the generalized phase equations	70
	References	73
5	Atomic interference in a microchip laser	75
5.1	Introduction	75
5.2	Derivation of the model	76
5.2.1	Effect of the low-frequency atomic coherence	78
5.2.2	Steady states	79
5.2.3	Linear stability analysis	80
5.2.4	Reduction of the model	81
5.3	Analysis of a two-transition laser	81
5.4	Conclusion	84
5.A	Derivation of the amplitude equation	87
	References	91
6	Inversionless amplification and propagation in an electro-nuclear level-mixing scheme	93
6.1	Introduction	93
6.2	The level Mixing scheme	94
6.3	Continuous wave amplification and propagation	99
6.3.1	Amplification mechanism	99
6.3.2	Propagation	102
6.4	Adiabatic pulse amplification	104
6.5	Ultrashort pulse amplification	106
6.6	Summary and Conclusion	108
6.A	Steady state solution	111
	References	113
7	Conclusions	115

Chapter 1

Introduction

Ever since their invention in 1960 [1], lasers have been exciting the curiosity of physicists by their strange dynamics: in spite of a constant excitation, they delivered a spiking output [2]. At that time also, oscillatory chemical reactions were observed [3], contradicting the firmly established belief that chemical reactions should always end up in steady state. These misbehaviors with respect to the general rule of equilibrium called for explanations and stimulated rapid developments in the theory of dynamical systems [4]. While the unstable laser output was still largely attributed to device imperfections and parasitic noise only, some physicists soon suggested that it might result from a fundamental nonlinearity in its equations of motion. In particular, various kinds of multimode operations were put forward as possible causes for the undamped laser pulsations (for a detailed historical account, see [5]). Grasnyuk and Oraevskii, after a numerical study of the equations governing a monomode laser with zero detuning from the atomic resonance, reported on the observation of irregular behavior [6]. Because of the important discrepancy between computed and experimentally observed thresholds for the onset of pulsations, this result went almost unnoticed in the physics community. Much more sensational was Lorenz notice of aperiodic motion in a weather model. His paper [7] marked the beginning of an intense research activity on what is now called “deterministic chaos” [8]. A decade later, Haken showed [9] that the laser equations studied by Grasnyuk and Oraevskii were actually isomorphic to the Lorenz model. However, these equations were considered by many as too simple to describe lasers. Moreover, the range of parameter values corresponding to chaotic dynamics seemed unrealistic. Some ten more years later, a NH_3 laser was built that finally behaved in good qualitative and quantitative agreement with the Lorenz-Haken equations [10]. This, together with other experimental and theoretical achievements [5], definitely established the relevance of a dynamical approach to the functioning of lasers. Understanding the laser instabilities and finding ways to control them is now becoming a routine problem for the applied physicists. Several monographs appeared during the last decade which underlined several of these aspects [11].

In this vein, the present thesis is an investigation of some nonlinear phenomena that occur in laser systems. Aside from the fundamental interest of the matter, such a study might help designing better optical sources for the engineer and the experimentalist. By “laser systems”, we mean both cavities and open systems where stimulated emission of radiation is used to amplify light.

While they are often regarded as a nuisance, dynamical instabilities sometimes give rise to useful applications. For instance, repetitive trains of powerful light pulses are of practical

interest in high-precision optical ranging or efficient nonlinear conversion. Promising optical sources of such pulses are the microchip lasers with saturable absorbers (LSA). They spontaneously generate pulsed output via a mode of operation called Passive Q-switching. Recent experimental studies of these microchip systems reveal unusual parameters values, which motivates us to reexplore the LSA theory in the first Chapter of this thesis. In these lasers, the onset of pulsations does not follow the usual scenario: instead of emerging directly at the first lasing threshold, pulsating intensity oscillations arise for larger pumping strengths after a Hopf bifurcation from the steady lasing state. It is known, however, that a Hopf bifurcation generally gives rise to harmonic oscillations. The fact that a pulsating output develops over a very narrow range of pump parameter is an indication that the Hopf bifurcation is singular. Examples of this dynamical behavior is documented in chemistry and biology [12], but has never been found in the laser context. Similarly to Haken with the Lorenz equations, we will note in the course of this study that the LSA problem is connected to the Lotka-Volterra model, used to describe chemical oscillations [13] as well as predator-prey ecology [14]. These equations received considerable attention as a general model of nonlinear oscillations [15].

The knowledge gained with the LSA will prove to be very useful in our second Chapter. We wish to determine how a smooth spatial variation of the pump profile along the cavity axis can influence the dynamics of a multimode laser. Previous studies, based on the recently derived TSD⁺ model [16], have indicated that this may induce self-pulsations in two-mode lasers. Encouraged by this result, we will analyze the three-mode case, which is more realistic if the spectral gain curve is symmetric. We will find that the underlying mechanism of this self-pulsing is very similar to that of the LSA: the spatially inhomogeneous excitation leaves some regions of the cavity unpumped, hence absorbent. This, together with the multimode operation, turns out to be the clue for the onset of pulsation. Moreover, we will discover memory effects associated to these spatial pump variations. Finally, we will examine a state of synchronization between modal intensities that is typical of these lasers and known as antiphase dynamics.

The issue of synchronization will reappear when we consider in Chapter III the dynamics of semiconductor laser (SCL) arrays with a global coupling. In these devices, it is required to lock the field phases emitted by each SCL in order to improve the beam and spectral qualities of the total output. We will deal with this question by regarding the lasing elements as oscillators, thus recasting the problem in a wider context: many other systems, such as arrays of Josephson junctions, reaction-diffusion systems, neural networks in the brain and even rhythmic applause in concert halls are also covered by the concept of coupled oscillators. Recently, much attention has also been paid to the synchronization of chaotic systems, with application to encryption. In the case of a global coupling, many theoretical results are already available, through the generic Kuramoto model [17]. Beside the theoretical difficulties associated to the numerous degrees of freedom, the SCL problem contains additional complications: the global coupling being achieved by an optical feedback, it is affected by a non negligible time delay. The influence of such a time delay on the synchronization of coupled oscillators is currently a subject of intense research, which makes SCL arrays even more relevant to investigate. Furthermore, the optical feedback is known to destabilize the continuous output of SCL's by inducing undamped relaxation oscillations. We will have therefore to examine the synchronization not only with respect to the optical oscillations of the electric field, but also with respect to the relaxation oscillations.

In the end of the 1980's, two papers [18] broke new grounds in the theory of light-matter

interaction. They showed independently and almost simultaneously that a population inversion was not necessary to achieve light amplification by stimulated emission of radiation. This dramatic conclusion rested on the consideration of more general quantum systems than the usual two-level scheme in the semi-classical approximation. In these system, the atoms can be prepared in special quantum superpositions of states where light absorption is suppressed. Such a quantum preparation amounts to create a quantum coherence between these states. Many new effects were found as a result of this quantum coherence, among which the spectacular Electromagnetically Induced Transparency [19]. Recently, experimental results indicated that quantum coherence effects were at play in the microchip LiNdP₄O₁₂ crystal (LNP in short) laser. This laser emitted a time periodic intensity when it was multimode. Experimental investigations further showed that these undamped relaxations oscillations were directly connected to simultaneous operation on multiple atomic transitions. The periodic behavior was not immediately detected because the associated relaxation oscillations were almost purely antiphased, so that the sum of the modal intensities remained practically constant. E. Viktorov directly recognized the Λ scheme behind this multi-transition operation. Together with P. Mandel proposed a model of the experiments carried out on the LNP laser. The theory, valid for two transitions, also included TSD⁺ features, thereby taking account of the fact that the cavity was end-pumped. Its success leads us to resume and reformulate the problem for an arbitrary number of transitions in Chapter IV. Our primary concern is to assess the actual role played by atomic coherence in this laser. Therefore, we will disregard the variations of the pump profile along the cavity axis. Indeed, from our previous study on the TSD⁺ model, we know that end-pumping can not be the cause of intensity oscillations. By carefully analyzing the multimode field phases inside the cavity, we will demonstrate that quantum coherence results in an enhancement of the stimulated absorption in the crystal. This effect is nonlinear, as it is generated by the electromagnetic field itself. Moreover, we will show that these nonlinear losses are sufficient to destabilize the steady state output of the LNP laser. In addition, we will demonstrate the antiphase character of the oscillations, in agreement with the experimental observation.

In the frame of the Interuniversity attraction pole program, we were involved in a joint research with the Instituut voor Kern- en Stralingsfysica (IKS). Our aim was to apply the principles of amplification without population inversion to nuclear transition. It is indeed technically impossible to achieve such an inversion in the nuclear domain, which has prevented the construction of a gamma ray laser so far. With the ideas of [18] in mind, the IKS team had already proposed to couple a radio-frequency electromagnetic field with the Hyperfine levels of a nuclear ground state [20]. However, it was later realized that, due to the equal population of all Hyperfine levels for a sample at room temperature, the necessary quantum coherence could not be achieved, so that the extension of the principles of atomic amplification without inversion to nuclear transitions remained problematic. In response to this problem, Rustem Shakhmuratov, while in visit in the IKS, proposed an alternative elecro-nuclear scheme, in which the RF field was replaced by a laser beam. In Chapter V, we will study this system and will find ranges of parameters that do allow the inversionless amplification of a weak gamma field. This positive result will however be moderated by the observation that part of the optical field energy is dissipated in the amplification process. Consequently, considering the propagation of a bichromatic optical-gamma field, there must be a limit distance beyond which the optical field is not sufficiently intense anymore to induce quantum coherence. This distance is a crucial piece of information to set up an experiment,

since it marks the transition from amplification to absorption of the gamma-field. We will therefore devote the second part of this research to its determination.

The diversity of subjects treated in the present work reflects the vitality of research in laser dynamics. Rather than focusing on a single question, we chose to participate in the multiple projects carried out in the ONT group. We were thus continuously in close contact with some of the most relevant topics in the field. This gave us the possibility to touch many facets of the nonlinear interaction of light with matter but also explains the generality of the title of this thesis.

A common and important feature to the studied physical systems is dissipation. Dissipative processes determine the timescales of the dynamics and play therefore a decisive role in it. It will often appear that some variables relax faster than others, which suggests the use of asymptotic techniques. Throughout this work, we will emphasize the analytical approach, completing it by numerical analysis. Whenever possible, we will try and interpret our mathematical results in physical terms, in order to extend our comprehension beyond the particular details of the models we use.

References

- [1] T.H. Maiman, Nature **187**, 483 (1960).
- [2] D.F. Nelson and W.S. Boyle, Appl. Opt. **1**, 181 (1962).
- [3] B.P. Belousov, Sb. Ref. Radiats. Med. Medgiz, (Moscow, 1959), 145; A.M. Zhabotinskii, Doklady Akademii Nauk SSSR **157**, 392 (1964).
- [4] J. Guckenheimer and P. Holmes, *Nonlinear Oscillations, Dynamical Systems, and Bifurcations of Vector Fields* (Springer-Verlag, New York, 1983); S.H. Strogatz, *Nonlinear Dynamics and Chaos* (Addison, 1994); G. Nicolis, *Introduction to Nonlinear Science* (Cambridge University Press, 1995);
- [5] N.B. Abraham, P. Mandel, and L.M. Narducci in *Progress in Optics XXV*, edited by E. Wolf (North-Holland, 1988), pp 3-190.
- [6] A.Z. Grasyuk and A.N. Oraevsky, Radio Eng. & Electron. Phys. **9**, 424.
- [7] E.N. Lorenz, J. Atmos. Sci. **20**, 130 (1963).
- [8] E.N. Lorenz, *The Essence of Chaos* (University of Washington Press 1993).
- [9] H. Haken, Phys. Lett. **53 A**, 77 (1975).
- [10] W. Klische and C.O. Weiss, Phys. Rev. A **31**, 4049 (1985).
- [11] C.O. Weiss and R. Vilaseca, *Dynamics of Lasers* (VCH Verlagsgesellschaft, Weinheim, 1991); H. Kawagushi, *Bistabilities and Nonlinearities in Laser Diodes* (Artech House, 1994); Y.I. Khanin, *Principles of Laser Dynamics* (Elsevier Science, 1995); P. Mandel, *Theoretical problems in cavity nonlinear optics* (Cambridge University Press, 1997); K.

- Otsuka, *Nonlinear Dynamics in Optical Complex Systems* (Kluwer Academic Publishing, 1999).
- [12] S.M. Baer and T. Erneux, SIAM J. Appl. Math. **46**, 721 (1986); SIAM J. Appl. Math. **52**, 1652 (1992).
 - [13] A.J. Lotka, J. Am. Chem. Soc. **42**, 1595 (1920); Proc. Nat. Acad. Sci. US **6**, 410 (1920).
 - [14] V. Volterra, Mem. Acad. Lincei. **2**, 31 (1926) (translation in R. N. Chapman's *Animal Ecology* (McGraw-Hill, New York, 1931, pp. 409-448).
 - [15] J. Grasman, *Asymptotic Methods for Relaxations Oscillations and Applications* (Springer-Verlag, New York, 1987), pp 72-87.
 - [16] D. Pieroux, Ph. D. Thesis: *Contribution à la dynamique des lasers multimodes et des lasers contrôlés par rétroaction*, Université Libre de Bruxelles, 1997.
 - [17] Y. Kuramoto, *Chemical Oscillations, Waves, and Turbulence* (Springer-Verlag, Berlin, 1984).
 - [18] O. Kocharovskaya and Ya. I. Khanin, Pis'ma Zh. Eksp. Teor. Fiz. **48**, 581 (1988) [JETP Lett. **48**, 630 (1988)]; S.E. Harris, Phys. Rev. Lett. **62**, 1033 (1989).
 - [19] S.E. Harris, Physics Today **50**, 36 (1997).
 - [20] R. Coussement, M. Van den Bergh, G. S'heeren, G. Neyens, R. Nouwen, P. Boolchand, Phys. Rev. Lett. **71**, 1824 (1993).

Chapter 2

Lasers with a weakly saturable absorber

2.1 Introduction

Microchip lasers with saturable absorbers (LSA) are promising tools for applications in which short and intense light pulses on monomode emission are needed and small size is required. They spontaneously generate pulsed output via a mode of operation called Passive Q-switching (PQS). Contrarily to other devices for which the cavity quality factor Q is suddenly changed, these devices do not require switching electronics. Their complexity is therefore much reduced compared to other microchip systems such as coupled-cavity Q-switched microchip lasers [1]. As noted in [2], their production is simplified by the fact that no interferometric control of the cavity dimension is necessary. This also relaxes the tolerance on the temperature stability during their use. They are therefore potentially inexpensive and robust lasers. With a pulse width below 100 ps and a peak power exceeding 5 kW [3], they are interesting for applications in medicine, light detection and ranging, and nonlinear frequency conversion [4]. The experimental study of these microchip systems revive the theoretical interest of LSA because they are characterized by unusual values of the relative saturability α between the absorber and the amplifier. This parameter is typically larger than one for gas [5, 6] and semiconductor lasers [7] with saturable losses while α is smaller than one for microchip lasers. As a result, qualitatively different responses may appear for these lasers. We should mention that the authors in [8] already considered this situation when studying PQS in a CO₂ laser with saturable losses. Motivated by the recent experiments on microchip lasers, the present chapter can therefore be viewed as an analytic continuation of [8]. From a mathematical viewpoint, our problem is a singular Hopf bifurcation, by which nearly harmonic periodic oscillations emerge in the intensity output but rapidly become pulsating. Such singular bifurcation problem have been studied in the past to describe pulsating chemical or biological oscillations [9]. We apply the method developed in [9] to analyze the microchip LSA. On this occasion, we find that that the problem is connected to the Lotka-Volterra equations used in the previous century to model chemical oscillations [10] as well as predator-prey ecology [11]. These equations received considerable attention as a general model of nonlinear oscillations [12].

This chapter is organized as follows. In section 2.2, we review the process of PQS caused by nonlinear losses. In addition, we present the model equations and summarize their linear stability analysis as performed in [13]. In section 2.3, we determine the size of the “bifurcation layer”, i.e. the small range of pump values over which pulsating oscillations develop.

With the help of the Lotka-Volterra equations, the analytic description of the bifurcation layer is performed in section 2.4. In the next section, we use a composite asymptotic expansion to describe and characterize the intensity pulse over the bifurcation layer. Finally, we conclude in Sec. 2.6.

2.2 Pulse generation by saturable losses

The resonant interaction of an electromagnetic field with a two-level system can lead either to absorption or amplification of light, depending on the incoherent excitation. In both cases, however, saturation effects arise for large intensities. This results from the fact that the same Einstein coefficient characterizes stimulated absorption and emission. As the number of photons becomes very large, these stimulated processes dominate the incoherent excitation and spontaneous emission. Consequently, the number of atoms in the ground and excited states tend to equalize and the medium becomes nearly transparent [14]. In a laser with saturable absorber, two separated cells are placed in the laser cavity. One of them is “active” or amplifying. It consists of two-level atoms with a positive population inversion, achieved by means of an external pump. The second cell is left with a negative inversion and is therefore absorbent, or “passive”. The coexistence of amplification and absorption makes the laser highly unstable and capable of avalanche effect. To be more specific, let us suppose that the laser is pumped above the lasing threshold. From a vanishing value, the intensity starts to grow with time. Eventually, one of the two cells becomes saturated. If it is the absorber that is bleached first, the overall cavity losses diminish. Consequently, as the intensity increases, it becomes more efficiently amplified. The growth of the intensity thus accelerates in an explosive manner until the amplifier becomes saturated in its turn. Finally, the linear cavity losses overcome the gain and the intensity falls to zero. This sustained generation of intensity pulses is called Passive Q-Switching. At first sight, PQS seems to require that the passive cell saturate for a smaller intensity than the active one. This condition is actually not necessary if the absorber has a faster dynamic than the amplifier because what actually matters is that the former saturates before the latter in the course of time.

In the simplest model of a LSA, passive and active media interact only with one cavity mode. Furthermore, the radiation is tuned in perfect resonance with the transition of both systems. Implicitly, we thus assume that the amplifying and absorbing atomic transitions have the same frequency and that they are homogeneously broadened. Three variables describe such a system. First, I is the laser intensity. It is rescaled in such a way that it starts to significantly saturates the amplifying cell when it is equal to one. The second variable is the gain. It is proportional to the average population difference on the amplifying transition and is noted D . Similarly, we define \bar{D} as the normalized averaged population difference on the absorbing transition. This leads to the following three rate equations, proposed by Yamada [7]:

$$\frac{dI}{dt} = I(-1 + D - \bar{D}), \quad (2.1)$$

$$\frac{dD}{dt} = \gamma [A - D(1 + I)], \quad (2.2)$$

$$\frac{d\bar{D}}{dt} = \bar{\gamma} [\bar{A} - \bar{D}(1 + \alpha I)]. \quad (2.3)$$

In these equations, A and \bar{A} are the pump parameters of the amplifying and absorbing media, respectively, and the parameter α represents their relative saturability. Time is measured in units of the cavity photon lifetime Γ_c^{-1} . In Eq. (2.2), $\gamma \equiv \gamma_{||}/\Gamma_c$ is the normalized decay rate of D towards equilibrium. Similarly, the relaxation rate $\bar{\gamma}_{||}$ of the saturable losses \bar{D} is rescaled as $\bar{\gamma} \equiv \bar{\gamma}_{||}/\Gamma_c$. The parameters γ and $\bar{\gamma}$ are typically very small, $\gamma, \bar{\gamma} \ll 1$ [15]. An exhaustive study of the Yamada model was presented in [16] for the case $\gamma = \bar{\gamma}$. Of particular interest is the parameter α because its value controls the mechanism by which pulses are produced. In general, $\alpha > 1$ for gas and semiconductor lasers. This is the most documented case in the literature. However, recent experiments with microchip lasers correspond to $\alpha < 1$ [3, 13]. We assume in the present analysis that α , γ , and A are independent parameters, although a more precise modelization of the system [13] indicates that this is only an approximation.

The lasing threshold, above which the non lasing solution is unstable, is given by

$$A = A_{th} \equiv \bar{A} + 1. \quad (2.4)$$

Above this threshold, laser action takes place and the population variables in the active and passive media are related to the intensity by

$$D = \frac{A}{1 + I}, \quad \bar{D} = \frac{\bar{A}}{1 + \alpha I}, \quad (2.5)$$

which shows directly the saturation of the gain and absorption with respect to the intensity. Moreover, since $D = \bar{D} + 1$ in steady state, the pump parameter A is connected to the intensity by the relation

$$A = (1 + I) \left(1 + \frac{\bar{A}}{1 + \alpha I} \right). \quad (2.6)$$

Close to threshold, we have

$$I \simeq \frac{A - A_{th}}{A_{th} - \alpha \bar{A}}. \quad (2.7)$$

In most LSA's, α is so large that the numerator of this last expression is negative. Therefore, the bifurcation from the zero intensity to the constant lasing solution is subcritical. A typical bifurcation scenario for large values of α is shown in Fig. 2.1: as soon as A surpasses the lasing threshold A_{th} , a strongly pulsating intensity output is produced. The period of this pulsating solution tends to infinity as $A - A_{th} \rightarrow 0^+$. In the language of dynamical system theory, this indicates that the bifurcation leading to such regime is a homoclinic bifurcation [16, 17]. For larger values of the pump parameter A , the constant intensity solution recovers stability and pulsation disappear.

A different situation is encountered if

$$\alpha < \frac{A_{th}}{\bar{A}}. \quad (2.8)$$

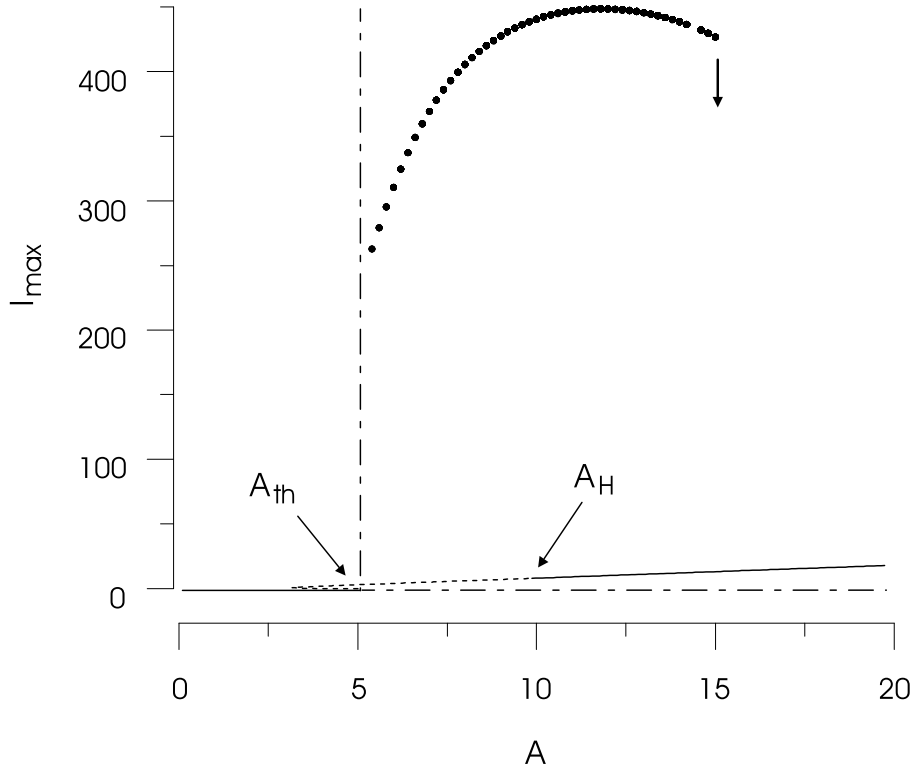


Figure 2.1: Bifurcation diagram computed with Eqs. (2.1) to (2.3) with $\bar{A} = 4$, $\alpha = 5$, $\gamma = 0.01$, $\bar{\gamma} = 0.1$. The lasing threshold is located at $A_{th} = 5$. For this value of α , the lasing solution emerges subcritically from the off solution. Dotted and dashed lines correspond to unstable segments of the steady state solution. Full circles indicate maxima of the intensity pulses that are produced immediately after the lasing threshold. A_H indicates a large intensity Hopf bifurcation by which the steady state solution becomes stable.

In this case, the constant lasing solution emerges supercritically from the zero intensity solution at $A = A_{th}$. Very close to this threshold, however, it can be destabilized by a Hopf bifurcation. Furthermore, over an extremely small range of pump parameter values, the resulting intensity oscillations change from harmonic to strongly pulsating, as illustrated in Fig. 2.2. The description of this rapid transition will be our main objective.

A linear stability analysis of the steady state solution (2.7) was performed in [13]. In the limit $\gamma, \bar{\gamma} \ll 1$, $\gamma = O(\bar{\gamma})$, there is a Hopf bifurcation close to the lasing threshold. It occurs at a small intensity $I = I_H$ given by:

$$I_H \simeq \frac{\gamma\bar{\gamma}(\gamma + \bar{\gamma})}{\alpha\bar{\gamma}^2\bar{A} - \gamma^2A_{th}}. \quad (2.9)$$

Using Eq. (2.6), the corresponding value of the pump parameter $A = A_H$ is:

$$A_H \simeq A_{th} + (A_{th} - \alpha\bar{A})I_H. \quad (2.10)$$

The value of I_H in (2.9) is physically relevant only if $\alpha > \gamma^2A_{th}/(\bar{\gamma}^2\bar{A})$. Combining this constraint with expression (2.8), the PQS regime we study corresponds to the values of α

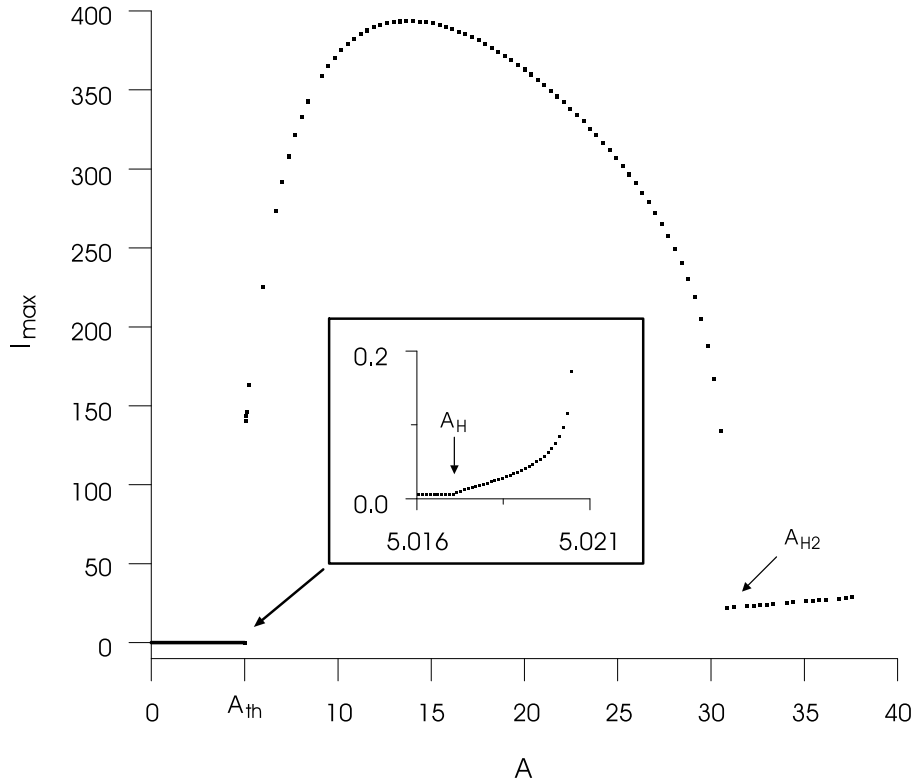


Figure 2.2: Bifurcation diagram with the same parameter values as in Fig. 2.1, except $\alpha = 0.5$. The zero intensity solution is first destabilized by a supercritical steady state bifurcation at $A_{th} = 5$. At $A_H = 5.017$, the steady state lasing solution is destabilized by a Hopf bifurcation. The branch of periodic solution becomes nearly vertical at $A_C \approx 5.02$, in good agreement with formula (2.22). For larger values of A , the amplitude of the pulsating solution grows rapidly and pass by a maximum at $A \approx 14$. The pulsations further disappear through a Hopf bifurcation at $A_{H2} \approx 30$.

satisfying

$$\boxed{\frac{\gamma^2 A_{th}}{\bar{\gamma}^2 \bar{A}} < \alpha < \frac{A_{th}}{\bar{A}}}.$$

This implies that $\gamma < \bar{\gamma}$. Such situation is encountered experimentally with microchip lasers having Nd:YAG as the gain medium and Cr:YAG as the saturable absorber [2, 4, 13]. Estimated parameter values are

$$\gamma = 1.7 \cdot 10^{-6}, \quad \bar{\gamma} = 6.3 \cdot 10^{-5}, \quad \alpha = 8.5 \cdot 10^{-2}, \quad A, \bar{A} = \mathcal{O}(1). \quad (2.11)$$

Experiments were also done on a Nd:YVO₄ microchip laser with semiconductor saturable absorber mirror (SESAM)[3]. For this system, the following parameters are evaluated as:

$$\gamma = 3.7 \cdot 10^{-7}, \quad \bar{\gamma} = 9.3 \cdot 10^{-2}, \quad \alpha = 3.7 \cdot 10^{-3}, \quad A, \bar{A} = \mathcal{O}(1). \quad (2.12)$$

Finally, let us mention for future reference that if the active and passive media consist of the same atoms, PQS is impossible. Indeed, in this case, the rescaled relaxation rate γ and $\bar{\gamma}$ are

identical and the relative saturability α equals one. Equations (2.1) to (2.3) then reduce to

$$\frac{dI}{dt} = I(-1 + \mathcal{D}), \quad (2.13)$$

$$\frac{d\mathcal{D}}{dt} = \gamma [\mathcal{A} - \mathcal{D}(1 + I)], \quad (2.14)$$

where $\mathcal{D} = D - \bar{D}$ and $\mathcal{A} = A - \bar{A}$. This shows that the system is then equivalent to an inefficiently pumped laser without saturable absorber. It is known that such a system does not deliver a pulsed intensity when it is free running [15]. We will see in the next Chapter, however, that this property is not always verified if the laser is multimode.

2.3 Size of the bifurcation layer

As we have seen in the previous section, the transition from harmonic to pulsating oscillations occurs on a very limited range of the pump parameter A . Let us now determine the value of A_C of the pump parameter until which the oscillations are still harmonic. The size of the bifurcation layer will be defined as $A_C - A_H$. To this end, we first examine numerically the pulsating solution close to the Hopf bifurcation point (See Fig. 2.3). In the (D, I) plane of the phase space, we note that the trajectory of the pulse spends a long time near the unstable separatrix that emerges from the saddle point $(A_{th}, 0)$. This suggests that the PQS pulsating oscillations result from a collision between the limit cycle emerging from the center $(\frac{\bar{A}}{1+I_H}, I_H)$ and this separatrix. Let us determine the value of A for which this happens. The coordinate of the Hopf point (2.9) and (2.10), together with the steady state expressions (2.5) motivates the new variables s , i , d , and \bar{d} defined by

$$s \equiv \gamma t, \quad I(t) \equiv \gamma i(s), \quad D(t) \equiv A_{th} + \gamma d(s), \quad \bar{D}(t) \equiv \bar{A} - \gamma \bar{d}(s). \quad (2.15)$$

Moreover, we introduce the parameters a and ε as

$$A \equiv A_{th} + \gamma a, \quad \varepsilon \equiv \frac{\gamma}{\bar{\gamma}}. \quad (2.16)$$

Inserting (2.15) and (2.16) into Eqs. (2.1) to (2.3) leads to the following equations for i , d , and \bar{d} :

$$\begin{aligned} i' &= i(d + \bar{d}), \\ d' &= a - d - A_{th}i, \\ \varepsilon \bar{d}' &= -\bar{d} + \alpha \bar{A}i. \end{aligned}$$

$$+O(\gamma) \quad (2.17)$$

In these equations, primes denote derivatives with respect to the rescaled time s and the $O(\gamma)$ corrections apply to the last two equations. The Hopf bifurcation for this reduced system is located at

$$a_H = \frac{(1 + \varepsilon)(A_{th} - \alpha \bar{A})}{\alpha \bar{A} - \varepsilon^2 A_{th}}. \quad (2.18)$$

This expression is equivalent to the location of the bifurcation point (2.10) in the original set of equations. Equations (2.17) cannot be solved analytically. Following our observation regarding the phase-space trajectory of the pulse, we seek a value of rescaled pump parameter a for which the trajectory degenerates into the unstable separatrix of the saddle point

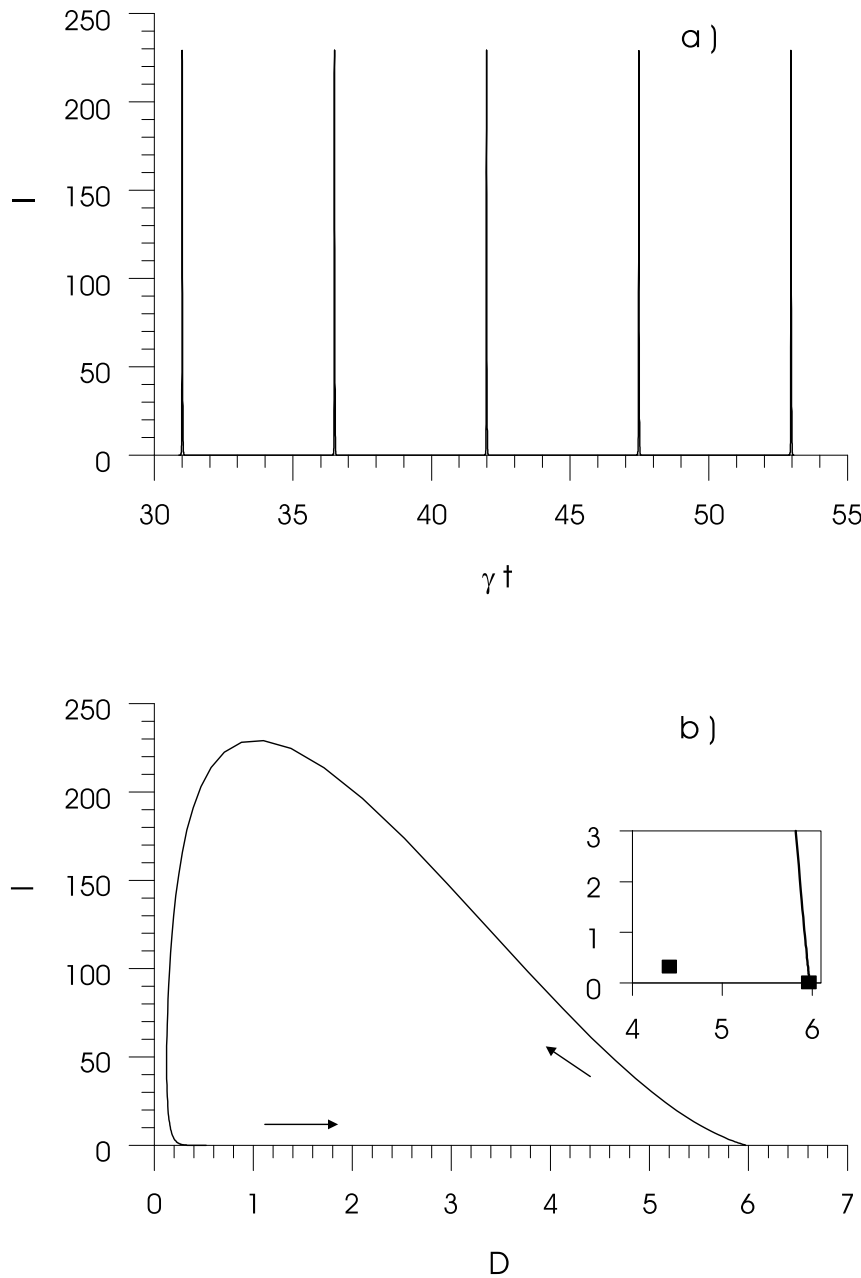


Figure 2.3: a) temporal trace of the pulsating solution for $A = 6$, $\bar{A} = 4$, $\alpha = 0.5$, $\gamma = 0.01$, and $\bar{\gamma} = 0.1$. b) phase portrait for the same parameters. The trajectory of the solution orbits around the steady state lasing solution at $(D, I) = (4.37, 0.37)$ and comes close to the stable and unstable manifolds of the off state $(D, I) = (6, 0)$. These two points are represented by squares in the inset. For small values of I , we see in the inset that the trajectory is almost linear when the system moves away from the saddle point $(6, 0)$.

$(d, \bar{d}, i) = (a, 0, 0)$. On this separatrix, we make the hypothesis that d and \bar{d} vary linearly with i . To verify this hypothesis, we write the variables d and \bar{d} as functions of i and compute their derivatives with respect to i . In the limit $\gamma \rightarrow 0$, we find:

$$\frac{d(d)}{di} = \frac{a - d - A_{th}i}{i(d + \bar{d})}, \quad \frac{d(\bar{d})}{di} = \frac{-\bar{d} + \alpha\bar{A}i}{\varepsilon i(d + \bar{d})}. \quad (2.19)$$

We then seek a solution of the form

$$d = a + \beta i, \quad \bar{d} = \delta i, \quad (2.20)$$

where β and δ are unknown coefficients to be determined. Substituting (2.20) into (2.19) gives the following conditions:

$$\beta = -\delta = \frac{-A_{th}}{1 + a} \quad (2.21)$$

and

$$a = a_C = \frac{A_{th} - \alpha\bar{A}}{\alpha\bar{A} - \varepsilon A_{th}}, \quad (2.22)$$

which defines a_C . In Figure 2.2, we see that a_C provides a good estimate for the onset of pulsations. The size of the bifurcation layer over which the solution becomes pulsating is given by $a_C - a_H$. Using (2.22) and (2.18), we find

$$a_C - a_H = \frac{\varepsilon(A_{th} - \alpha\bar{A})^2}{(\alpha\bar{A} - \varepsilon A_{th})(\alpha\bar{A} - \varepsilon^2 A_{th})}. \quad (2.23)$$

We note from 2.23 that the bifurcation layer becomes large as α decreases. As α approaches the critical value α_∞ given by

$$\alpha_\infty = \frac{\varepsilon A_{th}}{\bar{A}}, \quad (2.24)$$

a_C tends to infinity. The value α_∞ is thus a lower bound below which the absorbing cell of the LSA does not saturate enough to produce a pulsating output, although harmonic oscillations remain possible. Indeed, we recall that it is this saturation that causes the avalanche effect. From a mathematical viewpoint, however, our analysis is based on the assumption that a is of order unity. Therefore, if α is close to α_∞ , it loses its validity as a tends to a_C .

On the other hand, the size of the bifurcation layer decreases like ε for small ε , so that the Hopf bifurcation branch becomes more and more vertical. This clearly applies to the microchip Nd:YVO₄ laser with SESAM as indicated by (2.12) and, to a lesser extend, to the Nd:YAG/Cr:Yag LSA (2.11).

2.4 From harmonic to strongly pulsating oscillations

Having determined the size of the bifurcation layer $a_C - a_H$, we wish to describe the amplitude of the intensity oscillations for values of the rescaled pump parameter a between a_H and a_C and see how actually harmonic oscillations become pulsating. For the microchip LSA's

described by the sets of parameters (2.11) and (2.12), the ratio $\varepsilon = \gamma/\bar{\gamma}$ is small compared to unity. To take advantage of this fact, we rewrite the last equation of (2.17) as

$$\begin{aligned}\bar{d}' &= \alpha\bar{A}i - \varepsilon\bar{d}' \Rightarrow \bar{d}' = \alpha\bar{A}i' - \varepsilon\bar{d}'', \\ \bar{d} &\simeq \alpha\bar{A}i - \varepsilon\alpha\bar{A}i'\end{aligned}\quad (2.25)$$

The reduced model (2.17) in the vicinity of the Hopf bifurcation then becomes

$$i' = i(d + \alpha\bar{A}i) - \varepsilon\alpha\bar{A}ii', \quad (2.26)$$

$$d' = a - d - A_{th}i + O(\gamma), \quad (2.27)$$

We note from (2.11) and (2.12) that $\gamma \ll \varepsilon$. We may therefore neglect the $O(\gamma)$ terms in the last equation. The Hopf bifurcation for this reduced system coincides with the limit $\varepsilon \rightarrow 0$ in (2.18). It is located at

$$i_0 = \frac{1}{\alpha\bar{A}}, \quad d_0 = -1, \quad a_0 = \frac{A_{th}}{\alpha\bar{A}} - 1. \quad (2.28)$$

Introducing the new bifurcation parameter a_1 as

$$a = a_0(1 + \varepsilon a_1), \quad (2.29)$$

the steady state is simply given by

$$(i_s \ d_s) = (i_0 \ d_0) \times (1 + \varepsilon a_1)$$

It is then convenient to introduce the new variables v and w as

$$v = \frac{i}{i_s} - 1, \quad (2.30)$$

$$w = d - d_s + v. \quad (2.31)$$

The variable v directly measures the amplitude of intensity oscillations around the steady state. In terms of these new variables, Eqs. (2.26) and (2.27) become:

$$\begin{aligned}v' &= (1 + v)w + \varepsilon(1 + v)(a_1v - v'), \\ w' &= -v(a_0 - w) + \varepsilon[(1 + v)(a_1v - v') - (a_0 + 1)v].\end{aligned}\quad (2.32)$$

At the dominant order in ε , we show in the Appendix 2.A that these equations are equivalent to the Lotka-Volterra conservative system of equations [10, 11]. They admit a one-parameter family of periodic solutions, shown in Fig. 2.5. The related oscillations are nearly harmonic with frequency $\sqrt{a_0}$ close to the center $(v, w) = (0, 0)$ and become pulsating as the maximum intensity (the maximum of v) increases. This reduced system seems therefore able to reproduce the bifurcation layer in Fig. 2.2. The fact that it is conservative in dominant order contrasts with the three-variable system (2.17) encountered in the previous section. Setting $\varepsilon = 0$ in first approximation, the periodic solutions (v_0, w_0) of the system verifies the first integral:

$$E = v_0 - \ln(1 + v_0) - w_0 - a_0 \ln\left(1 - \frac{w_0}{a_0}\right). \quad (2.33)$$

In this expression, E is a constant that characterizes the amplitude of oscillations. In Appendix 2.B, we derive a solvability condition that relates implicitly the value of E to the bifurcation parameter a_1 . It writes

$$a_1 = \frac{\int_P (1 + v_0)^2 \frac{w_0^2}{a_0 - w_0} ds}{\int_P \frac{a_0 v_0^2}{a_0 - w_0} ds}, \quad (2.34)$$

where the integrals are evaluated over one period and are functions of E as the value of E determines the solution (v_0, w_0) . By evaluating the two integrals in (2.34), we may then find the corresponding value $a_1(E)$. This is done in Fig. 2.4, where we compare our analytical approximation with the bifurcation diagram of the system (2.1) to (2.3) and find an excellent agreement.

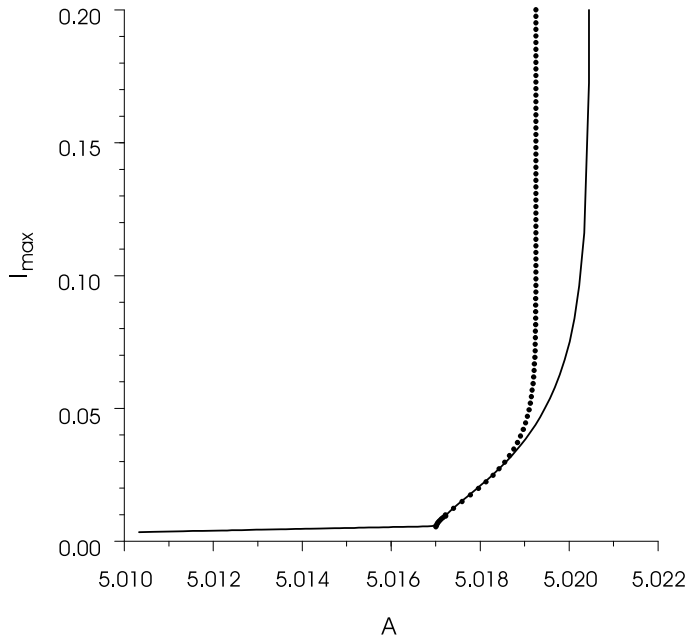


Figure 2.4: Enlargement of the bifurcation diagram 2.2 near the low-intensity Hopf point. The dotted line represent the analytical approximation, obtained with (2.34). The start of the analytical curve is shifted by 0.0005 on the right for a better fit with the numerical branch, which is in full line. The analytical curve agrees very well with the numerical curve, considering that ε is as large as 0.1 for this diagram.

Two limit cases can be studied analytically. On the one hand, we may examine Eq. (2.34) for small amplitude oscillations, i.e., we assume $E \ll 1$. For periodic solutions near the center $(v_0, w_0) = (0, 0)$, we have

$$(v_0, w_0) = \frac{\rho}{\sqrt{a_0}} (\sin \sqrt{a_0} s, \sqrt{a_0} \cos \sqrt{a_0} s), \quad (2.35)$$

where $\rho \ll 1$. Substituting this solution in (2.34), we obtain:

$$\rho = 2a_0 \sqrt{\frac{a_1 - 1}{2 + a_0}} \quad (2.36)$$

The amplitude of oscillation grows therefore parabolically with a_1 in the vicinity of the bifurcation point as we expect from Hopf bifurcation theory. Setting $\rho = 0$, we obtain the first correction in ε to the Hopf bifurcation point:

$$a_{1,H} = 1. \quad (2.37)$$

The second limit allowing an analytical evaluation of (2.34) is possible is the limit $E \gg 1$. We show in Appendix 2.B that

$$\lim_{E \rightarrow \infty} a_1(E) \equiv a_{1,C} = a_0 + 1. \quad (2.38)$$

Combining relations (2.29), (2.37), and (2.38), we recover the size of the boundary layer predicted in (2.23) for $\varepsilon \ll 1$:

$$a_0(\varepsilon a_{1,C} - \varepsilon a_{1,H}) = \varepsilon a_0^2 = \varepsilon \left(\frac{A_{th}}{\alpha \bar{A}} - 1 \right)^2. \quad (2.39)$$

2.5 Shape of the intensity pulse

This first integral (2.33) determines a family of periodic solutions. If $E \ll 1$, these solutions are of small amplitude and describe ellipses in the phase space. On the other hand, if $E \gg 1$, they are of large amplitude and correspond to the apparition of pulses in the system. We will now describe these pulses by composite asymptotic expansions [18, 19]. In the limit $E \gg 1$, the trajectory of the system in the phase plane can be described separately in 4 segments (See Fig. 2.5):

1. In the first segment, the LSA intensity is nearly zero. The corresponding portion of the phase space trajectory is therefore near the separatrix defined by $v = -1$. In this region, the pulse is approximately described (see Appendix 2.C) by $v \simeq v_1(s - s_1)$ with

$$v_1(s) = -1 + \exp[a_0(s + e^{-s} - 1) - E]. \quad (2.40)$$

2. In a second phase, the trajectory approaches the second separatrix defined by $w = a_0$. We then find that $v \simeq v_2(s - s_2)$ with

$$v_2(s) = -1 + e^{a_0 s}. \quad (2.41)$$

3. After this exponential growth, the intensity passes by a maximum $v \gg 1$. In this limit, we obtain $v \simeq v_3(s - s_3)$ with

$$v_3(s) = \frac{a_0 + E}{1 + e^{(E+a_0)s}} + \ln\left(\frac{a_0 + E}{a_0 + a_0 e^{-(E+a_0)s}}\right). \quad (2.42)$$

4. At its final stage, the pulse decreases violently and reaches a region of the phase plane where $|w| \gg 1$. This allows to derive for the intensity the approximate form $v \simeq v_4(s - s_4)$ with

$$v_4(s) = \frac{E - e^{Es}}{1 + e^{Es}}. \quad (2.43)$$

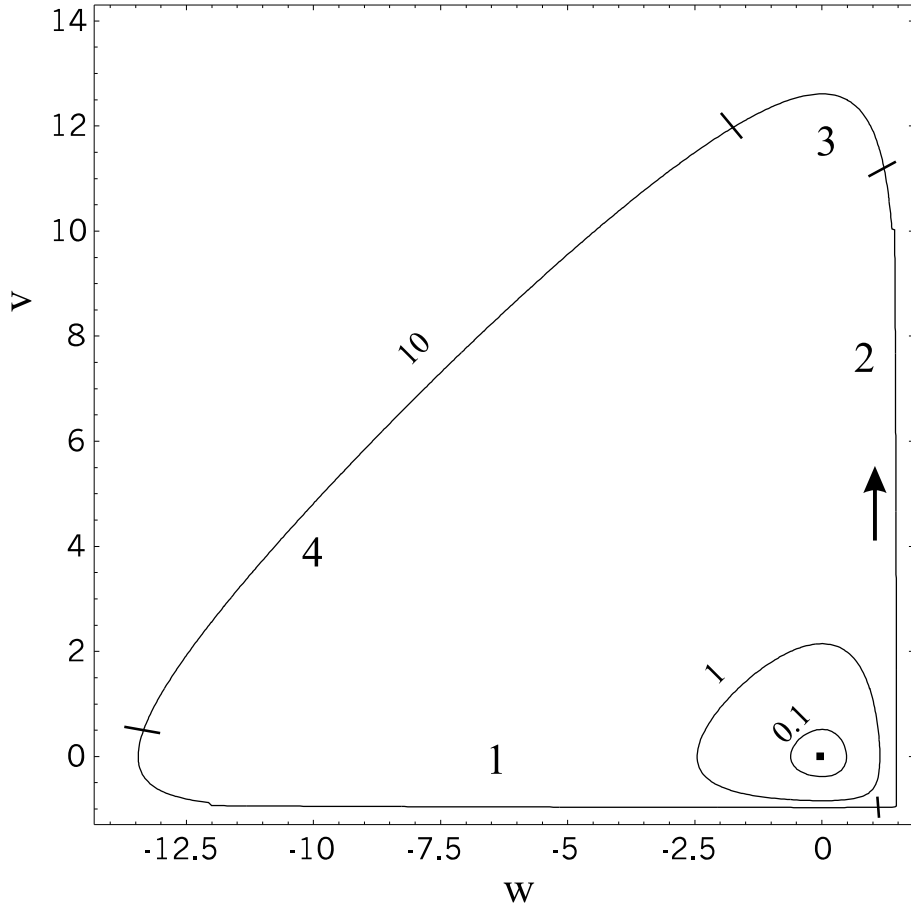


Figure 2.5: Phase portrait of the periodic solution of (2.32) with $\varepsilon \equiv 0$, $\bar{A} = 4$ and $\alpha = 0.5$, which yields $a_0 = 1.5$. From the smallest to the largest cycle, the values of the first integral E are 0.1, 1, and 10. The four regions in the phase space corresponding to the approximate solution v_1 to v_4 are indicated by the number 1 to 4 along the largest orbit. The direction of rotation is indicated by the arrow.

Knowing the form of the solution in different temporal intervals, we may construct the entire pulse as

$$v(s) = \begin{cases} v_1(s), & s < s_{12}, \\ v_2(s - s_2), & s_{12} < s < s_{23}, \\ v_3(s - s_3), & s_{23} < s < s_{34}, \\ v_4(s - s_4), & s_{34} < s. \end{cases} \quad (2.44)$$

The time constants $s_{12}, s_2, s_{23}, \dots$ are determined by the requirement that the solutions on subsequent intervals coincide in the vicinity of the connection points. Since we only have approximate solutions at our disposal, we require only that the functions and their derivatives be identical in the limit $E \gg 1$. The result of this analytical approximation is compared in Fig. 2.6 to the numerical integration of Eqs. (2.32) with $\varepsilon = 0$, showing a good qualitative and quantitative agreement. In Appendix 2.C, we find that the interpulse time scales linearly with the pulse maximum value. This duration is given by s_{12} and equals

$$s_{12} = \frac{E + a_0}{a_0}. \quad (2.45)$$

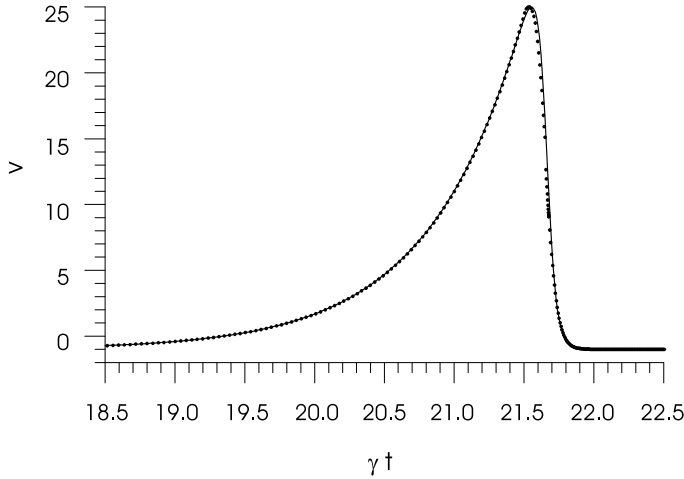


Figure 2.6: Temporal trace of a pulse obtained from (2.32) with $\varepsilon \equiv 0$. Full line, numerical integration with $\max(v) = 25$; dotted line, analytic approximation (2.44) with $E = 25$.

We note on the other hand that the pulse is strongly asymmetric. The rising edge of the pulse is much slower than its falling edge. Therefore, we may use $s_{23} - s_{12}$ as an estimation of the pulse duration. From (2.68), we find that

$$s_{23} - s_{12} = a_0^{-1} \ln(E + a_0 - a_0 e^{-1/a_0}). \quad (2.46)$$

Surprisingly, the pulse asymmetry is different from the shape calculated in [20]. Contrarily to what is shown in Fig. 2.6, these authors found that the descending part of the pulse is longer than the ascending part. Their results holds for large intensities, whereas the expressions presented in this section are only valid very close to the bifurcation threshold, as indicated by the scaling relations (2.15). To assess how the transition occurs between the two shapes, we compare two numerical integration of the original equation (2.1) to (2.3) performed at different distances of the Hopf point (see Fig. 2.7). We thus observe that on the quasi-vertical part of the periodic Hopf branch ($A = A_{th} + \gamma a$, with $a \simeq a_C$), the shape obtained from the reduced system (2.32) describes reasonably well the LSA output. However, beyond this vertical portion of the bifurcation diagram, the asymmetry is reversed and is fitted by the formula in [20]. This suggests that in between the two situations, there exists a range of pump values for which the pulse is almost symmetric, which might be interesting in solitonic applications.

2.6 Conclusion

Motivated by recent experiments on microchip lasers with saturable losses, we have revisited the LSA theory. The parameter values that are relevant to these experiments differ from the usual situation where the absorber has a lower saturation intensity than the amplifier. Rather than emerging from a homoclinic bifurcation at the laser first threshold, pulsations arise in this system through a singular Hopf bifurcation. We studied this bifurcation in the vicinity of the laser threshold $A = A_{th}$ and found a reduced three-variable problem that is not conservative. This is an important difference with respect to the previously studied singular

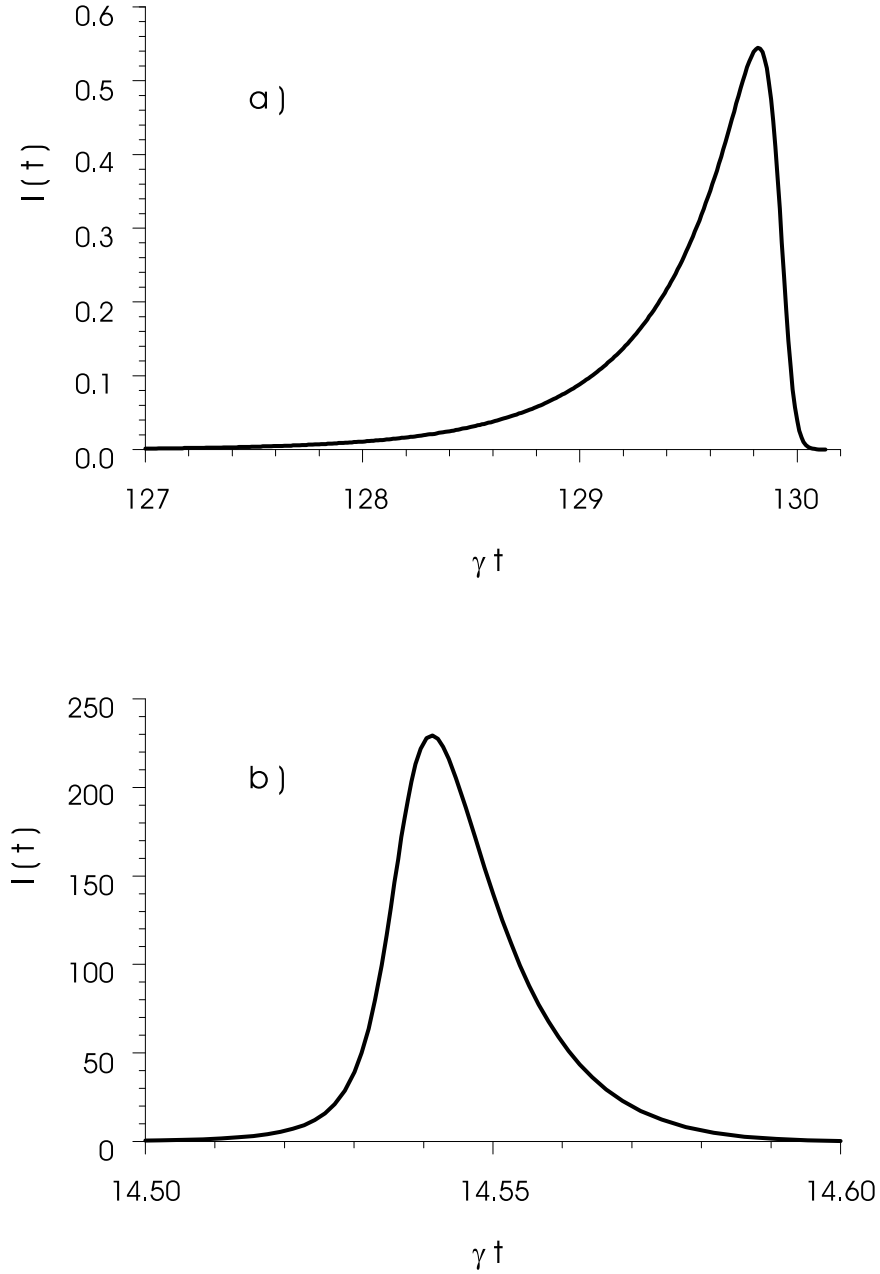


Figure 2.7: Shape of the pulse close and far from the Hopf instability, obtained by numerical integration of Eqs. (2.1) to (2.3) with $\bar{A} = 4$, $\alpha = 0.5$, $\gamma = 0.01$, $\bar{\gamma} = 0.1$. The Hopf point is at $A_H = 5.017$. a) $A = 5.0204836$. The shape of the pulse is still correctly described by the Lotka-Volterra system, despite the fact that $I = O(1)$ and the scaling relation (2.15) is no more satisfied. The rising edge is slower than the falling edge of the pulse. b) $A = 6$. The asymmetry of the pulse is now reversed and agrees with [20].

Hopf bifurcations [9]. In terms of the cavity damping rate Γ_c and the relaxation rates γ_{\parallel} and $\bar{\gamma}_{\parallel}$ of the amplifier and absorber, respectively, we found that the bifurcation layer has a size

$$A_C - A_H = \frac{\gamma_{\parallel}^2}{\bar{\gamma}_{\parallel}\Gamma_c} \frac{(A_{th} - \alpha\bar{A})^2}{\left(\alpha\bar{A} - \frac{\gamma_{\parallel}}{\bar{\gamma}_{\parallel}}A_{th}\right)\left(\alpha\bar{A} - \frac{\gamma_{\parallel}^2}{\bar{\gamma}_{\parallel}^2}A_{th}\right)}.$$

In microchip lasers, Γ_c is typically one order of magnitude larger than in conventional lasers due to the comparatively small cavity round-trip type. In addition the saturable absorber decays usually much faster to equilibrium than the amplifier, so that $A_C - A_H \ll 1$ in general. Therefore, the transition from harmonic to pulsating oscillations will be difficult to observe experimentally. However, the size of the bifurcation layer can be made larger if $\alpha\bar{A} - \frac{\gamma_{\parallel}}{\bar{\gamma}_{\parallel}}A_{th}$ is diminished. This can be achieved either with a small value of α , or by decreasing \bar{A} through the doping concentration of absorbing atoms and the size of the passive cell.

From the fact that in most situations $\gamma_{\parallel} \ll \bar{\gamma}_{\parallel}$, we may simplify the analysis further and obtain a conservative problem in the leading order of the small parameters $\gamma_{\parallel}/\Gamma_c$ and $\gamma_{\parallel}/\bar{\gamma}_{\parallel}$. This allows to use the technique developed in [9] and draw the full branch of periodic solution over the bifurcation layer.

Beyond the Hopf bifurcation layer, other asymptotic techniques can be used [13, 17] to determine the amplitude of the pulse as a function of the pump parameter A . By studying the pulse shape in the bifurcation layer, we realize that it has a different shape than for large A . Therefore, by designing a microchip laser with a large transition $A_C - A_H$, one can in principle control the shape of the pulse by the pump parameter. We may further conjecture that some value of A leads to a symmetric pulse shape. It would be interesting to verify this point either analytically or numerically in the future.

Appendix to Chapter 2

2.A The Lotka-Volterra equations

Lotka proposed as an hypothetical mechanism of reaction between two chemical products of concentrations X and Y the two kinetic equations [10]

$$X' = X(c_1 - c_2Y), \quad Y' = Y(-c_3 + c_4X). \quad (2.47)$$

Later, Volterra used de same equations [11] to describe the evolution of two populations having a predator-prey relation. The prey population X , has a natural growth rate c_1 and a death rate proportional to the number of predators: $-c_2Y$. On the other hand, the predator population has a death rate $-c_3$ in the absence of prey and grows otherwise with the rate c_4X . At the dominant order in ε , Eqs. (2.32) are

$$v'_0 = (1 + v_0)w_0, \quad (2.48)$$

$$w'_0 = -(a_0 - w_0)v_0. \quad (2.49)$$

These equations are identical to (2.47) with $c_1 \equiv a_0$ and $c_{2,3,4} \equiv 1$ upon the transformation

$$X = 1 + v_0, \quad Y = a_0 - w_0.$$

2.B Derivation of the solvability condition

In the leading order in ε , the system (2.32) reduces to Eqs. (2.48) and (2.49). At this order, a one-parameter family of periodic solutions $(v_0(s; E), w_0(s; E))$ exists. They verify the first integral (2.33). However, only one of these periodic solutions is also a periodic solution of the full system (2.32). To determine it, we introduce the functional

$$\tilde{E}(v(s), w(s)) = v - \ln(1 + v) - w - a_0 \ln\left(1 - \frac{w}{a_0}\right). \quad (2.50)$$

This functional, computed with the true periodic solution of (2.32) should verify in first approximation the condition

$$\int_P \tilde{E}' ds = 0, \quad (2.51)$$

where P is the period of the solution. Using (2.32), we can rewrite this condition as

$$\int_P \left\{ v(a_1 v - v') + \frac{w}{a_0 - w} [(1 + v)(a_1 v - v') - (a_0 + 1)v] \right\} ds = 0. \quad (2.52)$$

We now evaluate this expression with $v_0(s; E)$ and $w_0(s; E)$. To this end, we note that

$$\int_P v_0 v'_0 ds = \frac{1}{2} [v_0^2(s)]_0^P = 0. \quad (2.53)$$

Moreover, using (2.48), we find that

$$\int_P \frac{v_0 w_0}{a_0 - w_0} ds = \int_P \frac{-w_0 w'_0}{(a_0 - w_0)^2} ds = \left[-\ln(a_0 - w_0(s)) - \frac{a_0}{a_0 - w_0(s)} \right]_0^P = 0. \quad (2.54)$$

In the same way, we demonstrate that $\int_P v_0^n w_0 / (a_0 - w_0) ds = 0$. Finally, (2.52) reduces to

$$\int_P \left[a_1 v_0^2 - \frac{w_0^2 (1 + v_0)^2}{a_0 - w_0} \right] ds = 0, \quad (2.55)$$

which is the solvability condition (2.34).

Let us now derive the critical value of a_1 that corresponds to an infinite value of E . In this limit, the orbit of the periodic solution $(v_0(s; E), w_0(s; E))$ spends most of the time in the vicinity of the separatrix $w = a_0$. The first integral (2.33) can then be approximated by

$$\begin{aligned} E &\simeq v_0 - \ln(1 + v_0) - a_0 - a_0 \ln\left(1 - \frac{w_0}{a_0}\right), \\ &\rightarrow w_0 \simeq a_0 - a_0 \left(\frac{e^{E+a_0-v_0}}{1+v_0}\right)^{1/a_0}. \end{aligned}$$

In addition, the integration of one period is replaced by an integration over the time spent near the separatrix $w = a_0$:

$$\int_P f(s) ds \simeq \int_{v_{\min}}^{v_{\max}} \frac{f(v)}{w(1+v)} dv \simeq \int_{-1}^{\infty} \frac{f(v)}{a_0(1+v)} dv.$$

Equation (2.52) eventually becomes

$$\begin{aligned} a_1 &= \frac{\int_{-1}^{\infty} a_0 (1+v)^{1+1/a_0} e^{-v/a_0} dv}{\int_{-1}^{\infty} (1+v)^{-1+1/a_0} v^2 e^{-v/a_0} dv}, \\ &= \frac{a_0 \int_0^{\infty} \xi^{-1+1/a_0} e^{-\xi} d\xi}{\int_0^{\infty} (a_0^2 \xi^{1+1/a_0} - 2a_0 \xi^{1/a_0} + \xi^{-1+1/a_0}) e^{-\xi} d\xi}. \end{aligned}$$

Integration by parts of the numerator then yields $a_1 = 1$ (2.38).

2.C Asymptotic matching for the pulse

In this section, we derive the approximations (2.40), (2.41), (2.42), and (2.43) for the pulse and determine the time constants s_{12}, s_2, s_3, \dots in (2.44).

In the first region, $v \simeq -1$. Substituting this approximation in Eq. (2.49) yields $w = w_1(s - s_1)$, with

$$w_1(s) = a_0(1 - e^{-s}). \quad (2.56)$$

The expression (2.40) for v_1 is deduced from the first integral (2.33), where we neglect v_1 as compared to $-\ln(1 + v_1)$.

The second region corresponds to the initiation of the pulse. The trajectory approaches the second separatrix, so that $w_2 \simeq a_0$. Substituting this approximation in (2.49) directly yields (2.41).

In the third region, the intensity passes by a maximum. We have therefore $v_3 \gg 1$ in (2.33) and can neglect $\ln(1 + v_3)$ by comparison. This gives

$$v_3 \simeq E + w_3 + a_0 \ln\left(1 - \frac{w_3}{a_0}\right). \quad (2.57)$$

Equation (2.48) is then transformed into

$$\begin{aligned} w'_3 &\simeq -(a_0 - w_3) \left[E + w_3 + a_0 \ln\left(1 - \frac{w_3}{a_0}\right) \right] \\ &\simeq -(a_0 - w_3)(E + w_3), \end{aligned} \quad (2.58)$$

where the logarithmic term is omitted in the right hand side for the sake of integrability and because it is zero when v_3 is maximum. The solution of this equation is $w = w_3(s - s_3)$, with

$$w_3(s) = \frac{a_0 - Ee^{(E+a_0)s}}{1 + e^{(E+a_0)s}}. \quad (2.59)$$

Using (2.57), we deduce v_3 in (2.42).

Finally, at the end of the pulse, we have $|w_4|, v_4 \gg 1$ so that the first integral can be reevaluated as $w_4 \simeq v_4 - E$. Substituting this into (2.47) we obtain an integrable equation for the intensity variable

$$v'_4 \simeq (1 + v_4)(v_4 - E), \quad (2.60)$$

which yields (2.43).

2.C.1 Matching first and second segments

In the vicinity of s_{12} , we have, with $x_{12} \equiv s - s_{12}$

$$\begin{aligned} v_1(s) &= -1 + \exp[a_0(s_{12} - 1 + e^{-s_{12}}) - E] \\ &\quad \times [1 + a_0(1 - e^{-s_{12}})x_{12}] + O(x_{12}^2), \end{aligned} \quad (2.61)$$

$$v_2(s) = -1 + e^{a_0(s_{12}-s_2)}(1 + a_0x_{12}) + O(x_{12}^2). \quad (2.62)$$

The matching of the two functions requires

$$\exp[a_0(s_{12} - 1 + e^{-s_{12}}) - E] \simeq e^{a_0(s_{12}-s_2)}, \quad (2.63)$$

$$a_0(1 - e^{-s_{12}}) \simeq a_0. \quad (2.64)$$

In the limit $E \gg 1$, these conditions are satisfied if we take

$$s_2 = \frac{E + a_0}{a_0}, \quad s_{12} = s_2. \quad (2.65)$$

2.C.2 Matching second and third segments

Introducing $x_{23} \equiv s - s_{23}$ and the auxiliary functions $y_2 \equiv e^{a_0(s_{23}-s_2)}$ and $y_3 \equiv e^{(a_0+E)(s_{23}-s_3)}$ we obtain the matching conditions

$$y_2 - 1 = \frac{a_0 + E}{1 + y_3} + a_0 \ln \frac{(a_0 + E)y_3}{a_0(1 + y_3)}, \quad (2.66)$$

$$a_0 y_2 = \frac{(a_0 - E y_3)(a_0 + E)}{(1 + y_3)^2}. \quad (2.67)$$

In the limit $E \gg 1$, we have the approximate solutions

$$\begin{aligned} y_2 &= \frac{a_0 + E}{1 + y_3}, \\ y_3 &= \frac{a_0 e^{-1/a_0}}{E + a_0 - a_0 e^{-1/a_0}} \end{aligned}$$

from which we deduce that

$$\begin{aligned} s_{23} - s_2 &= a_0^{-1} \ln(E + a_0 - a_0 e^{-1/a_0}), \\ s_3 - s_{23} &= (a_0 + E)^{-1} \ln \frac{E + a_0 - a_0 e^{-1/a_0}}{a_0 e^{-1/a_0}}. \end{aligned} \quad (2.68)$$

2.C.3 Matching third and last segment

To connect the last part, we use $x_{34} \equiv s - s_{34}$, $\bar{y}_3 \equiv e^{(a_0+E)(s_{34}-s_3)}$, and $\bar{y}_4 \equiv e^{E(s_{34}-s_4)}$. We obtain the matching conditions

$$\frac{E - \bar{y}_4}{1 + \bar{y}_4} = \frac{a_0 + E}{1 + \bar{y}_3} + a_0 \ln \frac{(a_0 + E)\bar{y}_3}{a_0(1 + \bar{y}_3)}, \quad (2.69)$$

$$\frac{-E(1 + E)\bar{y}_4}{(1 + \bar{y}_4)^2} = \frac{(a_0 + E)(a_0 - E\bar{y}_3)}{(1 + \bar{y}_3)^2}. \quad (2.70)$$

We solve these two equations numerically in order to obtain Figure 2.44.

References

- [1] J.J. Zaykowski and C. Dill III, Opt. Lett. **17**, 1201 (1992).
- [2] J.J. Zaykowski and C. Dill III, Opt. Lett. **19**, 1427 (1994).
- [3] G. J. Spühler, R. Paschotta, R. Fluck, B. Braun, M. Moser, G. Zhang, E. Gini, and U. Keller, J. Opt. Soc. Am. B **16**, 376 (1999).
- [4] J.J. Zaykowski, Opt. Lett. **21**, 588 (1996); Erratum, Opt. Lett. **21**, 1618 (1996).
- [5] E. Arimondo, F. Casgrande, L. A. Lugiato, and P. Glorieux, Appl. Phys. B **30**, 57 (1983).
- [6] M. Tachikawa, K. Tanii, and T. Shimizu, J. Opt. Soc. Am. B **4**, 387 (1987).
- [7] M. Yamada, IEEE J. Quantum Electron. **29**, 1330 (1993).
- [8] E. Arimondo, P. Bootz, P. Glorieux, and E. Menchi, J. Opt. Soc. Am. B **2**, 193 (1985).
- [9] S.M. Baer and T. Erneux, SIAM J. Appl. Math. **46**, 721 (1986); SIAM J. Appl. Math. **52**, 1652 (1992).
- [10] A.J. Lotka, J. Am. Chem. Soc. **42**, 1595 (1920); Proc. Nat. Acad. Sci. US **6**, 410 (1920).
- [11] V. Volterra, Mem. Acad. Lincei. **2**, 31 (1926) (translation in R. N. Chapman's *Animal Ecology* (McGraw-Hill, New York, 1931, pp. 409-448).
- [12] J. Grasman, *Asymptotic Methods for Relaxations Oscillations and Applications* (Springer-Verlag New York 1987), pp 72-87.
- [13] P. Peterson, A. Gavrielides, M.P. Sharma, and T. Erneux, IEEE J. Quant. Electron. **35**, 1245 (1999).
- [14] A. E. Siegman, *Lasers* (University Sciences Books, 1986), pp. 204-210.
- [15] P. Mandel, *Theoretical problems in cavity nonlinear optics* (Cambridge University Press, 1997).
- [16] J.L.A. Dubbeldam and B. Krauskopf, Opt. Comm. **159**, 325 (1999).
- [17] T. Erneux, J. Opt. Soc. B **5**, 1063 (1988).
- [18] C.M. Bender and S.A. Orszag, *Advanced Mathematical Methods for Scientists and Engineers* (Springer-Verlag New York 1999).
- [19] J. Kevorkian and J.D. Cole, *Multiple Scale and Singular Perturbation Methods* (Springer-Verlag New York 1996).
- [20] T. Erneux, P. Peterson, and A. Gavrielides, Eur. Phys. J. D **10**, 423 (2000).

Chapter 3

Solid state lasers with spatially distributed gain

3.1 Introduction

Despite the fact that they share the same physical mechanisms to generate coherent light, ring cavity and Fabry-Perot cavity lasers have radically different behaviors. Their difference resides in the structure of the cavity electromagnetic modes that support the laser radiation. In a ring cavity, they are plane waves. If it is perfectly symmetric, there is no preferential direction of propagation and both directions should generally be taken into account. This provides the simplest example of a multimode laser [1]. In most situations, however, if the linewidth broadening is homogeneous, ring lasers are monomode. They lend themselves to a relatively simple mathematical description because the intensity distribution is uniform inside the cavity for all eigenmodes. With this respect, it was shown that their evolution equations are equivalent to the Lorenz equations, a model that has become generic in the study of chaos [2]. Consequently, they exhibit a very rich phenomenology of complex behavior and, for this reason, have received much attention from theoretical physicists.

On the other hand, the eigenmodes of Fabry-Perot lasers are stationary waves. These lasers operate more easily in multimode configuration, even when homogeneously broadened. Moreover, they are intrinsically stable. By contrast with the ring cavity, the problem of an adequate description of a multimode Fabry-Perot laser in the rate equation limit is difficult. By rate equations, we mean equations that couple the electromagnetic fields and the population inversion only. The first successful model was proposed by Tang, Statz, and deMars [3] who showed that the dominant feature driving these lasers was the coupling between the modal intensities and the average population inversion via the population inversion grating, also known as spatial hole burning. The characteristic length of these population gratings is half the optical wavelength. Soon afterwards, a number of theoretical models generalizing the Tang, Statz, and deMars (TSD) equations were proposed to account for additional mechanisms: the coupling among the complex field modal amplitudes (phase-sensitive interactions), the coupling between the complex field modal amplitudes and the population grating at either optical or/and long wavelengths, and the longitudinal inhomogeneity of the pumping mechanism [4, 5, 6, 7, 8, 9, 10]. The TSD⁺ model [11] is a recent extension of the TSD model that includes (i)the coupling of the modal intensities to the low spatial frequencies of the inversion of population profile and (ii)the pump profile in the longitudinal direction.

Transverse effects are ignored in this approach. This chapter is devoted to a systematic study of the TSD⁺ model.

In Sec. 3.2, we briefly review the derivation of the TSD⁺ model and define the notations. In Sec. 3.3, we prove that a fundamental theorem of antiphase dynamics, which was demonstrated for the TSD equations, is preserved by the TSD⁺ extension. This theorem deals with the properties of the total intensity, which in the rate equation approximation is the sum of the modal intensities. It states that in the limit of a flat spectral gain curve, the deviation of the steady state total intensity is a global variable verifying a single linear harmonic oscillator equation with a frequency Ω_R that is mode-independent. These relaxation oscillations generate a peak in the power spectrum of the total intensity when the laser is subjected to an external perturbation (noise, weak modulation, transient relaxation, for instance). This is in contrast with the modal intensities which display a larger number of peaks, typically as many peaks (and therefore relaxation oscillation frequencies) as there are modes, and possibly harmonics of these frequencies.

Concerning the dynamics of a laser operating on an arbitrary number of modes, little can be said from analytical point of view, besides antiphase dynamics. In order to gain insight into the model, we will therefore restrict our attention on a fixed number of modes. The two-mode case was already treated in [12]. It is not always realistic however, if one considers atoms with a gain curve that is symmetric in the spectral domain, such as neodymium (Nd). Indeed, in this case, the laser cavity is typically tuned in such a way that one mode coincides with the atomic resonance. Then, as the pump parameter is increased, the number of lasing mode varies typically as $1 \rightarrow 3 \rightarrow 5 \rightarrow \dots$. Therefore, in Sec. 3.4, we analyze systematically a symmetric three-mode configuration with one central mode of maximum gain \mathcal{L}_{\max} and two side modes with equal gains smaller or equal to \mathcal{L}_{\max} . We give the expressions of the steady state solutions and determine their stability. In particular, we analyze the Hopf bifurcations which may destabilize multimode solutions only. Given the difficulty to determine the existence and stability character of these bifurcations in the usual way (i.e., linear stability analysis of the steady state), we adopt an alternative approach which is suggested by the numerical simulations of the TSD⁺ equations. Indeed, they are prone to display pulsed solutions, as in a passive Q-switching process. On this basis, we assume the existence of pulsed solutions and determine analytically the conditions of existence of an inter-pulse solution, in which the modal intensities are vanishingly small. It turns out that this problem can be solved analytically, even for an arbitrary number of modes, and the conditions of existence are identical with the Hopf bifurcation conditions whenever a straightforward linear analysis has been possible.

The results presented in this chapter were published in [13].

3.2 Derivation of the TSD⁺ model

We consider a Fabry-Perot cavity of length L that supports N modes of oscillation for the electric field:

$$E(z, t) = \sum_{p=1}^N (E_p(t) e^{i\omega_p t} + c.c.) \sin(k_p z), \quad (3.1)$$

Given the speed of light c' inside the cavity, the wave numbers k_p satisfy the relation $k_p = \omega_p/c' = n_p \pi/L$. In addition, the cavity is filled with atoms that possess a resonant transition with the laser field (see Fig. 3.1). With respect to this atomic resonance ω_{21} , the field modes

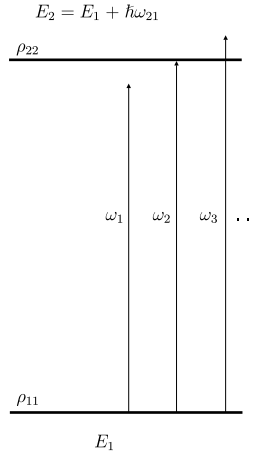


Figure 3.1: The two-level system.

are characterized by the detunings $\Delta_p = \omega_p - \omega_{21}$. We treat the atoms by a two-level description in which γ_{\parallel} and γ_{\perp} are the relaxation constants for the population inversion and the atomic polarization, respectively. The lasers considered in this model are characterized by the fact that $\gamma_{\perp} \gg \gamma_{\parallel}$. Examples of laser mediums to which this inequality applies are Nd:YAG, LiNdP₄O₁₂, and semiconductors. For such lasers, the polarization can be eliminated adiabatically. In the rotating wave and slowly varying amplitude approximations [1], the Maxwell-Bloch equations for this system become, with $t_{\parallel} = \gamma_{\parallel}t$,

$$\frac{dI_p(t_{\parallel})}{dt_{\parallel}} = \kappa \left(-1 + \mathcal{L}_p \frac{1}{L} \int_0^L 2D(z, t_{\parallel}) \sin^2(k_p z) dz \right) I_p(t_{\parallel}), \quad (3.2)$$

$$\frac{\partial D(z, t_{\parallel})}{\partial t_{\parallel}} = w(z) - D(z, t_{\parallel}) \left(1 + \sum_p 2I_p(t_{\parallel}) \sin^2(k_p z) \right). \quad (3.3)$$

In these equations, I_p is the intensity of mode p , rescaled as $I_p = 2\mathcal{L}_p |d_{12}E_p|^2 / (\hbar^2 \gamma_{\parallel} \gamma_{\perp})$, where $\mathcal{L}_p \equiv (1 + \Delta_p^2 / \gamma_{\perp}^2)^{-1}$ and d_{12} is the matrix element of the dipole operator between the two states of the transition. The quantity $D(z, t_{\parallel})$, is the rescaled distribution of population inversion along the cavity axis. It is given by $D(z, t_{\parallel}) = N\omega_{21} |d_{12}|^2 (\rho_{22} - \rho_{11}) / (\epsilon \hbar \gamma_{\parallel} \Gamma_c)$, where N is the density of atoms, ρ is their density operator, and Γ_c is the cavity damping rate. The effect of incoherent pumping is contained into $w(z)$, towards which $D(z, t_{\parallel})$ tends in the absence of a laser field. Finally, the cavity damping rate is expressed in the timescale $t_{\parallel} = \gamma_{\parallel}t$ as $\kappa = \Gamma_c / \gamma_{\parallel}$.

Equations (3.2) and (3.3) are nonlinear and integro-differential, which leaves little hope to obtain analytical result on the laser dynamics. Nevertheless, a Lyapunov function was found [14], demonstrating that, under some conditions, only one solution is stable, with constant modal intensities I_p . Indeed, denoting the steady state value of any variable $g(t_{\parallel})$

with an overbar, \bar{g} , the function

$$\mathcal{F}(t_{\parallel}) = \frac{1}{L} \int_0^L \frac{[D(z, t_{\parallel}) - \bar{D}(z)]^2}{2\bar{D}(z)} dz + \sum_p \frac{1}{\kappa \mathcal{L}_p} \left[I_p(t_{\parallel}) - \bar{I}_p - \bar{I}_p \ln \frac{I_p(t_{\parallel})}{\bar{I}_p} \right] \quad (3.4)$$

verifies $\mathcal{F} \geq 0$ and $d\mathcal{F}/dt_{\parallel} < 0$. This means that \mathcal{F} tends to zero as $t_{\parallel} \rightarrow \infty$ and, hence, $D(z, t_{\parallel})$ and $I_p(t_{\parallel})$ must tend to their steady state values $\bar{D}(z)$ and \bar{I}_p . We shall get back to this result later in this chapter. More recently [15], the relaxation towards this stable solution was discussed for various pump profiles $w(z)$.

The right hand side of Eqs. (3.2) and (3.3) suggests for $D(z, t)$ and $w(z)$ a Fourier decomposition:

$$f_0 = \frac{1}{L} \int_0^L f dz, \quad f_n = \frac{2}{L} \int_0^L f \cos(2n\pi z/L) dz, \quad f = D(z, t), w(z). \quad (3.5)$$

This transforms the system (3.2) and (3.3) into an infinite set of moment equations:

$$\frac{dI_p}{dt_{\parallel}} = \kappa \left[-1 + \mathcal{L}_p \left(D_0 - \frac{D_{n_p}}{2} \right) \right] I_p, \quad (3.6)$$

$$\frac{dD_0}{dt_{\parallel}} = w_0 - D_0 \left(1 + \sum_q I_q \right) + \frac{1}{2} \sum_q D_{n_q} I_q, \quad (3.7)$$

$$\frac{dD_{n_p}}{dt_{\parallel}} = w_{n_p} - D_{n_p} \left(1 + \sum_q I_q \right) + \left(D_0 + \frac{D_{2n_p}}{2} \right) I_p + \sum_{q \neq p} \frac{D_{n_p-n_q} + D_{n_p+n_q}}{2} I_q. \quad (3.8)$$

Due to its intensity distribution proportional to $\sin^2(k_p z)$ inside the cavity, a given mode p of the field burns in the population inversion profile $D(z, t)$ a grating of holes with spatial frequency $2k_p$. The corresponding Fourier component is D_{n_p} . It is sometimes referred to as “the population grating” relative to mode p . In the early days of laser physics, Tang, Statz, and de Marz [3] truncated Eqs. (3.6) to (3.8), retaining the mean inversion and pump, D_0 and w_0 , as well as the population gratings D_{n_p} but neglecting D_{2n_p} and $D_{n_p \pm n_q}$. The resulting finite set of ordinary differential equation is the TSD model. The validity of this truncation was discussed recently in [15] with the conclusion that it is a safe approximation as long as the pump is constant over the cavity. The TSD model accounts for stable multimode operation and provides a good qualitative picture of how the laser relaxes to the steady state. However, it neglects the influence of spatial inhomogeneities in the pump distribution $w(z)$ on the laser dynamics. This motivated D. Pieroux and P. Mandel to propose a different truncation of Eqs. (3.6) to (3.8). They included in their model the low frequency gratings $D_{n_p-n_q}$ where p

and q correspond to lasing modes. They obtained what is now called the TSD⁺ model [11]:

$$\begin{aligned} w_x &\equiv w_{n_p - n_q}, \quad D_x \equiv D_{n_p - n_q}, \quad N_p \equiv D_{n_p}, \quad x = n_p - n_q, \\ \frac{dI_p}{dt_{\parallel}} &= \kappa \left[-1 + \mathcal{L}_p \left(D_0 - \frac{N_p}{2} \right) \right] I_p, \end{aligned} \quad (3.9)$$

$$\frac{dD_0}{dt_{\parallel}} = w_0 - D_0 \left(1 + \sum_q I_q \right) + \frac{1}{2} \sum_q N_q I_q, \quad (3.10)$$

$$\frac{dD_r}{dt_{\parallel}} = w_r - D_r \left(1 + \sum_q I_q \right) + \frac{1}{2} \sum_{q=1}^{N-r} N_{r+q} I_q + \frac{1}{2} \sum_{q=r+1}^N N_{q-r} I_q, \quad (3.11)$$

$$\frac{dN_p}{dt_{\parallel}} = -N_p \left(1 + \sum_q I_q \right) + \frac{1}{2} D_0 I_p + \frac{1}{2} \sum_q D_{p-q} I_q. \quad (3.12)$$

$$p = 1, \dots, N, \quad r = 1, \dots, N-1.$$

In these equations, we have slightly modified the notations, reserving D_x to the low spatial frequency gratings and using N_x to designate the high frequency gratings. The parameter κ , which is the ratio of the population inversion lifetime to the photon lifetime, is typically a very large number, of the order of 10^3 to 10^6 [1, 16]. It is therefore natural to think of adiabatically eliminating the field variables. However, a linear stability analysis of the resulting equations would show that the transient toward equilibrium is exponential and free from oscillations. This does not correspond to the experimental observations, which reveal an important oscillatory dynamics in the laser. Consequently, the modal intensities must be kept as “active” dynamical variables in the model. Finally, we note that the TSD equations can be deduced from Eqs. (3.9) to (3.12) by setting $w_{r>0} = D_{r>0} = 0$.

3.3 Antiphase Dynamics

A remarkable feature of the transient behavior of a multimode laser towards its steady state is antiphase dynamics: while N distinct relaxation frequencies are observable in the transient of the modal intensities I_p , the total intensity $I_{tot} = \sum_p I_p$ oscillates with only one frequency [17, 18, 19]. This property of self-organization was also reported in the self-pulsing regimes of solid state lasers subjected to feedback [20], and in lasers with intracavity second-harmonic generation [21, 22]. Besides these experimental and numerical investigations, the presence of antiphase dynamics was demonstrated analytically in the TSD equations [1, 12, 23]. Let us extend the demonstration in the TSD⁺ model. To this end, we perturb the steady state solution of Eqs. (3.9) to (3.12) in the following way

$$\begin{aligned} D_q(t_{\parallel}) &= \bar{D}_q + \varepsilon^2 d_q(\tau) + O(\varepsilon^3), \\ N_q(t_{\parallel}) &= \bar{N}_q + \varepsilon^2 n_q(\tau) + O(\varepsilon^3), \\ I_q(t_{\parallel}) &= \bar{I}_q + \varepsilon i_q(\tau) + O(\varepsilon^2), \\ \tau &= \varepsilon t_{\parallel}. \end{aligned}$$

where \bar{D}_q , \bar{N}_q and \bar{I}_q denote steady state values and $\varepsilon = \kappa^{-1/2} \ll 1$. We assume that the gain curve of the atomic transition is flat over the frequency spread of the lasing mode:

$\mathcal{L}_q = 1 - \varepsilon^2 \ell_q + O(\varepsilon^3)$. With this assumption, Eqs. (3.9), (3.10), and (3.12) yield for the steady state solution the following relations:

$$\bar{N}_p = 2(\bar{D}_0 - 1) + O(\varepsilon), \quad (3.13)$$

$$w_0 = \bar{D}_0 + \sum_p \bar{I}_p + O(\varepsilon), \quad (3.14)$$

$$2(\bar{D}_0 - 1) \left(1 + \sum_q \bar{I}_q \right) = \frac{1}{2} \bar{D}_0 \bar{I}_p + \frac{1}{2} \sum_q \bar{D}_{p-q} \bar{I}_q + O(\varepsilon). \quad (3.15)$$

In the first order in ε , we obtain

$$\frac{di_p}{d\tau} = \bar{I}_p \left(d_0 - \frac{n_p}{2} \right) + O(\varepsilon), \quad (3.16)$$

$$\frac{dd_0}{d\tau} = - \sum_q i_q + O(\varepsilon), \quad (3.17)$$

$$\frac{dn_p}{d\tau} = -\bar{N}_p \sum_q i_q + \frac{1}{2} \bar{D}_0 i_p + \frac{1}{2} \sum_q \bar{D}_{p-q} i_q + O(\varepsilon). \quad (3.18)$$

Derivating (3.16) with respect to τ , summing over p and using relations (3.13) to (3.15), one obtains

$$\left(\frac{d^2}{d\tau^2} + w_0 - 1 \right) \left(\sum_p i_p \right) = 0 \quad (3.19)$$

which is the property we wanted to prove: deviations from the total steady state intensity oscillate with only one frequency, the single mode relaxation oscillation frequency, no matter how many modes are lasing in the cavity. The total intensity is therefore a global variable, revealing self-organization in multimode lasers. This point is clearly illustrated in Fig. 3.2, which shows the relaxation of the modal and total intensities towards stationary state. The dimensionless oscillation frequency is $\sqrt{\kappa(w_0 - 1)}$, or equivalently $\sqrt{\Gamma_c \gamma_{||}} (w_0 - 1)$ in s^{-1} , where Γ_c and $\gamma_{||}$ are, respectively, the cavity and inversion damping rates. This frequency is sometimes referred to as the “McCumber frequency” [24], and is noted Ω_R .

3.4 Analysis of a three-mode laser

In this section, we study the TSD⁺ model for a three-mode laser. For simplicity, we assume that the central mode is resonant with the atomic transition, whereas the side modes are equally detuned from the atomic line (Fig. 3.1). This amounts to impose $\mathcal{L}_1 = \mathcal{L}_3 = \mathcal{L} \leq 1$ and $\mathcal{L}_2 = 1$ in Eqs. (3.9) to (3.12).

In order to assess the influence of a nonuniform pump profile on the laser dynamics, it is instructive to consult the TSD model first [12]. For the present set of modal gains \mathcal{L}_j , it predicts the following scenario, as the only pump parameter w_0 is increased from zero.

1. For $w_0 < 1$, all modal intensities vanish.
2. As w_0 surpasses the threshold $w_{th,1} = 1$, the central mode starts to lase, the other modes remaining extinct.

3. Finally, for $w_0 > w_{th,2} = \mathcal{L}^{-1}$ all three modes lase with a constant intensity. No other stable solution exists for this configuration.

In addition, depending on the number of lasing modes, up to two frequencies, Ω_R and Ω_L , characterize the relaxation towards steady state.

For a three-mode laser, the TSD⁺ model assumes the following pump profile

$$w(z) = w_0 + w_1 \cos(2\pi z/L) + w_2 \cos(4\pi z/L). \quad (3.20)$$

A key feature of the present analysis is that there are regions inside the cavity where longitudinal modal intensity distributions do almost not overlap for pairs of modes. In particular, for the pairs of consecutive modes (I_1, I_2) and (I_2, I_3) , this happens at $z = L/2$. For the pairs (I_1, I_3) , on the other hand, minimal overlap is at $z = L/2 \pm L/4$. By tuning w_1 and w_2 one can

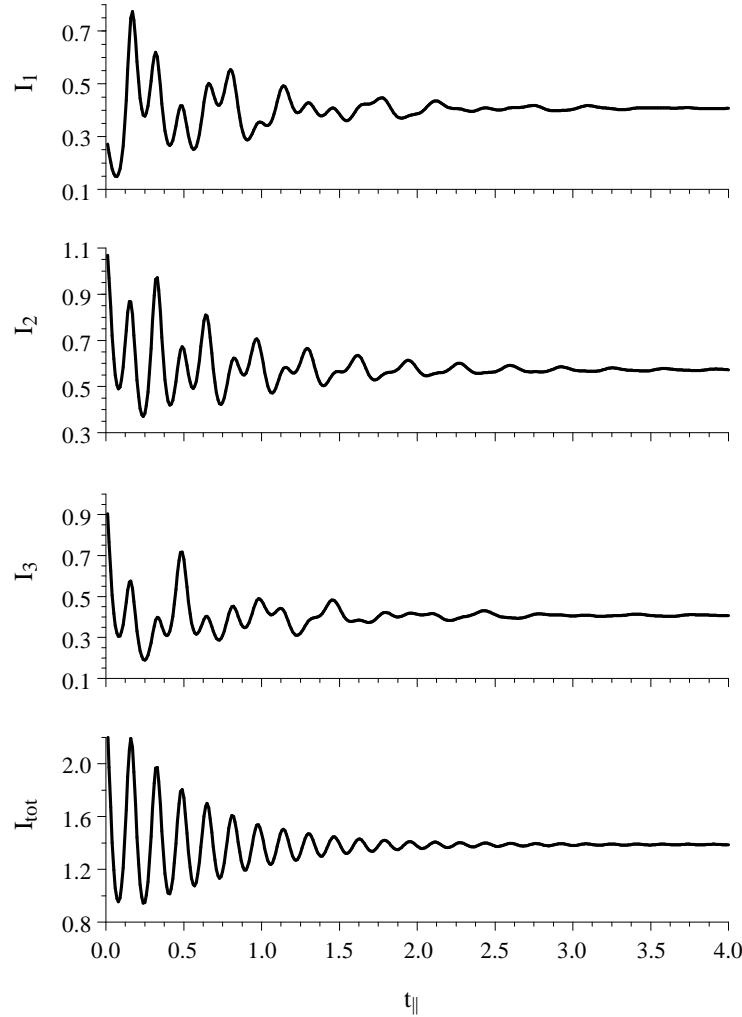


Figure 3.2: Temporal evolution of the modal intensities illustrating antiphase dynamics. The transient of each modal intensity contains multiple frequencies, while the total output consists of damped oscillations with only one frequency. Parameter values: $\kappa = 1000$, $w_0 = 2.5$, $w_1 = -1$, $w_2 = 1$, $\mathcal{L}_{1,3} = 0.99$, and $\mathcal{L}_2 = 1$.

Table 3.1: Modal selection as a function of the pump profile $w(z) = w_0 + w_1 \cos(2\pi z/L) + w_2 \cos(4\pi z/L)$. The pulsations of modes 2 and 3 are $\omega_2 = \omega_1 + \pi c/L$ and $\omega_3 = \omega_1 + 2\pi c/L$.

	maximum pump profile	minimum pump profile	favored pairs	quenched pairs
$w_1 > 0$	$z=0, L$	$z=L/2$		$(I_1, I_2) \& (I_2, I_3)$
$w_1 < 0$	$z=L/2$	$z=0, L$	$(I_1, I_2) \& (I_2, I_3)$	
$w_2 > 0$	$z=0, L/2, L$	$z=L/4, 3L/4$	$(I_1, I_2) \& (I_2, I_3)$	(I_1, I_3)
$w_2 < 0$	$z=L/4, 3L/4$	$z=0, L/2, L$	(I_1, I_3)	$(I_1, I_2) \& (I_2, I_3)$

intensify or diminish the pump precisely in these regions of the cavity. Therefore, through the mechanism of spatial hole burning, one can expect more (less) efficient laser amplification for such pairs of mode with increased (lowered) pump intensity in these regions. Hence, a non uniform pump distribution alters mode competition. While w_0 determines the total energy injected in the laser, the role of w_1 and w_2 is to distribute this energy among the modes of the cavity. A classification of the possible situations is given in Table 3.1.

Using the same geometrical argument, we can state more generally that tuning the pump parameter w_r affects the competition between pairs of modes (I_p, I_{p+r}) .

3.4.1 Steady states and stability

The steady state solutions can be classified in relation to the number of nonzero modal intensities. Their detailed expressions and stability conditions are given in Appendix 3.A. We outline the differences with the TSD model below:

1. Beyond the second lasing threshold $w_0 > w_{th,2}$, the medium has sufficient gain for all the modes to lase. In contrast with the TSD predictions, both monomode solutions with $\bar{I}_1 \neq 0$ and $\bar{I}_3 \neq 0$ can be stable, besides solution $\bar{I}_2 \neq 0$. This requires that $w_1 > w_1^*$ and $w_2 > w_2^*$, where w_1^* and w_2^* are given by (3.36) and (3.37). If these two conditions are fulfilled, the mode competition is enhanced between all pairs of mode (see Table 1). As a consequence, if initially $I_i(0), I_j(0) \ll I_k(0)$, then $I_k(t_{||})$ tends to a nonzero steady state value, suppressing the other modes through a winner-takes-all dynamics. Figure 3.3 illustrates this point: for the same parameter values but different initial conditions, either $\bar{I}_1 \neq 0$ or $\bar{I}_2 \neq 0$ emerge.
2. Other steady state solutions that can be stable in the TSD⁺ model but not in the TSD version are the two-mode solutions, either with $\{\bar{I}_{1,2} \neq 0, \bar{I}_3 = 0\}$, $\{\bar{I}_{1,3} \neq 0, \bar{I}_2 = 0\}$ or $\{\bar{I}_{2,3} \neq 0, \bar{I}_1 = 0\}$. The stability conditions (3.41), (3.42) and (3.47) indicates that in all cases, either of \bar{D}_1 and \bar{D}_2 should be larger than $2\bar{D}_0$. It would be a mistake, though, to deduce that the corresponding stationnary inversion profile $\bar{D}(z)$ necessarily passes by zero. As a counter-example, consider a profile $\bar{D}(z)$ that is constant in a small fraction of the cavity and zero elsewhere. Its limited Fourier series $\bar{D}_0 + \bar{D}_1 \cos(2\pi z/L) + \bar{D}_2 \cos(4\pi z/L)$ can be negative for some values of z . This situation was encountered when investigating the effect of a partial filling of the cavity with the laser medium [25].
3. Finally, for a deep spatial modulation of the pump profile $w(z)$, steady state solutions can undergo Hopf bifurcations. Such instabilities, however, only affect multimode

solutions. They give rise to stable periodic solutions. For the two-mode solutions and in the limit $\mathcal{L}_j \rightarrow 1$, the Hopf bifurcation points assume simple expressions. On the one hand, the Hopf instability of the solution $\{\bar{I}_{1,2} \neq 0, \bar{I}_3 = 0\}$ arises at $w_{1,H} = -10w_0$. On the other hand, for the solution $\{\bar{I}_{1,3} \neq 0, \bar{I}_2 = 0\}$, it takes place at $w_{2,H} = -10w_0$. As either of w_1 and w_2 is further decreased a period-doubling bifurcation occurs, followed by chaos.

Considering the proof of global stability of Eqs. (3.2) and (3.3), the presence of bistability and self-pulsing may seem spurious and only due to the TSD⁺ truncation. The apparent contradiction is resolved, however, by noting that such situations occur only if the steady state population profile $\bar{D}(z) \simeq \bar{D}_0 + \bar{D}_1 \cos(2\pi z/L) + \bar{D}_2 \cos(4\pi z/L)$ is somewhere negative in the cavity. In this case, the function \mathcal{F} given by (3.4) can not be a Lyapunov function of the system anymore.

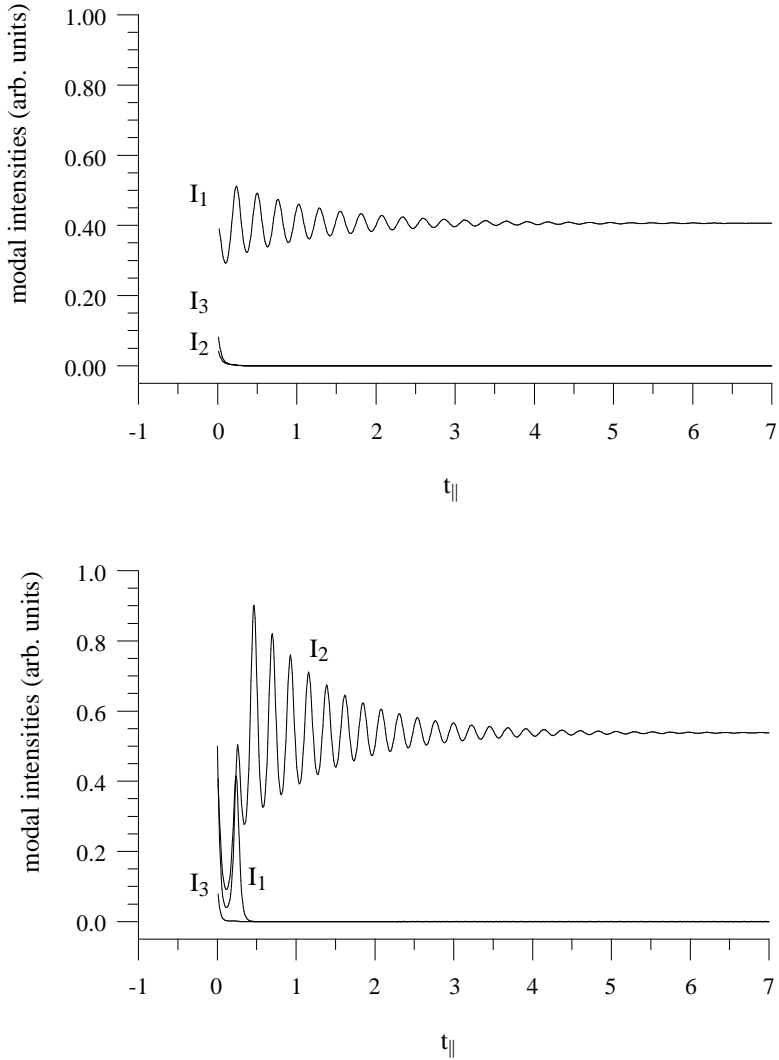


Figure 3.3: Temporal evolution of the modal intensities. Parameter values: $\kappa = 1000$, $w_0 = 1.75$, $w_1 = 6$, $w_2 = 4$, $\mathcal{L}_{1,3} = 0.9$, and $\mathcal{L}_2 = 1$. Depending on the initial conditions, different steady states emerge.

3.4.2 Self-pulsing solutions: physical mechanism

The existence of self-pulsation in the laser output relies on two facts. Firstly, a negative inversion exists somewhere in the cavity. At this point, the medium is a saturable absorber for the laser field. This alone is not sufficient to destabilize the constant intensity operation because the saturable absorber has the same characteristics as the amplifier, as we noted it when studying the dynamics of a laser with saturable absorber. Secondly, the laser operates in the multimode regime. As already pointed out, the overlap between cavity eigenmodes varies along the cavity axis. In the gain regions, this overlap is minimum between the excited modes. Consequently, the saturation of amplification is also minimum. On the contrary, in the regions of absorption, the excited modes strongly overlap and the saturation of the medium's response is more important. This is illustrated in Fig. 3.4 for modes 1 and 2. The difference of saturation caused by multimode operation thus permits the onset of self-pulsing.

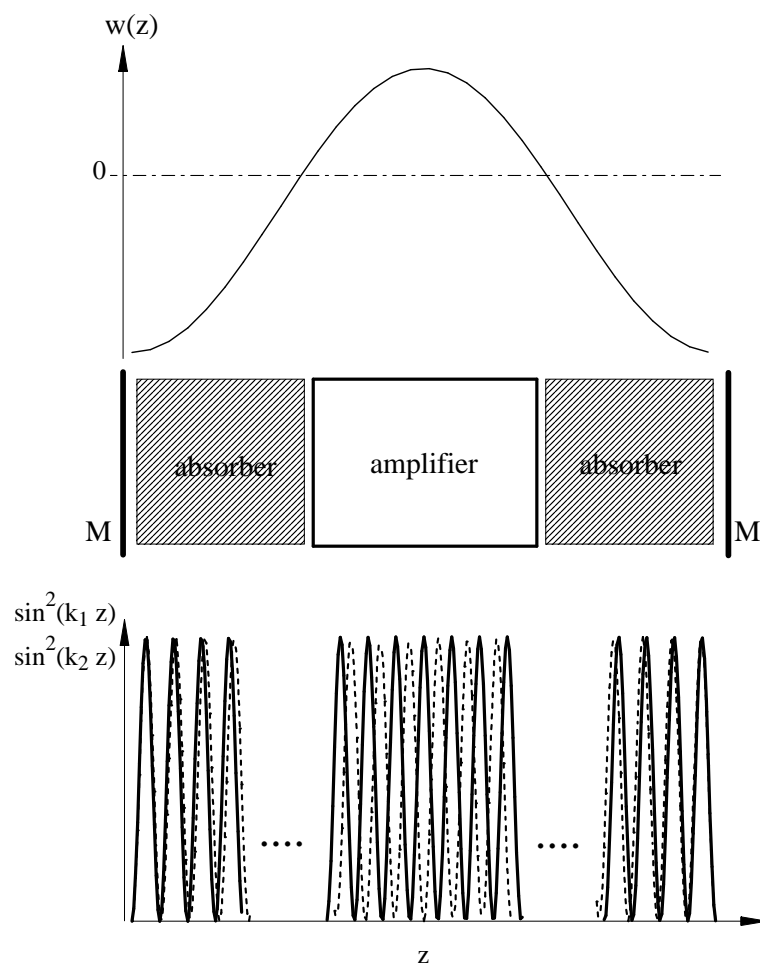


Figure 3.4: Intensity overlap between consecutive cavity eigenmodes and pump spatial distribution leading to self-pulsing. In the center of the figure, the laser medium and cavity mirrors (M) are represented schematically.

To conclude this interpretation, let us mention that not all laser materials can display negative inversion of population. Indeed, in the so-called four-level atomic systems [26], which include neodymium, the lower level of the optical transition has a very short lifetime compared to the upper level. A negative inversion, caused by a lack of pumping, is therefore impossible. Examples of laser materials that do absorb the laser field if not pumped are ruby [26], holmium (Ho) and thulium (Tm) [27], and semiconductors.

3.4.3 Self-pulsing solutions: analytical treatment

The linear stability analysis giving the Hopf bifurcation is rather complicated algebraically. As shown in Fig. 3.5, close to bifurcation point, the solution assumes a pulsed behavior. To describe this part, we propose to seek a solution of the form:

$$\begin{aligned} I_p(t_{\parallel}) &= \varepsilon^{2-2x} i_p(\tau_x), \quad D_p(t_{\parallel}) = w_p + \varepsilon^{2-x} d_p(\tau_x), \quad N_p(t_{\parallel}) = \varepsilon^{2-x} n_p(\tau_x), \\ \varepsilon &= \kappa^{-1/2}, \quad \tau_x = \varepsilon^{-x} t_{\parallel}, \quad 0 < x < 1. \end{aligned} \quad (3.21)$$

Above, τ_x is the timescale of the interpulse and is not fixed *a priori*. Moreover, we assume that the average pump parameter is close to the lasing threshold and that the modal gains are close to unity: $w_0 = 1 + \varepsilon^{2-x} \bar{w}_0$, $\mathcal{L}_q = 1 - \varepsilon^{2-x} \ell_q$. In the leading order, we thus obtain

$$\frac{di_p}{d\tau_x} = \left(\bar{w}_0 - \ell_p + d_0 - \frac{n_p}{2} \right) i_p + O(\varepsilon^{2-x}), \quad (3.22)$$

$$\frac{dd_0}{d\tau_x} = -w_0 \sum_q i_q + O(\varepsilon^x), \quad (3.23)$$

$$\frac{dn_p}{d\tau_x} = \frac{1}{2} w_0 i_p + \frac{1}{2} \sum_q w_{p-q} i_q + O(\varepsilon^x). \quad (3.24)$$

For the nonzero modal intensities, we may pose $y_p = \ln i_p$, and obtain the set of nonlinear equations

$$\frac{d^2 y_p}{d\tau_x^2} = -\frac{1}{4} w_0 \exp y_p - \sum_q \left(w_0 + \frac{w_{p-q}}{4} \right) \exp y_q + O(\varepsilon^x). \quad (3.25)$$

For some domain of parameter values, the solution of this equation diverge at a finite time. This corresponds to the emergence of a pulse in the original set of equations. As τ_x tends to the time of divergence τ_x^* , we try the ansatz $y_p(\tau_x) = A_p + B_p \ln(|\tau_x - \tau_x^*|)$. Substituting into (3.25), we obtain, $B_p = -2$, and the following set of algebraic equations

$$2 = -\frac{1}{4} w_0 e^{A_p} - \sum_q \left(w_0 + \frac{w_{p-q}}{4} \right) e^{A_q}. \quad (3.26)$$

Let us solve this system in the two-mode and three-mode cases. First, if the self-pulsing solution is bimodal with $\{\bar{I}_{1,2} \neq 0, \bar{I}_3 = 0\}$ then one has only two equations

$$\begin{aligned} 2 &= -\frac{3}{2} w_0 e^{A_1} - \left(w_0 + \frac{w_1}{4} \right) e^{A_2}, \quad 2 = -\frac{3}{2} w_0 e^{A_2} - \left(w_0 + \frac{w_1}{4} \right) e^{A_1}, \\ \Rightarrow e^{A_1} &= e^{A_2} = \frac{-8}{10w_0 + w_1}. \end{aligned}$$

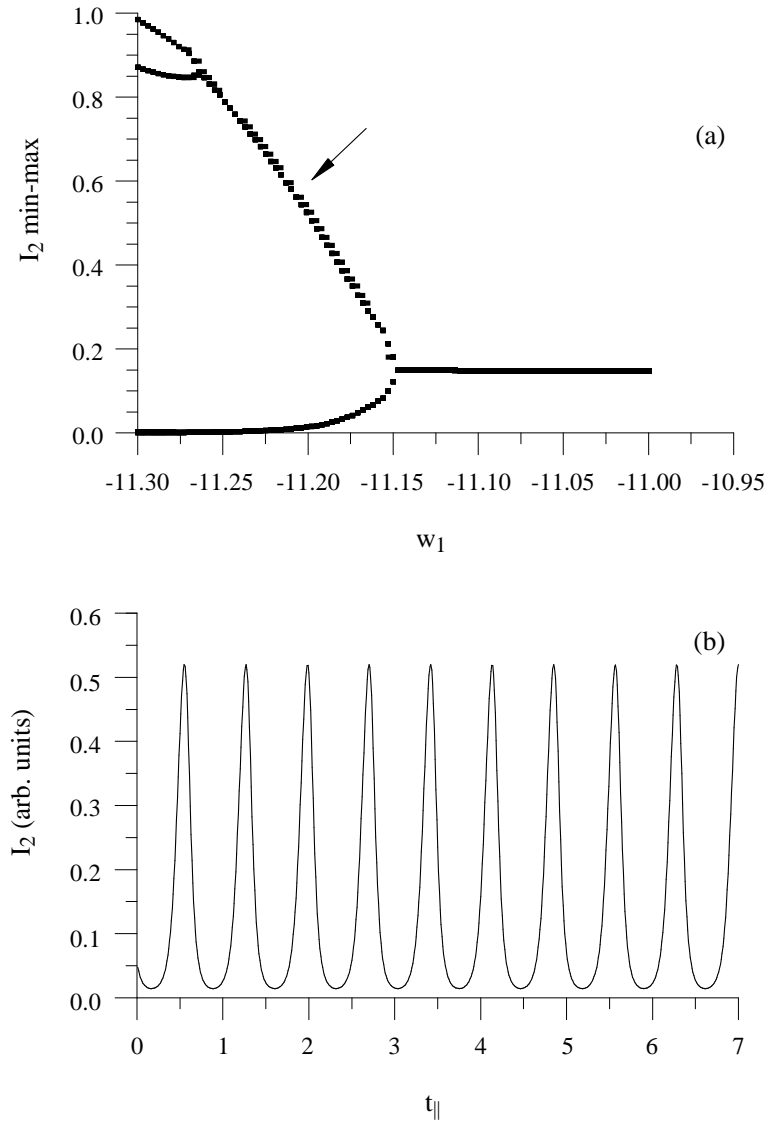


Figure 3.5: a) Bifurcation diagram with $\kappa = 1000$, $w_0 = 1.1$, $w_2 = 4$, $\mathcal{L}_{1,3} = 0.99$, and $\mathcal{L}_2 = 1$. w_1 is varied in the range $[-11.3, -11]$. Minima and maxima of I_2 are plotted versus w_1 . b) Temporal trace of I_2 for $w_1 = -11.2$, showing a pulsed behavior.

Hence such an interpulse solution exists only if $w_1 < -10w_0$, which is precisely the Hopf bifurcation condition found from a linear stability analysis. In the same way, the condition $w_2 < 10w_0$ is obtained for the periodic solution with $\{\bar{I}_{1,3} \neq 0, \bar{I}_2 = 0\}$. Next, for the three-mode self-pulsing solution, one has the set of equations

$$8 = -6w_0e^{A_1} - (4w_0 + w_1)e^{A_2} - (4w_0 + w_2)e^{A_3}, \quad (3.27)$$

$$8 = -(4w_0 + w_1)e^{A_1} - 6w_0e^{A_2} - (4w_0 + w_1)e^{A_3}, \quad (3.28)$$

$$8 = -(4w_0 + w_2)e^{A_1} - (4w_0 + w_1)e^{A_2} - 6w_0e^{A_3}, \quad (3.29)$$

$$\Rightarrow e^{A_1} = e^{A_3} = \frac{8w_0 - 4w_1}{f(w_0, w_1, w_2)}, \quad e^{A_2} = \frac{8w_0 - 8w_1 + 4w_2}{f(w_0, w_1, w_2)},$$

$$f(w_0, w_1, w_2) = -14w_0^2 + 8w_0w_1 + w_1^2 - 3w_0w_2. \quad (3.30)$$

The condition of existence for the periodic solution is therefore given by $f(w_0, w_1, w_2) > 0$, in good agreement with the numerical simulations.

We have constructed in this way, in the self-pulsing domain, a solution of small amplitude, being of order ε^{2-2x} , which is expected to connect two consecutive pulses. The presence of the pulse is attested by the divergence. The so far unspecified timescale parameter x and pulse time τ_x^* would be determined by matching conditions with the pulse part of the solution. It is tempting to say that it is not a solution that emerges from the Hopf bifurcation since the solution should be harmonic in time close to the bifurcation point and hence that the bifurcation is subcritical. Actually, the bifurcation diagram in Fig. 3.5 shows that the bifurcation is supercritical for the chosen set of parameters. The oscillations that are harmonic close to the bifurcation point already acquire higher harmonics as $w_1 - w_{1,H} = \mathcal{O}(\varepsilon)$. Such singular behavior, connected to the presence of a small parameter in the equations is reminiscent to our study of a laser with a weakly saturable absorber. This consolidates our interpretation of the phenomenon. Finally, numerical simulations indicate that period doubling and chaos follow the periodic intensity pulsations (Fig. 3.5) for deeper spatial modulations of the pump profile.

3.5 Conclusion

The TSD⁺ model extends the TSD model by the inclusion of low spatial frequency Fourier components of the inversion profile $D(z, t_{\parallel})$ in the rate equations. We concluded from geometrical considerations that the competition between lasing modes p and q is strongly affected by the component D_{p-q} . In the particular case of a three-mode laser, we found that the effect can be sufficiently important to generate new stable steady states. In principle, this should remain true for a laser emitting on more than three modes. The investigations reported in [25] for five modes support this view. For extreme spatial modulations of the pump profile, the multimode steady states can be destabilized by Hopf bifurcations. We have provided a physical explanation of this phenomenon in terms of saturable absorption combined with multimode operation. We note that this instability could find application in semiconductor lasers as a means to produce controlled intensity pulses without the need of a different material as a saturable absorber. In these devices, the modulation of the pump profile over the cavity length can easily be achieved by a proper design of the electrodes. Besides self-pulsing, we found that it is possible to observe bistability between different steady-states. These two features, which had been regarded as impossible since the discovery of the Lyapunov function (3.4), are easily explained by the fact that the steady state inversion $\bar{D}(z)$ passes by zero. Moreover, we showed that the important property of antiphase dynamics still exists in the new model, in agreement with experimental observations. It seems that this property is generic of multimode homogeneously broaden lasers and that its validity extends beyond the vicinity of the steady state. For instance, it was found numerically to persist in the chaotic state of a laser with modulated losses [28]. In the present case too, preliminary numerical situation tend to show that antiphase dynamics persist in the strongly pulsating and chaotic domain.

To close this chapter, we refer to [25] again, where the TSD⁺ model was compared to the global rate Eqs. (3.2) and (3.3) through numerical simulations. It was concluded that the TSD⁺ model is a very good approximation, considering its relative simplicity.

Appendix to Chapter 3

3.A Details of the linear stability analysis

In this Appendix, we present the steady state solutions and the conditions of their linear stability. These results are obtained by substituting eigenvalues of the form $\lambda = \varepsilon^{-1}\lambda_{-1} + \lambda_0 + \varepsilon\lambda_1 + \dots$ with $\varepsilon = \sqrt{\kappa}$ in the characteristic polynomials and solving for $\varepsilon \rightarrow 0$. Although the external parameters of the system are w_0 , w_1 , and w_2 , it is much more convenient, from algebraic point of view, to parametrize the solutions in terms of the steady state values \bar{D}_0 , \bar{D}_1 , \bar{D}_2 . This leads us to formulate for each solution the set of functions $\bar{I}_j(\bar{D}_0, \bar{D}_1, \bar{D}_2)$, $\bar{N}_j(\bar{D}_0, \bar{D}_1, \bar{D}_2)$, and $w_j(\bar{D}_0, \bar{D}_1, \bar{D}_2)$.

Before going into details, we identify a general stability condition for solutions having $\bar{I}_q = 0$:

$$\bar{N}_q(\bar{D}_0, \bar{D}_1, \bar{D}_2) > 2(\bar{D}_0 - \mathcal{L}_q^{-1}). \quad (3.31)$$

Otherwise, the mode q starts lasing. Most other stability conditions are too complicated to be expressed for arbitrary values of \mathcal{L}_q . We will therefore give them only in the limit $\mathcal{L}_q \rightarrow 1$.

Trivial solution

It is given by $\bar{I}_j = \bar{N}_j = 0$, $\bar{D}_j = w_j$ and it is linearly stable if and only if $w_0 < 1$.

Monomode solution $\{\bar{I}_1 \neq 0, \bar{I}_{2,3} = 0\}$

It is given by

$$\bar{I}_2 = \bar{I}_3 = 0, \quad \bar{I}_1 = 2 \frac{\mathcal{L}\bar{D}_0 - 1}{2 - \mathcal{L}\bar{D}_0}, \quad (3.32)$$

$$\begin{aligned} \bar{N}_1 &= 2(\bar{D}_0 - \mathcal{L}^{-1}), \quad \bar{N}_2 = \bar{D}_1 \frac{\bar{D}_0 - \mathcal{L}^{-1}}{\bar{D}_0}, \quad \bar{N}_3 = \bar{D}_2 \frac{\bar{D}_0 - \mathcal{L}^{-1}}{\bar{D}_0}, \\ w_0 &= \frac{-\mathcal{L}\bar{D}_0^2 + 4\bar{D}_0 - 2\mathcal{L}^{-1}}{2 - \mathcal{L}\bar{D}_0}, \quad w_1 = \bar{D}_1 \frac{2\bar{D}_0 - \mathcal{L}^{-1}}{\bar{D}_0(2 - \mathcal{L}\bar{D}_0)}, \quad w_2 = w_1 \frac{\bar{D}_2}{\bar{D}_1}. \end{aligned} \quad (3.33)$$

The solution $\{\bar{I}_3 \neq 0, \bar{I}_{1,2} = 0\}$ is obtained by permuting (\bar{I}_1, \bar{N}_1) and (\bar{I}_3, \bar{N}_3) . This solution is physically acceptable if $\bar{I}_1 > 0$, that is if $\mathcal{L}^{-1} < \bar{D}_0 < 2\mathcal{L}^{-1}$.

In the limit $\mathcal{L} \rightarrow 1$, it is linearly stable if

$$\bar{D}_1 > 2\bar{D}_0, \quad (3.34)$$

$$\bar{D}_2 > 2\bar{D}_0. \quad (3.35)$$

One can therefore parametrize the stability boundaries in the parameter space (w_0, w_1, w_2) by

$$(w_0, w_1^*, w_2) = \left(\frac{-\delta^2 + 4\delta - 2}{2 - \delta}, 2 \frac{2\delta - 1}{2 - \delta}, \eta \right), \quad (3.36)$$

$$(w_0, w_1, w_2^*) = \left(\frac{-\delta^2 + 4\delta - 2}{2 - \delta}, \eta, 2 \frac{2\delta - 1}{2 - \delta} \right), \quad \delta \in]1, 2[, \quad \eta \in]\infty, \infty[\quad (3.37)$$

The linear stability analysis also reveals damped oscillation with frequency $\Omega_R = \sqrt{\kappa(w_0 - 1)}$.

Monomode solution $\{\bar{I}_2 \neq 0, \bar{I}_{1,3} = 0\}$

It is given by

$$\begin{aligned} \bar{I}_2 &= 2 \frac{\bar{D}_0 - 1}{2 - \bar{D}_0}, \quad \bar{I}_1 = \bar{I}_3 = 0, \quad \bar{N}_2 = \bar{D}_0 - 1, \quad \bar{N}_1 = \bar{N}_3 = \bar{D}_1 \frac{\bar{D}_0 - 1}{\bar{D}_0}, \\ w_0 &= \frac{-\bar{D}_0^2 + 4\bar{D}_0 - 2}{2 - \bar{D}_0}, \quad w_1 = w_0 \frac{\bar{D}_1}{\bar{D}_0}, \quad w_2 = \frac{\bar{D}_0 \bar{D}_2}{2 - \bar{D}_0}. \end{aligned} \quad (3.38)$$

The positivity of \bar{I}_2 requires $1 < \bar{D}_0 < 2$. This constraint determines \bar{D}_0 as a function of w_0 in a unique way when the system is in state $\{I_2\}$.

In the limit $\mathcal{L} \rightarrow 1$, it is stable provided that

$$\bar{D}_1 > 2\bar{D}_0. \quad (3.39)$$

Moreover the linearized system of equation admits solutions with damped oscillations at frequency $\Omega_R = \sqrt{\kappa(w_0 - 1)}$.

Two-mode solution $\{\bar{I}_{1,2} \neq 0, \bar{I}_3 = 0\}$

This solution is

$$\begin{aligned} \bar{I}_1 &= 4 \frac{(\bar{D}_0 - 1)\bar{D}_1 - 2\bar{D}_0(\bar{D}_0 - \mathcal{L}^{-1})}{(\bar{D}_1 - 2\bar{D}_0)(\bar{D}_1 - 6\bar{D}_0 + 4(1 + \mathcal{L}^{-1}))}, \quad \bar{I}_2 = 4 \frac{\bar{D}_1(\bar{D}_0 - \mathcal{L}^{-1}) - 2\bar{D}_0(\bar{D}_0 - 1)}{(\bar{D}_1 - 2\bar{D}_0)(\bar{D}_1 - 6\bar{D}_0 + 4(1 + \mathcal{L}^{-1}))}, \\ \bar{I}_3 &= 0, \quad N_2 = 2(\bar{D}_0 - 1), \quad N_1 = 2(\bar{D}_0 - \mathcal{L}^{-1}), \\ N_3 &= \left\{ \bar{D}_1 \left[\frac{\bar{D}_1}{2} (\bar{D}_0 - \mathcal{L}^{-1}) - \bar{D}_0 (\bar{D}_0 - 1) \right] + \bar{D}_2 \left[\frac{\bar{D}_1}{2} (\bar{D}_0 - 1) - \bar{D}_0 (\bar{D}_0 - \mathcal{L}^{-1}) \right] \right\} \left[\frac{\bar{D}_1^2}{4} - \bar{D}_0^2 \right]^{-1}, \\ w_0 &= \bar{D}_0 + \mathcal{L}^{-1}\bar{I}_1 + \bar{I}_2, \quad w_1 = (1 + \bar{I}_2 + \bar{I}_1)\bar{D}_1 - \frac{1}{2}(\bar{I}_1 N_2 + \bar{I}_2(N_1 + N_3)), \\ w_2 &= (1 + \bar{I}_1 + \bar{I}_2)\bar{D}_2 - \frac{1}{2}\bar{I}_1 N_3. \end{aligned} \quad (3.40)$$

The solution $\{\bar{I}_{2,3} \neq 0, \bar{I}_1 = 0\}$ is obtained by permuting (\bar{I}_1, \bar{N}_1) and (\bar{I}_3, \bar{N}_3) . In the limit $\mathcal{L} \rightarrow 1$, two stability conditions are

$$\bar{D}_2 > 2\bar{D}_0, \quad (3.41)$$

$$\bar{D}_1 < 2\bar{D}_0. \quad (3.42)$$

We find a frequency $\Omega_L = \sqrt{\kappa\bar{I}_2(2\bar{D}_0 - \bar{D}_1)/4}$ associated to damped oscillations. In addition, there is a pair of complex conjugate roots that have their imaginary part equal to the McCumber frequency

$$\lambda_{3,\pm} = a \pm i\Omega, \quad \Omega = \Omega_R + O(\kappa^{-1/2}), \quad a = -\frac{w_1 + 10w_0}{2(16 - 6\bar{D}_0 + \bar{D}_1)} + O(\kappa^{-1}). \quad (3.43)$$

The real part of this pair of roots is positive if $w_1 + 10w_0 < 0$. In that case, the system undergoes a Hopf bifurcation.

Two-mode solution $\{\bar{I}_{1,3} \neq 0, \bar{I}_2 = 0\}$

This solution is

$$\bar{I}_2 = 0, \quad \bar{I}_1 = \bar{I}_3 = 4 \frac{\mathcal{L}\bar{D}_0 - 1}{8 - 6\mathcal{L}\bar{D}_0 + \mathcal{L}\bar{D}_2}, \quad (3.44)$$

$$\begin{aligned} \bar{N}_2 &= 2\bar{D}_1 \frac{\bar{D}_0 - \mathcal{L}^{-1}}{\bar{D}_0 + \bar{D}_2/2}, \quad \bar{N}_1 = \bar{N}_3 = 2(\bar{D}_0 - \mathcal{L}^{-1}), \\ w_0 &= \frac{16\bar{D}_0 - 6\mathcal{L}\bar{D}_0^2 + \mathcal{L}\bar{D}_2\bar{D}_0 - 8\mathcal{L}^{-1}}{8 - 6\mathcal{L}\bar{D}_0 + \mathcal{L}\bar{D}_2}, \end{aligned} \quad (3.45)$$

$$\begin{aligned} w_1 &= \frac{\bar{D}_1(4 - 2\mathcal{L}\bar{D}_0 + \mathcal{L}\bar{D}_2)(-4 + 6\mathcal{L}\bar{D}_0 + \mathcal{L}\bar{D}_2)}{\mathcal{L}(2\bar{D}_0 + \bar{D}_2)(8 - 6\mathcal{L}\bar{D}_0 + \mathcal{L}\bar{D}_2)}, \\ w_2 &= \frac{\mathcal{L}\bar{D}_2^2 - 8\mathcal{L}\bar{D}_0^2 + 2\mathcal{L}\bar{D}_0\bar{D}_2 + 16\bar{D}_0 - 8\mathcal{L}^{-1}}{8 - 6\mathcal{L}\bar{D}_0 + \mathcal{L}\bar{D}_2}. \end{aligned} \quad (3.46)$$

The positivity of the intensities requires $(\bar{D}_0 - \mathcal{L}^{-1})(8 - 6\mathcal{L}\bar{D}_0 + \mathcal{L}\bar{D}_2) > 0$.

In the limit $\mathcal{L} \rightarrow 1$, stability requires

$$\bar{D}_1 > 2\bar{D}_0 + \bar{D}_2, \quad (3.47)$$

which implies a depletion of the inversion profile at the center of the cavity and therefore a competition between mode 1 and modes 2 and 3. If this condition is not fulfilled, a transition to the three-mode solution $\{\bar{I}_{1,2,3} \neq 0\}$ takes place. We find a frequency $\Omega_L = \sqrt{\kappa\bar{I}_1(2\bar{D}_0 - \bar{D}_1)/4}$ associated to damped oscillations. In addition, there is a pair of complex conjugate roots associated with the McCumber frequency

$$\lambda_{5,\pm} = a \pm i\Omega, \quad \Omega = \Omega_R + O(\kappa^{-1/2}), \quad a = -\frac{w_2 + 10w_0}{2(16 - 6\bar{D}_0 + \bar{D}_2)} + O(\kappa^{-1}). \quad (3.48)$$

A Hopf bifurcation therefore occurs at $w_2 + 10w_0 = 0$.

Three-mode solution $\{\bar{I}_{1,2,3} \neq 0\}$

This solution is given by

$$\begin{aligned}
\bar{N}_2 &= 2(\bar{D}_0 - 1), \quad \bar{N}_1 = \bar{N}_3 = \bar{N} = 2(\bar{D}_0 - \mathcal{L}^{-1}), \\
\bar{I}_2 &= [4\bar{N}\bar{D}_1 - \bar{N}_1(2\bar{D}_0 + \bar{D}_2)]M^{-1}, \quad \bar{I}_1 = \bar{I}_3 = \bar{I} = (\bar{N}_1\bar{D}_1 - 2\bar{N}\bar{D}_0)M^{-1}, \\
w_0 &= \bar{D}_0 + \mathcal{L}\bar{I}_1 + \bar{I}_2 + \mathcal{L}\bar{I}_3, \quad w_2 = (1 + \bar{I}_2 + \bar{I}_1 + \bar{I}_3)\bar{D}_2 - \frac{1}{2}(\bar{I}_1\bar{N}_3 + \bar{I}_3\bar{N}_1), \\
w_1 &= (1 + \bar{I}_2 + \bar{I}_1 + \bar{I}_3)\bar{D}_1 - \frac{1}{2}[\bar{I}_1\bar{N}_2 + \bar{I}_2(\bar{N}_1 + \bar{N}_3) + \bar{I}_3\bar{N}_2]. \tag{3.49}
\end{aligned}$$

where

$$M = \bar{D}_1 [\bar{D}_1 - 2(\bar{N} + \bar{N}_2)] + \bar{D}_0 [4\bar{N} + 2\bar{N}_2 - (2\bar{D}_0 + \bar{D}_2)] + \bar{D}_2\bar{N}_2. \tag{3.50}$$

Due to the algebraic complexity of the problem, we can only give partial results on the linear stability of the solution. In the limit $\mathcal{L} \rightarrow 1$, we find among the roots of the characteristic polynomial

$$\lambda_{\pm} = \frac{1}{2} \left\{ - (1 + 2\bar{I} + \bar{I}_2) \pm \sqrt{(1 + 2\bar{I} + \bar{I}_2)^2 - \kappa\bar{I}(2\bar{D}_0 - \bar{D}_2)} \right\}. \tag{3.51}$$

Since $\kappa \gg 1$, these roots are complex conjugate with negative real part if $\bar{D}_0 > \bar{D}_2/2$. The imaginary part is $\Omega_L = \sqrt{\kappa\bar{I}(2\bar{D}_0 - \bar{D}_2)/4} + O(\kappa^{-1/2})$. Otherwise, they are real and λ_+ is positive. This instability is linked to the competition between modes 1 and 3. If $\bar{D}_2 > 2\bar{D}_0$, either mode 1 or mode 3 is extinguished.

References

- [1] P. Mandel, *Theoretical problems in cavity nonlinear optics* (Cambridge University Press, 1997).
- [2] H. Haken, Phys. Lett. **A53**, 77 (1975).
- [3] C. L. Tang, H. Statz and G. de Mars, J. Appl. Phys. **34**, 2289 (1963).
- [4] J.A. Fleck Jr. and R.E. Kidder, J. Appl. Phys. **35**, 2825 (1964).
- [5] L.A. Ostroskii, Sov. Phys. JETP **21**, 727 (1965).
- [6] L.A. Ostroskii, Sov. Phys. JETP **22**, 1053 (1966).
- [7] N.G. Basov, V.N. Morozov, and A.N. Oraevskii, Sov. Phys. JETP **22**, 622 (1966).
- [8] C. Etrich, P. Mandel, N.B. Abraham, and H. Zeghlache, IEEE J. Quantum Electron. **28**, 811 (1992).
- [9] I.V. Koryukin, P.A. Khandokhin, Ya.I. Khanin, and P. Mandel, Kvantovaya Elektronika (Moscow) **22**, 1081 (1995) [translation: Quantum Electronics **25**, 1045 (1995)].
- [10] P. Mandel, C. Etrich, and K. Otsuka, IEEE J. Quantum Electron. **29**, 836 (1993).
- [11] D. Pieroux and P. Mandel, Quantum Semiclass. Opt. **9**, L17 (1997).
- [12] D. Pieroux, Ph. D. Thesis: *Contribution à la dynamique des lasers multimodes et des lasers contrôlés par rétroaction*, Université Libre de Bruxelles, 1997.
- [13] G. Kozyreff and P. Mandel, Phys. Rev. A **58**, 4946 (1998).
- [14] V.V. Antsiferov, A.V. Ghiner, K.P. Komarov, and K.G. Folin, Kvantovaya Elektronika (Moscow) **2**, 591 (1975) [translation: Quantum Electronics **5**, 332 (1976)]; Ya. I. Khanin, *Principles of Laser Dynamics* (Elsevier, Amsterdam, 1995), p.160.
- [15] P. Mandel, European Physics Journal D **8**, 431 (2000).
- [16] Ya. I. Khanin, *Principles of Laser Dynamics* (Elsevier, Amsterdam, 1995).
- [17] K. Otsuka, P. Mandel, S. Bielawski, D. Derozier, and P. Glorieux, Phys Rev. A **46**, 1692 (1992).
- [18] K. Otsuka, M. Georgiou, and P. Mandel, Jpn. J. Appl. Phys. **31**, L1250 (1992).
- [19] P. Mandel, K. Otsuka, J.-Y. Wang, and D. Pieroux, Phys. Rev. Lett. **76**, 2694 (1996).
- [20] K. Otsuka, P. Mandel, M. Georgiou, and C. Etrich, Jpn. J. Appl. Phys. **32**, L318 (1993).
- [21] K. Wiesenfeld, C. Bracikowski, G. E. James, and R. Roy, Phys. Rev. Lett. **65**, 1749 (1990).

- [22] P. Mandel and J.-Y. Wang, Phys. Rev. Lett. **75**, 1923 (1995).
- [23] D. Pieroux and P. Mandel, Opt. Commun. **107**, 245 (1994).
- [24] D. E. McCumber, Phys. Rev. **141**, 306 (1966).
- [25] I. V. Koryukin and E. Yu. Shirokov, J. Opt. B: Quant. Semiclass. Opt. **1**, 536 (1999).
- [26] A. E. Siegman, *Lasers* (University Sciences Books, 1986), p. 36.
- [27] J. F. Elder and M. J. P. Payne, Opt. Commun. **145**, 329 (1998).
- [28] B.A. Nguyen and P. Mandel, Opt. Comm. **112**, 235 (1994).

Chapter 4

Global coupling with time delay in semiconductor laser arrays

4.1 Introduction

Semiconductor lasers (SCLs), benefitting from the achievements in the industry of electronics, are now easily produced and at low cost. Furthermore, the amount of electromagnetic energy that can be extracted from a semiconductor material by unit volume exceeds by far the performances of other lasing materials, such as solid state or gas lasers. These advantages made semiconductor lasers the optical source of choice in diverse applications from telecommunications to medicine. The need for more optical power has led laser physicists to design semiconductor lasers with a large surface of emission, called “broad area lasers”. These high power sources find applications in laser printers, solid-state laser pump and space communication. However, carrier diffusion and light diffraction produce undesired spatial instabilities in the transverse plane of the laser [1]. As a consequence, light is not emitted uniformly on the transverse plane of the laser. Specifically, filamentary regions with high intensity are separated by other regions where the intensity is almost zero. This phenomenon is called filamentation [2]. When it occurs, the optical gain of the semiconductor material is not optimally used and the output beam characteristics are poor. To overcome this problem, it was proposed to divide the large, broad area laser into many lasing units that are too small for filamentation. Linear arrays of edge emitting SCL producing tens to hundred of watts of cw power are now commercially available but typically with 1-THz linewidths. With the advent of Vertical Surface Emitting SCL, two-dimensional laser arrays also become possible.

A key issue relative to these devices is to lock the phases of the electromagnetic fields emitted by each lasing element. In this way, the linewidth of the total output is reduced because all lasers acquire the same frequency. On the other hand, it is advantageous to lock the emitted fields in-phase. By interference in the far field, this leads to a concentration of almost all the output power in a single narrow lobe (Figure 4.1). In order to achieve such a synchronization, the lasers should be coupled to each other. In this respect, it was soon realized [3] that a coupling between nearest-neighbor elements induces anti-phase synchronization more easily than in-phase synchronization. Anti-phase synchronization means that each laser is dephased by π from the adjacent elements. As illustrated in Fig. 4.1, this produces a double-lobed far field pattern. In addition, for a broad range of coupling strength, the nearest-neighbor coupling leads to a chaotic behavior of the array [4]. On the other hand, it was shown [5]

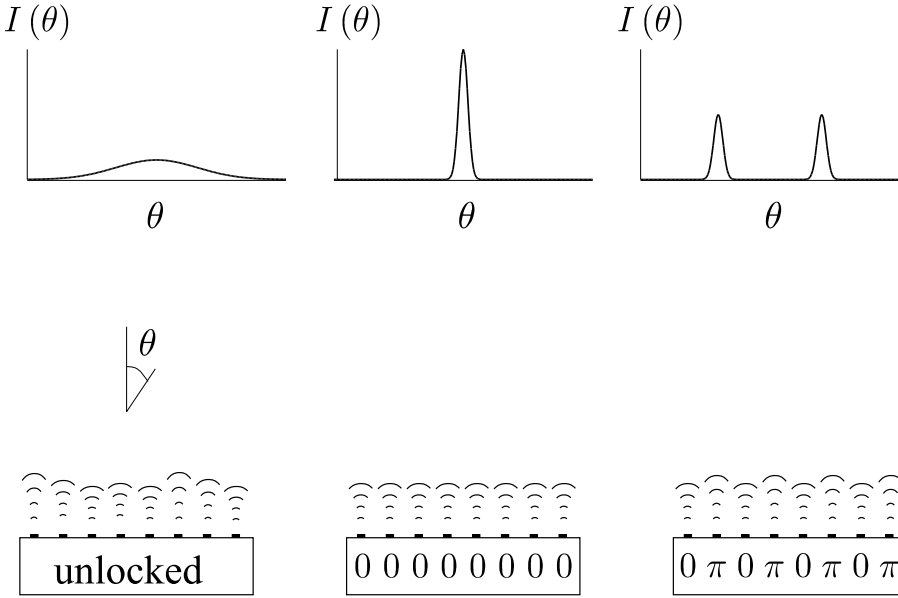


Figure 4.1: Far field pattern of the intensity emitted by a laser array if the lasers are desynchronized, synchronized in-phase, and synchronized in antiphase.

that if each laser is coupled equally to all other elements in the array, the preferential state of synchronization is the in-phase state. The effect of such a global coupling on a laser array with randomly distributed optical frequencies was also theoretically investigated [6]. This leads us to consider an array of semiconductor lasers that are weakly and globally coupled by the optical feedback of an external mirror, as depicted in Fig. 4.2. A similar scheme was recently used to stabilize the emission of a broad area laser [7]. A different but closely related configuration was also recently implemented with a commercial diode laser array [8]. Due to the finite speed of light, the interaction between lasing elements is delayed. How this delay impacts on the synchronization will be the central question in this chapter. Numerical simulations were done for this system [9] that tend to extend the conclusions of [5] to the case where the coupling is delayed: with the increase of the coupling strength, the lasers lock in-phase. The idea to use optical feedback in order to synchronize a laser array was already exploited in [10]. However, up to now, only strong coupling has been considered, which raises some technical difficulties. The very small transverse size of the SCL's, of the order of a few microns, makes it difficult to efficiently reinject a substantial fraction of the emitted field back into their active region. Usually, the mirror is placed a few millimeters away from the array, typically at the Talbot distance. With such a small external cavity length, the only effect of the delay is to change the phase of the reinjected field. The field amplitudes, on the other hand, can be considered as constant over the short external cavity round-trip time.

The problem of coupled lasers can be cast in a more general context. Multimode lasers [11, 12], arrays of Josephson junctions [13], reaction-diffusion systems [14], neural networks in the brain [15] and rhythmic applause in concert halls [16] are other examples of systems that consist of interacting elementary units. An important class of such systems is that of weakly coupled oscillators: if the coupling does not modify significantly the phase space trajectories, one phase variable suffices to describe each oscillating element. This leads to phase models, including the extensively studied Kuramoto equations [14, 17]. In recent years, it was real-

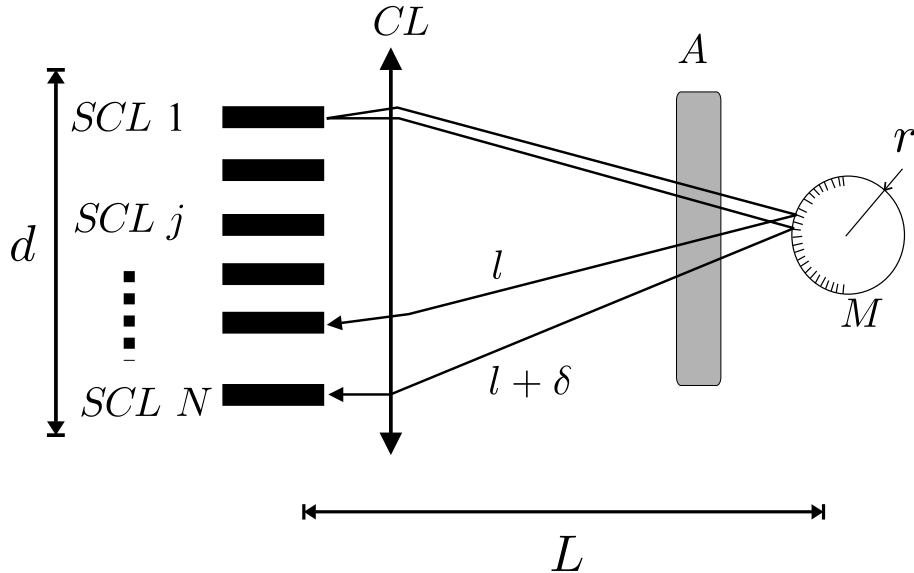


Figure 4.2: Schematic representation of a SCL array with global optical coupling between the lasers. d is the transverse size of the array. The spherical feedback mirror M of radius r is placed at the focus of the converging lens CL and at a distance L from the array. A is an attenuator that controls the strength of the coupling. If the lateral dimension d of the array is small compared to the external cavity length L , the optical length difference δ is approximately bounded by $r(d/2L)^2$. For instance, if $d = 1$ mm, $r = 1$ mm, $L = 10$ cm, $|\delta| \leq 2.5 \cdot 10^{-8}$ m, which is much shorter than one optical wavelength. Therefore, we may assume that $\delta_{jn} = \bar{\delta}$ for all laser indices j and n in Eq. (4.1).

ized that delaying the interactions between elementary cells can have a profound influence on their collective behavior. The principal consequences of time delay documented for phase models concern the occurrence of synchronization [18, 19] and multistability between states of synchronization [20]. However, if the coupling strength is comparable to the attraction to the limit cycle, amplitude quenching or “oscillation death” can also result from the delay [21]. From the general viewpoint of coupled oscillators, the physical system we study in the present chapter mixes the two situations. For very small values of the coupling strength, the electric field emitted by each SCL is essentially described by its optical phase and the system can be modelled by coupled phase equations of the Kuramoto type. However, increasing the coupling strength gives rise to time periodic intensities by way of a Hopf bifurcation. The amplitude of the limit cycle created by this mechanism then strongly depends on the coupling strength. Each element of the array thus becomes a two-frequency oscillator with one frequency in the optical domain and the other frequency corresponding to sustained relaxation oscillations and typically lying in the GHz range for a SCL. To investigate the dynamics of this system, we derive in this chapter a set of phase equations that generalizes the Kuramoto model by the addition of second and third order derivatives of the phase variables.

We show that the constant intensity, or cw, regimes can be either in-phase or out-of-phase. The in-phase steady state can bifurcate towards a time periodic regime where the intensities delivered by each laser oscillate either in phase or in antiphase. The bifurcation to the in-phase time periodic regime does not exist in the absence of a delayed feedback. It is therefore a delay-induced bifurcation. Maximization of the array output is achieved if parameters are selected such that the bifurcation occurs toward the in-phased periodic regime.

The remainder of this chapter is organized as followed. In Sec. 4.2, we describe the model and introduce the evolution equations. In Sec. 4.3 and 4.4, we study the synchronization properties of the SCL array in the cw regime and calculate the self-pulsing thresholds from the cw states. For the in-phase steady state, there are two possible thresholds: a degenerate Hopf bifurcation leading to antiphase periodic laser intensities and a regular Hopf bifurcation leading to in-phase periodic laser intensities. In Sec. 4.5 we present an analytical treatment of the synchronization in the self-pulsing domain in the simplifying limit of a large linewidth enhancement factor. Finally, we conclude.

The results of this chapter were published in part in [22].

4.2 Model

Each laser element in the array, labelled by an index j , is modelled by a complex electric field variable E_j and a material variable Z_j . In the absence of any coupling with the other lasers and if no feedback is present, the field E_j rotates at a natural frequency ω_j , which can differ from one laser to another. The material variable Z_j quantifies the excess carrier density relative to the lasing threshold in the absence of any external coupling. It is rescaled in order to treat dimensionless order one quantities. A single laser subjected to a weak optical feedback is known to be well described by the Lang-Kobayashi equations [23]. Therefore, the mathematical model of our system will be a set of N coupled Lang-Kobayashi equations in dimensionless form:

$$\frac{dE_j}{dt} = i\omega_j E_j + (1 + i\alpha) Z_j E_j + i\frac{\chi}{2} e^{-i\zeta} (E_{j-1} + E_{j+1}) + i\frac{\eta}{N} \sum_{n=1}^N e^{-i\vartheta_{jn}} E_n (t - t_D), \quad (4.1)$$

$$\frac{dZ_j}{dt} = \gamma [P_j - Z_j - (1 + 2Z_j) |E_j|^2]. \quad (4.2)$$

with periodic boundary conditions $E_0 = E_N$, $E_{N+1} = E_1$. In these equations, the time unit is the photon cavity lifetime $\tau_c \equiv 1/\Gamma_c \simeq 2 \times 10^{-12}$ s and $\gamma \equiv \gamma_w/\Gamma_c \simeq 10^{-3}$ is the ratio of the carrier relaxation rate to the cavity damping rate. The parameter α is the linewidth enhancement factor, which accounts phenomenologically of the band structure of the semiconductor material. A typical value of α is 5. P_j is the excess pump parameter of laser j , which is proportional to the injection current above threshold. We suppose that all lasers operate in the same single longitudinal mode of the short cavity. This may require the use of frequency selection techniques [24] or to pump the lasers not too far above lasing threshold. The j^{th} laser has a lasing frequency ω_j/τ_c in the absence of optical feedback and coupling between the lasers. We denote by \bar{P} and $\bar{\omega}$ the average pump and optical frequency over the SCL array. Hereafter we will assume that the deviations $|P_j - \bar{P}|$ and $|\omega_j - \bar{\omega}|$ are small.

The parameter η describes the global coupling strength due to the external mirror. The phase of this coupling is a constant plus the optical dephasing accumulated in the external cavity between lasers n and j . It is denoted by ϑ_{nj} and the mean value over all couples of lasers j and n is $\bar{\vartheta}$. Note that, for symmetry reasons, we do not follow in Eqs. (4.1) and (4.2) the commonly adopted notations in which the feedback term appears without imaginary unit i [25]. This, however, is equivalent to setting $\bar{\vartheta} = \pi/2$, or shifting the position of the external mirror by one eighth of the optical wavelength. Since the exact value of the external cavity length is not known with this precision, we may simply set $\bar{\vartheta}$ equal to zero. The phase

Table 4.1: List of symbols

symbol	signification	value
E_j	electric field emitted by laser j	
Z_j	excess carrier density in laser j relative to transparency in the absence of coupling	
$\omega_j (\bar{\omega})$	natural optical frequency of j (mean frequency)	10^{15} Hz
$P_j (\bar{P})$	pump parameter of laser j (mean pump)	1.5
α	linewidth enhancement factor	5
χ	coupling strength between adjacent lasers due to evanescent fields	$10^{-4} - 10^{-5}$
ζ	phase of the local coupling χ	0
η	global coupling strength due to external mirror	$10^{-4} - 10^{-3}$
$\delta_{nj} (\bar{\delta})$	optical dephasing due to external cavity roundtrip from laser n to j (mean dephasing)	0
Γ_c	internal cavity damping rate	10^{12} s ⁻¹
t_D	external cavity roundtrip time normalized by Γ_c^{-1}	1 – 1000
γ	carrier relaxation rate normalized by Γ_c	10^{-3}
$\Omega_j (\bar{\Omega})$	natural relaxation frequency of laser j normalized by Γ_c (mean frequency)	0.03 (≈ 10 GHz)

dispersion $|\delta_{nj} - \bar{\delta}|$ can be made small if the feedback mirror (with radius $r \ll L$) is placed at the focus of a converging lens and sufficiently far from the SCL array (See Fig. 4.2). Hereafter, the theoretical conclusions will therefore be stated for $\delta_{nj} = 0$. The global coupling is also characterized by an important parameter $t_D = 2L/(c\tau_c)$, which is the external cavity round-trip time normalized by τ_c . The parameters χ and ζ measure, respectively, the strength and the phase of the local coupling that can arise due to the interaction between neighboring lasers via evanescent fields. Note that the phase of the local coupling ζ is usually assumed to be zero [4]. Finally, we will assume that the coupling between the lasers is weak: $\eta, \chi \ll 1$. The signification and value of the symbols is summarized in Table 4.2.

4.3 Synchronization below self-pulsing threshold

4.3.1 In-phase synchronization

In this Section, we discuss the steady states of Eqs. (4.1) and (4.2) and their stability as a function of the strength η and the delay t_D of the global coupling. By steady state, we mean that the intensities are constant, contrary to the field phases, which can still vary. Both cw in-phase and antiphase solutions exist. To determine which of these is effectively chosen by the system, we study their linear stability. Since we are mainly interested in the effect of time delay on the synchronization of globally coupled lasers, we present a detailed stability analysis for the case $\chi = 0$ and only briefly discuss the influence of the local coupling on the stability properties of cw states. Expressions of the stability conditions which are valid for nonzero χ are given in Appendix 4.A. As we mention it in the introduction, the optical feedback can destabilize the SCL array from its cw operation. However, before η exceeds the self-pulsing threshold, the SCL's deliver a constant intensity. Below this threshold the stability of the steady state justifies that Z_j and the modulus of the fields $|E_j|$ can be adiabatically eliminated in (4.1) and (4.2). In the limit $|P_j/\bar{P} - 1| = |\delta P_j| \ll 1$, this yields the following set of N

coupled equations for the field phases $\phi_j(t)$:

$$\boxed{\frac{d\phi_j}{dt} = \omega_j - \frac{\eta\sqrt{1+\alpha^2}}{N} \sum_{n=1}^N \sin [\vartheta_{jn} + \phi_j - \phi_n(t-t_D) - \cot^{-1}\alpha] - \frac{\chi\sqrt{1+\alpha^2}}{2} \sum_{q=1,-1} \sin (\phi_j - \phi_{j+q} + \zeta - \cot^{-1}\alpha),} \quad (4.3)$$

with the boundary conditions $\phi_0 = \phi_N$, $\phi_{N+1} = \phi_1$. Note that the effective coupling strength in (4.3) is proportional to $\sqrt{1+\alpha^2}$ and therefore increases with the linewidth enhancement factor α . If local interactions are negligible, $\chi \ll \eta$, and if $|\vartheta_{jn}| \ll 1$, Eqs. (4.3) reduce to the Kuramoto equations with a time delay [18, 19]. In addition, let all the lasers be identical, so that $\omega_j = \bar{\omega}$. The in-phase solutions of (4.3) are given by $\phi_j = \phi_k = \omega t$ with the common frequency ω obeying the transcendental equation

$$\omega = \bar{\omega} - \sqrt{1+\alpha^2}\eta \sin(\omega t_D - \cot^{-1}\alpha). \quad (4.4)$$

This equation can have multiple solutions. They correspond to the external cavity modes (ECM) of the single laser [25] which grow in number with increasing ηt_D . The linear stability analysis of the in-phase cw (See Appendix 4.A) state defines triangular domains in the $(\bar{\omega}t_D, \eta)$ parameter space where this solution is unstable:

$$\frac{\pi}{2} + \eta t_D \sqrt{1+\alpha^2} \leq \bar{\omega}t_D - \cot^{-1}\alpha - 2n\pi \leq \frac{3\pi}{2} - \eta t_D \sqrt{1+\alpha^2}, \quad (4.5)$$

where n is an arbitrary integer. These triangles of instability are shown in Figures 4.3 and 4.4 for two values of the delay t_D . These inequalities are consistent with results derived in [18] and obtained in the limit $N \rightarrow \infty$. In Eq. (4.5) the time delay appears in two well separated time scales: $\bar{\omega}t_D$ and ηt_D . Since $\eta \ll 1 \ll \bar{\omega}$, the variation of the external cavity length L over one optical wavelength leads to a variation of 4π for $\bar{\omega}t_D$ but leaves ηt_D almost constant. Therefore we can consider $\bar{\omega}t_D$ and ηt_D as independent parameters of the problem. Inside the domain defined by (4.5), in-phase synchronization is lost in favor of antiphase cw regimes. The size of these instability domains is inversely proportional to ηt_D . Therefore, to increase the time delay favors in-phase cw operation. In Sec. 4.4, we shall define selfpulsing thresholds η_{H1}, η_{H2} to periodic intensities. If t_D is sufficiently large and if $\pi(2t_D\sqrt{1+\alpha^2})^{-1} < \eta < \eta_{H1,2}$, stable cw in-phase operation exists for all values of $\bar{\omega}t_D$. This is due to the overlap of stability domains of cw in-phase solutions corresponding to different ECM.

4.3.2 Antiphase synchronization

The antiphase cw solutions are defined by

$$\phi_j = \bar{\omega}t + 2jM\pi/N, \quad (4.6)$$

where the integer M determines the type of antiphase state. In the absence of local coupling, the linear stability analysis indicates that the antiphase state (4.6) is neutrally stable with $N-1$ zero eigenvalues. This neutral stability is related to the existence of a $(N-1)$ -dimensional

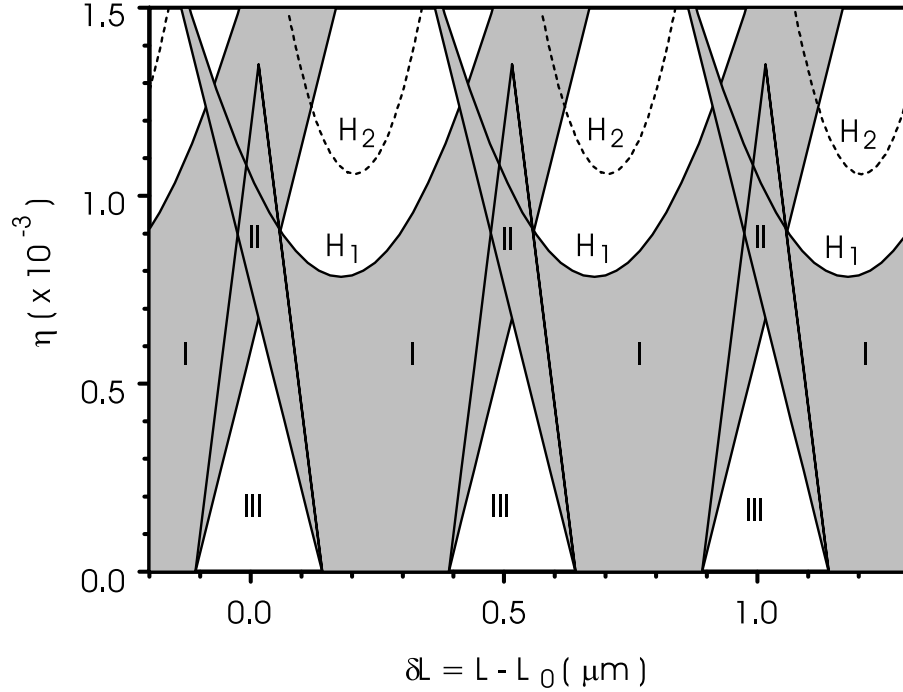


Figure 4.3: Stability boundaries of cw solutions. The parameters values are the same as in Fig. 2. $L = 13.7 \text{ cm} + \delta L$. In-phase states corresponding to different ECM are stable in the grey areas (I and II). In the regions II stable antiphase and in-phase states coexist. In the white triangular regions III only antiphase states are stable. Curves $H_{1,2}$ indicate the locations of Hopf bifurcations. The antiphase Hopf bifurcation precedes the in-phase Hopf bifurcation.

invariant manifold in the phase space of Eq. (4.3). It is the manifold spanned by the antiphase solutions that verify the relation $\sum_j \exp(i\phi_j) = 0$ [26, 27, 28]. We find the following neutral stability domains of the antiphase cw solutions (4.6)

$$\frac{\pi}{2} + \frac{\eta t_D}{2} \sqrt{1 + a^2} \leq \bar{\omega} t_D - \cot^{-1} \alpha - 2n\pi \leq \frac{3\pi}{2} - \frac{\eta t_D}{2} \sqrt{1 + a^2}. \quad (4.7)$$

Let us now relax the assumption $\omega_j = \bar{\omega}$. Then, in the large N limit, assuming a Lorentzian distribution for the natural frequencies, $g(\omega') = (\Gamma/\pi) [\Gamma^2 + (\omega' - \bar{\omega})^2]^{-1}$, the stability condition for the desynchronized state becomes [18, 19]

$$\eta < \eta_c \equiv \frac{2\Gamma}{\sqrt{1 + a^2} \cos(\bar{\omega} t_D - \cot^{-1} \alpha)}, \quad (4.8)$$

where ω verifies the equation (4.39) with $\eta = \eta_c$ and $\chi = 0$. Note that, as $\Gamma \rightarrow 0$, the stability boundary defined by (4.8) transforms into (4.38) with $\chi = 0$.

Finally, we note that the phase equations (4.3) are valid in the limit $\eta, \chi, |\delta P_j| \ll 1$ and below the self-pulsing threshold. Under these assumptions, the stability conditions obtained in this Section agree with the linear stability analysis of the full equations (4.1) and (4.2).

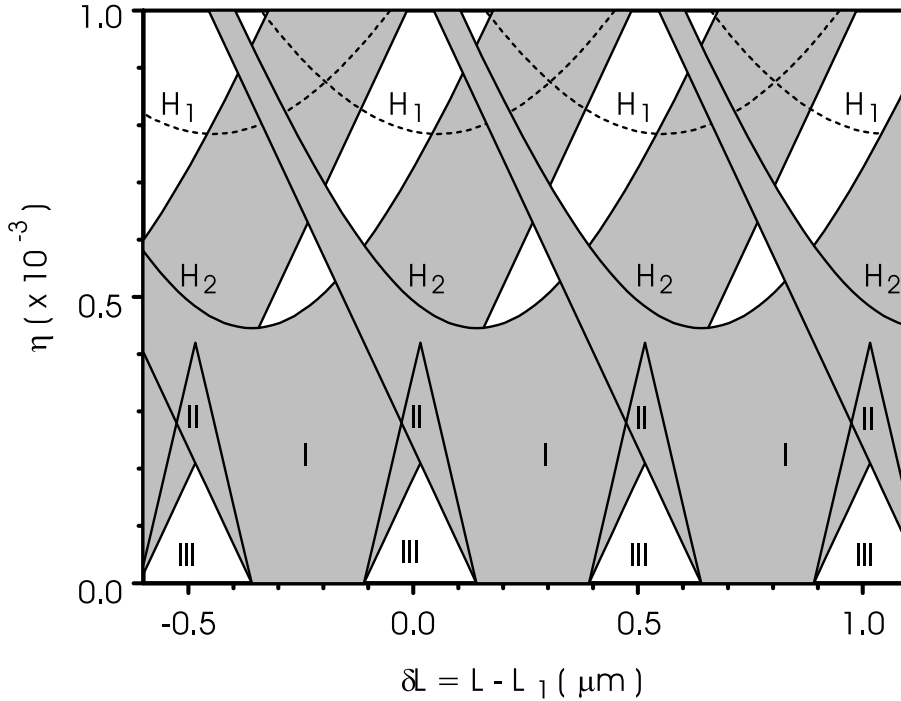


Figure 4.4: Stability boundaries of cw solutions. The parameters values are the same as in Fig. 2. $L = 44 \text{ cm} + \delta L$. In-phase states corresponding to different ECM are stable in the grey areas (I and II). In the regions II stable antiphase and in-phase states coexist. In the white triangular regions III only antiphase states are stable. Curves $H_{1,2}$ indicate the locations of Hopf bifurcations. The in-phase Hopf bifurcation precedes the antiphase one.

4.4 Self-pulsing instabilities

In order to describe Hopf bifurcations of the in-phase cw state leading to solutions with self-pulsing laser intensities, we return to the original set of coupled Lang-Kobayashi equations (4.1) and (4.2). We confine our treatment to the case of identical lasers by setting $\omega_j = \bar{\omega}$ and $P_j = \bar{P}$. The complete in-phase cw solution of Eqs. (4.1) and (4.2) is then

$$E_j(t) = \left(\frac{\bar{P} + \eta \sin \omega t_D + \chi \sin \zeta}{1 - 2\eta \sin \omega t_D - 2\chi \sin \zeta} \right)^{1/2} e^{i\omega t}, \quad (4.9)$$

$$Z_j(t) = -\eta \sin \omega t_D - \chi \sin \zeta. \quad (4.10)$$

where ω is the solution of (4.4). Besides the desynchronization boundaries (4.5), a linear stability analysis of (4.9) and (4.10) reveals the existence of two different types of Hopf bifurcations leading to self-pulsing solutions. The bifurcations of the first type are associated with perturbations transverse to the synchronization manifold $\{E_1 = \dots = E_N, Z_1 = \dots = Z_N\}$. In the limit of a weak global coupling $\eta \ll 1$ and neglecting local coupling χ , these bifurcations merge into a single $(N - 1)$ -fold degenerate bifurcation defined by

$$\eta = \eta_{H1} \equiv \frac{\gamma(1 + 2\bar{P})}{\sqrt{1 + \alpha^2} \cos(\omega t_D + \cot^{-1} \alpha)}. \quad (4.11)$$

The associated relaxation oscillation frequency is $(2\gamma\bar{P})^{1/2}$. Such a degeneracy is known to produce multiple branches of antiphase self-pulsing solutions [12]. The antiphase character of the emerging sustained relaxation oscillations partially destroys the in-phase synchronization of the cw state. This can be seen on the bifurcation diagram in Fig. 4.5. The branch A-P represents minima and maxima of the total field amplitude as a function of η corresponding to antiphase relaxations in the intensities. With the increase of η , the average total field decreases. The solutions describing these intensity oscillations will be constructed in the next section.

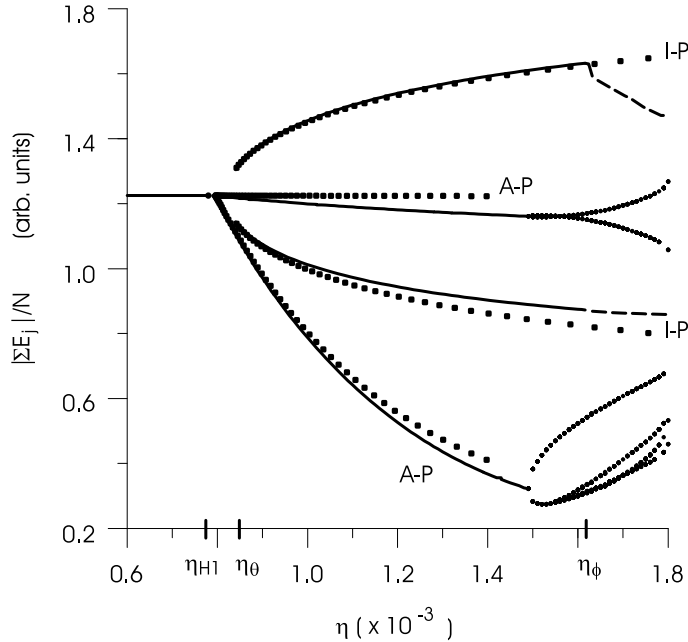


Figure 4.5: Branches of self-pulsing solutions bifurcating from the in-phase cw state obtained by simulating numerically Eqs. (4.1) and (4.2) with $N = 5$, $\text{mod}(\bar{\omega}t_D, 2\pi) = 0.14$ and $t_D = 91.7$, which corresponds to $\varphi \simeq \bar{\Omega}t_D = 5.02$ and $\tau_D = 0.18$. Minima and maxima of the total field are plotted as functions of η . Other parameters are the same as in Fig 2. The secondary bifurcation η_θ (η_ϕ) corresponds to K_θ (K_ϕ) discussed in Sec. 4.5.1. Dotted lines are the analytical approximations for the self-pulsing solutions obtained using (4.24)-(4.26) and (4.30)-(4.31).

Another Hopf bifurcation, which is always nondegenerate, is located at

$$\eta = \eta_{H2} \equiv \frac{\eta_{H1}}{1 - \cos \varphi}, \quad \varphi \equiv \Omega_{H2}(t_D, \bar{P}, \gamma) \times t_D. \quad (4.12)$$

Note that the bifurcation condition (4.12) is independent of χ and is identical to that of a solitary laser with a feedback strength η instead of η/N in (4.1). The frequency Ω_{H2} characterizing the oscillations at $\eta = \eta_{H2}$ satisfies the transcendental equation

$$\Omega_{H2} = (2\gamma\bar{P})^{1/2} + \gamma(\bar{P} + 1/2) \cot\left(\frac{\Omega_{H2}t_D}{2}\right). \quad (4.13)$$

This equation has an infinity of solutions, each producing a different η_{H2} through the discrete values of φ in Eq. (4.12). The periodic solution that bifurcates at $\eta = \eta_{H2}$ lies within the synchronization manifold. It is therefore characterized by in-phase synchronization not

only in the oscillations at the optical frequency ω , but also in the relaxation oscillations at frequency Ω_{H2} . The resulting average total field amplitude is therefore maximum, as illustrated by the branch I-P in Fig. 4.5.

Which of the two Hopf bifurcations, $\eta = \eta_{H1}$ or $\eta = \eta_{H2}$, takes place first and, hence, destabilizes the cw solution depends on the order of magnitude of the time delay t_D . We discuss three different situations: small, moderate, and large delays.

1. If $t_D \ll \gamma^{-1/2}$, then $\varphi \ll 1$ and the cw solution (4.9) and (4.10) can only be destabilized through the Hopf bifurcation at $\eta = \eta_{H1}$. In this limit, however, the phase dispersions ϑ_{nj} may become non negligible, which makes the validity of formula (4.11) questionable.
2. If $t_D \sim \gamma^{-1/2}$, i.e., the time delay is comparable to the relaxation oscillations period. The value of φ corresponding to the lowest bifurcation threshold η_{H2} is well approximated by $(2\gamma\bar{P})^{1/2} t_D$. Then the relative position of η_{H1} and η_{H2} can be controlled through φ by changing the external cavity length on the centimeter scale.
3. Finally, if $t_D \gtrsim \pi\gamma^{-1}(2\bar{P} + 1)^{-1}$ there exists at least one solution Ω_{H2} of (4.13) such that $\eta_{H2} < \eta_{H1}$. Therefore, it is always the in-phase Hopf bifurcation (4.12) that destabilizes the in-phase cw solution. Moreover, our numerical simulations indicate that for large delays the in-phase synchronized self-pulsing solution emerging at $\eta = \eta_{H2}$ is stable in a wide domain above the desynchronization threshold given by $\eta = \eta_{H1}$. In this sense, the antiphase instability is bypassed and in-phase synchronization is preserved by the in-phase Hopf bifurcation at $\eta = \eta_{H2}$.

Figure 4.6 illustrates the order of appearance of the Hopf bifurcations $\eta = \eta_{H1}$ and $\eta = \eta_{H2}$ as a function of the time delay. From (4.11) and (4.12), η_{H1} and η_{H2} have minima $\eta_{H1} = \gamma(1 + 2\bar{P})/\sqrt{1 + \alpha^2}$ and $\eta_{H2} = \eta_{H1}/(1 - \cos\varphi)$ at $\cos(\omega t_D + \cot^{-1}\alpha) = 1$. These minima are shown as functions of the external cavity length L . One can see that for $L \lesssim 20$ cm the order of appearance of the two Hopf bifurcations, $\eta = \eta_{H1}$ and $\eta = \eta_{H2}$, can be controlled through L . For larger L , the in-phase Hopf bifurcation always precedes the antiphase Hopf bifurcation.

The linear stability analysis of the cw states is summarized in Figs. 4.3 and 4.4 for values of the external cavity length in the vicinity of $L \approx 13.7$ cm and $L \approx 44$ cm, respectively. In these figures L varies on the scale of the optical wavelength which we fix at $\lambda = 1 \mu\text{m}$. The grey areas labelled I and II are the stability domains of different cw in-phase solutions, each corresponding to a certain ECM. In Fig. 4.3, it is the Hopf bifurcation to antiphase self-pulsing solutions at $\eta = \eta_{H1} < \eta_{H2}$, which takes place first and destabilizes the in-phase cw state. In Fig. 4.4, corresponding to a larger value of feedback delay, the first Hopf bifurcation leading to inphase self-pulsing regime takes place at $\eta = \eta_{H2} < \eta_{H1}$.

Having determined the critical coupling strengths η_{H1} and η_{H2} , we can complete the conditions to achieve synchronization in the cw operation:

$$\boxed{\eta_c < \eta < \eta_{H1}, \eta_{H2}}, \quad (4.14)$$

where η_c is defined in (4.8). Qualitatively, this imposes that the dispersion of the natural frequencies Γ be smaller than the relaxation rate of the carrier density γ .

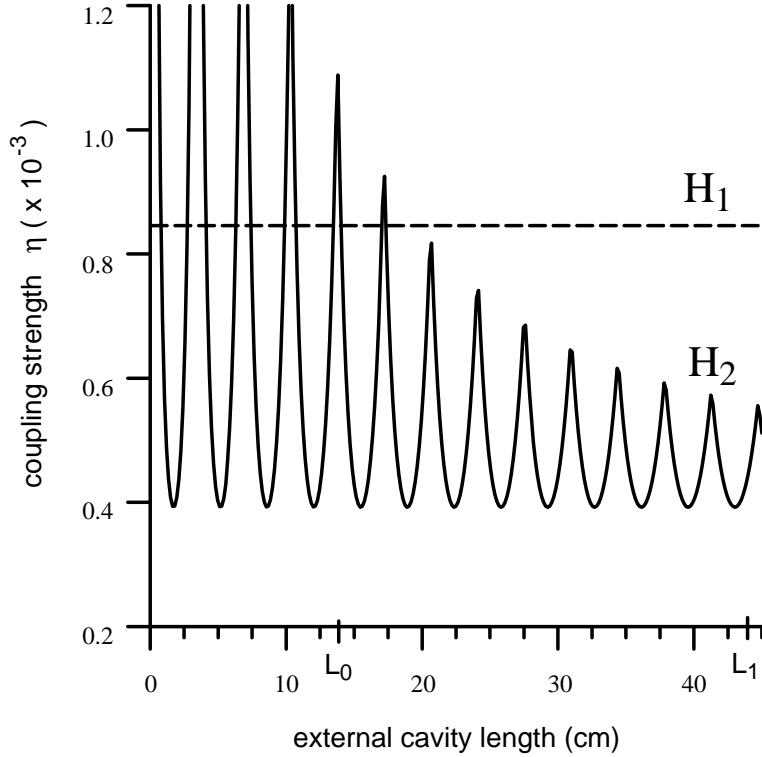


Figure 4.6: Relative positions of the two Hopf bifurcations. $\chi = 0$, $\alpha = 5$, $\bar{P} = 1.5$, $\gamma = 10^{-3}$. The dashed line H_1 shows the minimal coupling strength necessary to reach the degenerate Hopf bifurcation $\eta = \eta_{H1}$. It corresponds to the minima of the curves H_1 shown in Figs 4.3 and 4.4. The solid line H_2 represents the minimal coupling strength corresponding to the in-phase Hopf bifurcation $\eta = \eta_{H2}$, calculated using Eq. (4.12).

Finally we conclude that according to the linear stability analysis, a large time delay favors in-phase synchronization because it reduces the size of the instability domains (4.5) of the cw in-phase state and favors the in-phase Hopf bifurcation at $\eta = \eta_{H2}$ against the antiphase bifurcation at $\eta = \eta_{H1}$.

4.5 Self-pulsing solutions

We now construct the time periodic solutions that bifurcate from the in-phase cw solution (4.9) and (4.10). For the sake of mathematical convenience, we assume that $\alpha \gg 1$. Using this approximation, it is possible to describe analytically not only small amplitude self-pulsing solutions of (4.1) and (4.2) near Hopf bifurcation thresholds but finite amplitude periodic intensity solutions as well. Although in practice $\alpha \approx 5$, the agreement with numerical results is quite remarkable. Working in the limit $\gamma, \eta, \chi, \alpha^{-1} \ll 1$, we seek a solution of Eqs. (4.1) and (4.2) of the following form

$$E_j(t) = \sqrt{P_j} \left(1 + \frac{y_j}{\alpha} \right) \exp(i\Phi_j), \quad (4.15)$$

$$Z_j(t) = \Omega_j \frac{x_j}{\alpha}, \quad \Omega_j = \sqrt{2\gamma P_j}. \quad (4.16)$$

Following the procedure described in Appendix 4.B, we obtain the following set of N coupled third order phase equations

$$\begin{aligned} \frac{1}{\Omega_j^2} \left[\frac{d^3 \Phi_j}{dt^3} + \gamma (2P_j + 1) \frac{d^2 \Phi_j}{dt^2} \right] + \frac{d \Phi_j}{dt} &= \omega_j - \frac{\alpha \eta}{N} \sum_{n=1}^N \sin [\vartheta_{jn} + \Phi_j - \Phi_n(t - t_D)] \\ &\quad - \frac{\alpha \chi}{2} \sum_{q=-1,1} \sin (\zeta + \Phi_j - \Phi_{j+q}). \end{aligned} \quad (4.17)$$

These equations generalize the phase equations (4.3) by the presence of higher order derivatives of Φ_j . We note that the equations recently derived in [29] for a multimode single SCL with external feedback have a structure that is similar to (4.17). One can also note an analogy between (4.17) and the extended Kuramoto model, studied in [30, 31], in which a second derivative of the phase variable was included in order to take into account “inertial” effects. The authors of Ref. [30] found, in the limit $N \rightarrow \infty$, that inertia embarrasses the in-phase synchronization. In our case inertial terms proportional to higher order derivatives in (4.17) are responsible for the appearance of self-pulsing instabilities at $\eta = \eta_{H1}$ and $\eta = \eta_{H2}$. As already mentioned, the first of these two instabilities leads to the solutions with partially broken in-phase synchrony.

We derive amplitude equations by following the two-time scale perturbation approach proposed in [32]. To this end, we introduce the two time variables s and τ and their delays by

$$(s, s_D) = \bar{\Omega} \times (t, t_D), \quad (\tau, \tau_D) = \gamma (\bar{P} + 1/2) \times (t, t_D), \quad (4.18)$$

where $\bar{\Omega} = \sqrt{2\gamma\bar{P}}$ is the average natural relaxation frequency over the laser array. Coupling parameters and frequencies are rescaled as

$$(K, X, \delta\omega_j, \delta\Omega_j) = \frac{2}{\gamma(2\bar{P} + 1)} \times (\alpha\eta, \alpha\chi, \omega_j - \bar{\omega}, \Omega_j - \bar{\Omega}).$$

In the leading order approximation, one obtains

$$x_j = -\text{Im}[z_j(\tau) e^{is}], \quad y_j = \text{Re}[z_j(\tau) e^{is}], \quad \Phi_j = \bar{\omega}t + \phi_j(\tau) + \text{Re}[z_j(\tau) e^{is}]. \quad (4.19)$$

This solution is represented in Fig. 4.7 for two laser elements. The motion of each electric phasor contains a monotonic part given by $\bar{\omega}t + \phi_j(\tau)$ on which an oscillatory component $z_j(\tau) e^{is}$ is superimposed. The former is related to the optical motion whereas the latter describes the relaxation oscillations. The question of synchronization concerns the two motions simultaneously. To this end, we derive (see Appendix 4.B) the slow time evolution equations for $\phi_j(\tau)$ and $z_j(\tau)$:

$$\begin{aligned} \frac{d\phi_j}{d\tau} &= \delta\omega_j - \frac{K}{N} \sum_{n=1}^N \sin(\phi_{jn}) J_0(|z_{jn}|) - \frac{X}{2} \sum_{q=j-1,j+1} \sin(\xi_{jq}) J_0(|w_{jq}|), \\ \frac{dz_j}{d\tau} &= (-1 + i\delta\Omega_j) z_j + \frac{K}{N} \sum_{n=1}^N \cos(\phi_{jn}) z_{jn} \frac{J_1(|z_{jn}|)}{|z_{jn}|} + \frac{X}{2} \sum_{q=j-1,j+1} \cos(\xi_{jq}) w_{jq} \frac{J_1(|w_{jq}|)}{|w_{jq}|}, \end{aligned} \quad (4.20)$$

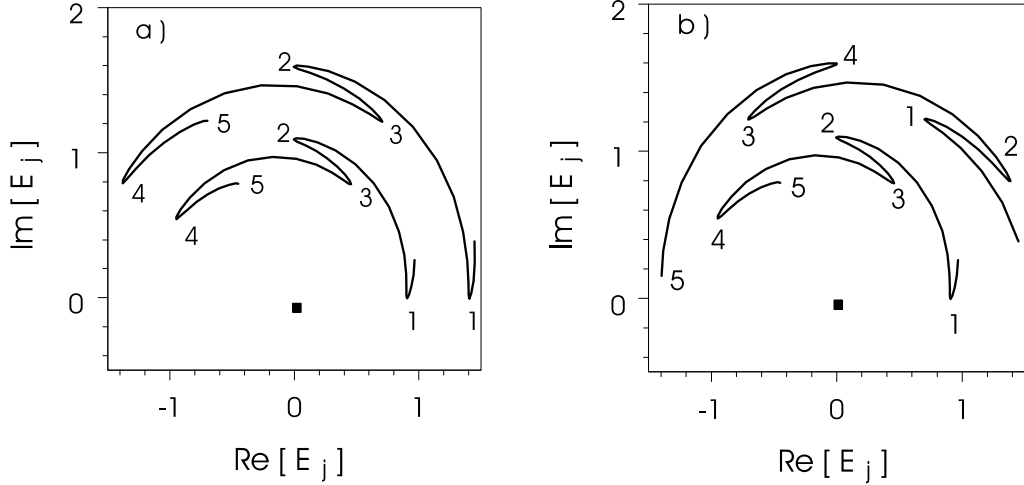


Figure 4.7: Periodic solutions of (4.1) and (4.2). The real and imaginary parts of the electric field is plotted for two lasers in a frame rotating at the velocity $\bar{\omega}t$. The two traces are radially shifted for clarity. The numbers are temporal reference points. (a) Both the optical and relaxation oscillations are in-phased: $\phi_1 = \phi_2$, $z_1 = z_2$. (b) Optical oscillations are in-phase, relaxation oscillations are antiphased: $\phi_1 = \phi_2$, $z_1 = -z_2$. Note that the two traces can represent clusters of lasers as well.

In these equations, $J_\nu(x)$ are Bessel functions of the first kind and

$$\phi_{jn} = \bar{\omega}t_D + \vartheta_{jn} + \phi_j - \phi_n(\tau - \tau_D), \quad (4.21)$$

$$z_{jn} = z_j - z_n(\tau - \tau_D) \exp(-is_D), \quad (4.22)$$

$$\xi_{jq} = \zeta + \phi_j - \phi_q, \quad w_{jq} = z_j - z_q. \quad (4.23)$$

We use the amplitude Eqs. (4.20) in order to describe analytically periodic self-pulsing regimes in the array. Specifically, the steady state $z_1 = \dots = z_N = 0$ of Eqs. (4.20) corresponds to the cw solutions of the original Lang-Kobayashi equations, whereas the states with time independent $|z_j| \neq 0$ correspond to periodic self-pulsing solutions of (4.1) and (4.2).

Although, for the sake of generality, local coupling and dispersion in natural frequencies are included in (4.20), below we focus on the synchronization of globally coupled oscillators with identical parameters in the absence of local coupling: $X, \delta\Omega_j, \delta\omega_j, \vartheta_{jn} = 0$.

4.5.1 In-phase periodic solution

The in-phase periodic solution of (4.1) and (4.2) that bifurcates at $\eta = \eta_{H2}$ is obtained by substituting $\phi_j = \phi_n = \Delta\omega\tau$ and $z_j(\tau) = z_n(\tau) = \rho \exp(i\Delta\Omega\tau)$ with a time independent ρ in (4.20). This solution is illustrated in Fig. 4.7 for two lasers. The amplitude ρ of the oscillations is then related to the rescaled coupling parameter K by the implicit relation

$$K^{-1} = \frac{\tilde{\rho}J_1(\tilde{\rho})}{2\rho^2} \cos\psi, \quad \tilde{\rho} = 2\rho \sin(\varphi/2) \quad (4.24)$$

$$\psi = \bar{\omega}t_D + \Delta\omega\tau_D, \quad \varphi = \bar{\Omega}t_D + \Delta\Omega\tau_D, \quad (4.25)$$

where the frequency shifts $\Delta\omega$ and $\Delta\Omega$ obey the transcendental equations

$$\Delta\omega = -2\frac{\rho^2 J_0(\tilde{\rho})}{\tilde{\rho}J_1(\tilde{\rho})} \tan\psi, \quad \Delta\Omega = \cot\left(\frac{\varphi}{2}\right). \quad (4.26)$$

Eq. (4.26) for the correction to the relaxation oscillation frequency $\Delta\Omega$ is in fact equivalent to Eq. (4.13). The value of φ can be controlled by varying the external cavity length on the cm scale. The stability of the solution (4.24)-(4.26) can be determined by linearizing Eqs. (4.20) and applying discrete Fourier transformation of variables as in (4.33). This yields stability conditions for perturbations transverse to the synchronization manifold.

If $\eta_{H2} < \eta_{H1}$, that is if $\cos \varphi < 0$, the in-phase periodic solution is stable in the vicinity of the self-pulsing threshold. However, it can be destabilized by a secondary bifurcation K_ϕ . The condition $K = K_\phi$ defines a $(N - 1)$ -fold degenerate steady state bifurcation of Eqs. (4.20) which corresponds to a secondary bifurcation of the in-phase periodic solutions of Eqs. (4.1) and (4.2). This bifurcation leads to a gradual desynchronization of the optical phases ϕ_j . To demonstrate this point, we perturb the in-phase solution (4.24)-(4.26) as $\phi_j = \Delta\omega\tau + \delta\phi_j$ and $z_j = \rho \exp(i\Delta\Omega\tau) + \delta z_j$. In the particular case $\cos \psi = 1$, the linearized equations for $\delta\phi_j$ decouple from those for δz_j

$$\frac{d\delta\phi_j}{d\tau} = -KJ_0(\tilde{\rho}) \sum_n \delta\phi_j - \delta\phi_n(\tau - \tau_D). \quad (4.27)$$

According to (4.27) the secondary instability $K = K_\phi$ takes place when the quantity $J_0(\tilde{\rho})$ changes from positive to negative with increasing ρ .

If $\eta_{H2} > \eta_{H1}$, the cw regime is already unstable at the Hopf bifurcation $K = K_{H2}$ and the in-phase periodic solution emerging from this point is, therefore, also unstable. However, the laser array can be stabilized in the in-phase state through a $(N - 1)$ -fold degenerate Hopf bifurcation of Eqs. (4.20) at $K = K_\theta$. It corresponds to a secondary antiphase Hopf bifurcation of the in-phase self-pulsing solution in the original laser equations. Increasing further K , the laser array again loses its in-phase synchronization at $K = K_\phi > K_\theta$. This situation is illustrated by the bifurcation diagram shown in Fig. 4.5 together with Fig. 4.8 [35]. In this figure,

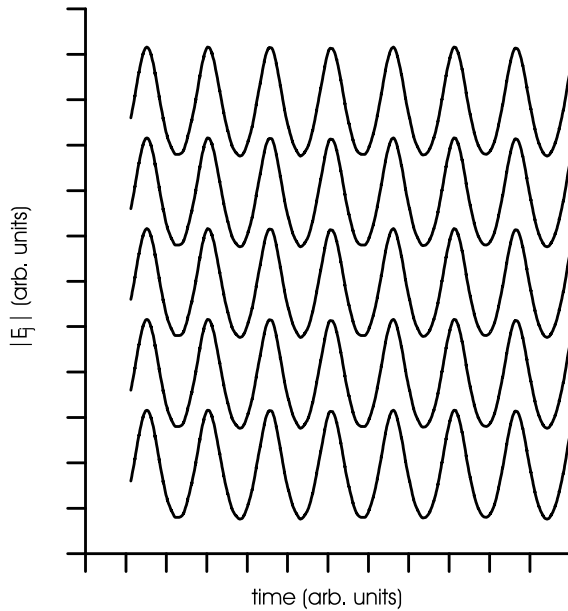


Figure 4.8: Intensities for the in-phase self-pulsing branch I-P of Fig. 4.5. $\eta = 1.12 \cdot 10^{-3}$.

the branches of stable self-pulsing solutions bifurcating from the in-phase cw state are shown

as functions of the coupling strength. It is seen that in-phase and antiphase self-pulsing regimes can coexist in a broad range of coupling strengths. The bifurcation thresholds $K = K_\theta$ and $K = K_\phi$ are shown in Fig. 4.9 as functions of $\omega \tau_D - 2 n \pi$.

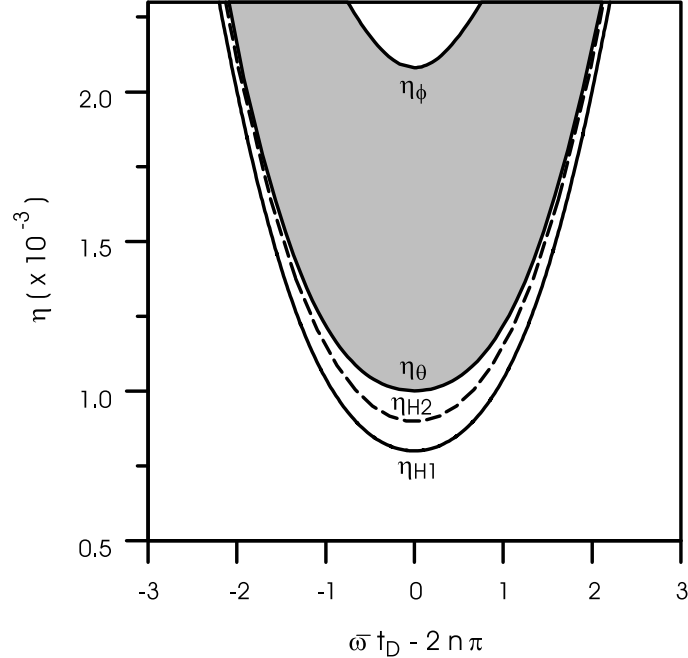


Figure 4.9: Bifurcation loci of the in-phase self-pulsing solution labelled I-P in Fig. 4a. The curve η_{H2} corresponds to the Hopf bifurcation from the already unstable cw in-phase solution. The in-phase self-pulsing solution exists above this curve and is stable in the grey region delimited by the curves $\eta_\theta \equiv \gamma(\bar{P} + 1/2)\alpha^{-1}K_\theta$ and $\eta_\phi \equiv \gamma(\bar{P} + 1/2)\alpha^{-1}K_\phi$.

The bifurcation diagram shown in Fig. 4.10. corresponds to a large value of the delay, $\tau_D = 1.83$, for which the in-phase Hopf bifurcation always precedes the antiphase Hopf bifurcation. As shown in the figure, the stable in-phase self-pulsing solution emerging at $\eta = \eta_{H2}$ undergoes a secondary Hopf bifurcation to in-phase synchronized solution with quasiperiodic laser intensities. Since this secondary bifurcation takes place before the desynchronizing bifurcation at $K = K_\phi$, in-phase synchronization is preserved in the quasiperiodic self-pulsing regime. This eventually leads to an in-phase synchronized chaotic regime with increasing η .

4.5.2 Antiphase periodic solutions

Let us now study the solutions that emerge from the Hopf point $\eta = \eta_{H1}$. From the linear stability analysis, we know that the antiphase self-pulsing solutions can destabilize the cw in-phase state only if τ_D is sufficiently small. Otherwise, $\eta_{H2} < \eta_{H1}$ and the in-phase periodic solution emerges first. Let us assume that $\tau_D \ll 1$ and, therefore, neglect the delay τ_D in (4.21). An example of periodic solution where the optical phases ϕ_j are locked in-phase but the relaxation oscillations are in antiphase is given in Fig. 4.7 for two lasers. Substituting $\phi_j = \Delta\omega\tau$ and $z_j = \rho \exp(i\Delta\Omega\tau + 2ijk\pi/N)$ in Eqs. (4.20), we get the following relation between the amplitude ρ of the antiphase selfpulsing solution with the discrete wave number

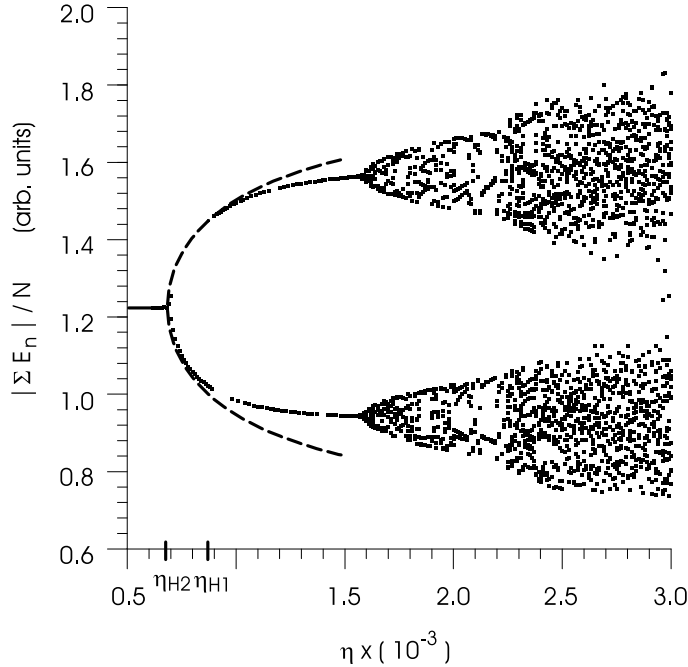


Figure 4.10: Numerically calculated bifurcation diagram for Eqs. (4.1) and (4.2) with $N = 4$, $\text{mod}(\bar{\omega}t_D, 2\pi) = 0.14$ and $t_D = 917$, which corresponds to $\bar{\Omega}t_D = 50.2$ and $\tau_D = 1.83$. Other parameters are the same as in Fig 2. The cw in-phase state undergoes the Hopf bifurcation leading to stable in-phase self-pulsing solution. With the increase of the coupling strength η this solution bifurcates into a quasiperiodic in-phase synchronized regime via a secondary Hopf bifurcation. The latter regime bifurcates to a chaotic in-phase synchronized regime as η is further increased. Broken lines show analytical results obtained using Eqs. (4.24)-(4.26).

k and the rescaled coupling parameter K

$$K^{-1} = \frac{\cos(\omega t_D)}{N} \sum_{n=1}^N \frac{\rho_{n,k} J_1(\rho_{n,k})}{2\rho^2}, \quad (4.28)$$

where

$$\rho_{n,k} = 2\rho \sin\left(\frac{\bar{\Omega}t_D}{2} - \frac{nk\pi}{N}\right).$$

In the bifurcation equation (4.28), k can take any integer value between 1 and $N - 1$, each corresponding to a different antiphase periodic solution. Letting $\rho \rightarrow 0$ in (4.28), we obtain $K \rightarrow K_{H1} = 2/\cos(\omega t_D)$. All these solutions have the same scaling near $K = K_{H1}$, namely $\rho = \sqrt{8\Delta K/3} + O(\Delta K^{3/2})$ with $\Delta K = K/K_{H1} - 1$, except the solution corresponding to $k = N/2$ with N even, which scales as

$$\rho = \sqrt{\frac{8\Delta K}{3 + \cos(2\bar{\Omega}t_D)}} + O(\Delta K^{3/2}). \quad (4.29)$$

The self-pulsing antiphase solution with the wave number $k = N/2$ is often observed in numerical simulations when N is even in Eqs. (4.1) and (4.2). For this wave number, two clusters form in the array. Within each cluster, individual laser intensities oscillate in-phase

while SCL's pertaining to different clusters differ by a phase shift of π in their relaxation oscillations. Such a situation is depicted in Fig. 4.7. The denominator in (4.29) indicates that the growth rate of the amplitude of this self-pulsing state with ΔK is maximum for $\cos(2\bar{\Omega}t_D) = -1$. Such a resonance condition with respect to the frequency $2\bar{\Omega}$ is connected to the fact that the total reflected field oscillates at twice the oscillation frequency of the individual lasers if the laser array is in the $k = N/2$ state. Indeed, let us reconstruct $E_{tot} = \sum_{j=1}^N E_j$ using (4.15), (4.19), and $\phi_j = \Delta\omega\tau$, $z_j = (-1)^j \rho \exp(i\Delta\Omega\tau)$,

$$\begin{aligned} E_{tot} &\propto \cos(\rho \cos(\bar{\Omega}t + \Delta\Omega\tau)) + O(\rho/\alpha) \\ &\simeq J_0(\rho) - 2J_2(\rho) \cos(2\bar{\Omega}t + 2\Delta\Omega\tau). \end{aligned}$$

With the increase of the coupling strength a symmetry breaking instability of the $k = N/2$ solution takes place by which the two antiphase clusters acquire different optical phases. In order to demonstrate this phenomenon, we substitute into (4.20) a perturbed antiphase solution in the form $\phi_j = \Delta\omega\tau + (-1)^j \delta\phi$, $z_j = (-1)^j \rho \exp(i\Delta\Omega\tau) + (-1)^j \delta z$ and derive linearized equations for $\delta\phi$ and δz . In the particular case $\cos(\omega t_D) = 1$, the equation for $\delta\phi$ does not depend on δz and is

$$\frac{d\delta\phi}{d\tau} = -KJ_0(2\rho \cos(\bar{\Omega}t_D/2)) \delta\phi.$$

Accordingly, the symmetry breaking bifurcation arises when $J_0(2\rho \cos(\bar{\Omega}t_D/2))$ becomes negative with increasing ρ . The total field for the solution with the optical phase difference $\delta\phi$ of the antiphase clusters can be written as

$$E_{tot} \propto \cos(\rho \cos(\bar{\Omega}t + \Delta\Omega\tau) + \delta\phi) + O(\rho/\alpha)$$

Note that the trigonometric expression above possesses two distinct minima at $\cos(\delta\phi \pm \rho)$. Similar feature is exhibited by the antiphase self-pulsing regime bifurcating at $\eta = 1.49$ in Fig. 4.5.

Two antiphase clusters can appear in the array if N is odd, except that one laser does not belong to any cluster. The first order amplitude equations (4.20) predict that this laser is in steady state. Higher order effects lead to corrections in the form of very small amplitude oscillations. This behavior is illustrated in Fig. 4.11 and corresponds to the branch of solution labelled A-P in Fig. 4.5. In Fig. 4.11, two antiphase clusters are formed by the lasers 1,2 and 4,5, whereas laser 3 is almost cw. The self-pulsing solution with two antiphase clusters and a single cw laser can be described analytically with the help of Eqs. (4.20). Looking for a solution of the form $z_1 = 0$, $z_{j>1} = (-1)^j \rho \exp(i\Delta\Omega\tau)$, $\phi_{j>1} = \Delta\omega\tau$, $\phi_1 = \Delta\omega\tau - \delta\phi$ and using the self-consistency condition $d\phi_1/d\tau = d\phi_{j>1}/d\tau$ we get a transcendental equation for the optical phase lag $\delta\phi$:

$$(N-2) \cos \delta\phi - N \cot \omega t_D \sin \delta\phi = \frac{(N-1)[J_0(\rho_+) + J_0(\rho_-)] - 2}{2J_0(\rho)} \quad (4.30)$$

where $\rho_+ = 2\rho \cos(\bar{\Omega}t_D/2)$ and $\rho_- = 2\rho \sin(\bar{\Omega}t_D/2)$. The amplitude ρ and the coupling parameter K are related by

$$K^{-1} = \cos(\omega t_D + \delta\phi) \frac{J_1(\rho)}{N\rho} + \frac{N-1}{N} \cos(\omega t_D) \frac{\rho_- J_1(\rho_-) + \rho_+ J_1(\rho_+)}{4\rho^2} \quad (4.31)$$

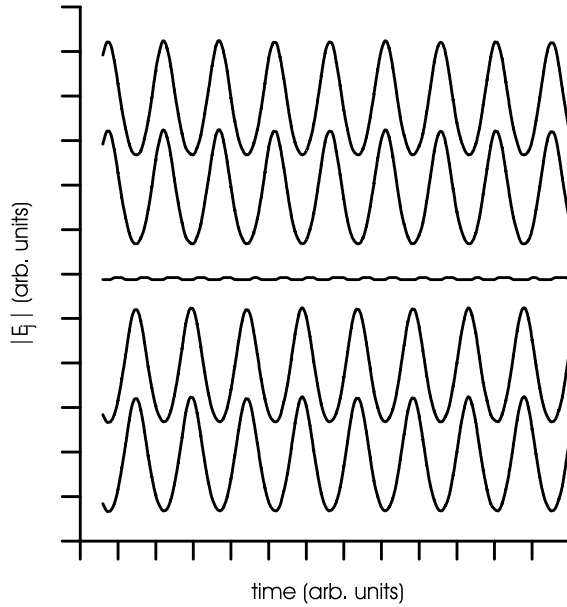


Figure 4.11: Laser intensities for the antiphase self-pulsing branch A-P of Fig. 4.5. $\eta = 1.12 \cdot 10^{-3}$. The intensity oscillations are locally extinguished in the array

Due to the permutation symmetry of the problem with $\chi = 0$, the laser indices can be rearranged such that the $(N - 1)/2$ first lasers belong to the first cluster and the $(N - 1)/2$ last lasers form the second cluster. The cw laser is thus at the center and can be viewed as a transition point between the two clusters where a sudden relaxation phase shift of π takes place. Numerical simulations with nonzero but small χ and the boundary conditions $E_0 = E_{N+1} = 0$ lead to such a situation. This state of synchronization can therefore be viewed as a discrete analog of a domain wall.

4.6 Conclusion

We have studied the synchronization properties of a SCL array subjected to a delayed global coupling through optical feedback. If the lasers are identical and the coupling strength is below the self-pulsing threshold, the array dynamics can be modelled with Kuramoto phase equations (4.3) that include a time delay. Depending on the optical dephasing of the feedback field, the coupling induces either in-phase or antiphase cw synchronization. Increasing the time delay, the stability domains expand for the in-phase cw states, whereas they shrink and tend to disappear for the antiphase cw states (compare Figs. 4.3 and 4.4). In the more realistic situation where there is a distribution of the SCL's optical frequencies, the coupling strength must exceed some critical value η_c in order to establish synchronization. An estimation of η_c , given by (4.8), can be obtained from the Kuramoto model (4.3) in the limit of an infinitely large array [18, 19]. We note, however, that a more complete description of the laser synchronization properties can be expected from our extended model (4.17) because it takes into account weakly damped relaxation oscillations. These oscillations are typical of solid state and semiconductor lasers. Though damped, they could degrade the synchronization properties of the array. Recently, it was shown that a second order derivative term included into the Kuramoto phase equations can increase the in-phase synchronization threshold [30].

As the coupling strength exceeds the Hopf bifurcation threshold, the laser intensities display undamped oscillations. They exhibit either in-phase or antiphase pulsations with a frequency close to the relaxation oscillations frequency Ω of the solitary SCL. Antiphase dynamics is a common feature typical of many other systems consisting of globally coupled identical elements [11, 33, 34]. A Hopf bifurcation leading to antiphase dynamics exists even in the absence of time delay. This bifurcation is highly degenerate and give rise to various type of antiphase relaxation oscillation in the array output. Among these, we have described a particular antiphase state featuring extinction of the sustained relaxation oscillations of a single laser. The existence of such stable regime was verified by means of numerical simulations of the original laser equations (4.1) and (4.2). If a weak local coupling is added to the system the cw laser becomes a discrete analog of a domain wall.

The in-phase self-pulsing instability can appear only if $\Omega t_D = \mathcal{O}(1)$. For moderate delays, i.e., $\Omega t_D = \mathcal{O}(1)$, which of the two selfpulsing bifurcations destabilize the cw in-phase state depends on the relaxation dephasing between the emitted and reinjected fields. In this case, we found that even if the antiphase Hopf bifurcation takes place first, the in-phase self-pulsing solution can become stable with the increase of the coupling strength as it is illustrated by Fig. 4.5. On the other hand, for large delays verifying $t_D \gtrsim \pi\gamma^{-1} (2\bar{P} + 1)^{-1}$, the in-phase bifurcation always precedes the antiphase one, thus preserving in-phase synchrony in the self-pulsing regime.

Above the selfpulsing threshold, the phase equations (4.3) are no more valid. Therefore, in order to describe the self-pulsing dynamics, we derived an extended version of the Kuramoto model with higher order derivative terms (4.17). Using a perturbation method, we reduced Eqs. (4.17) to the amplitude equations (4.20). This allowed us to describe analytically various self-pulsing solutions emerging from the Hopf bifurcations and discuss their stability. In particular, we have studied secondary antiphase bifurcations of the in-phase self-pulsing solution. For moderate delays, $\Omega t_D = \mathcal{O}(1)$, these bifurcations can destroy the synchrony of the in-phase self-pulsing regime and, hence, decrease the amplitude of the total field $\sum_{j=1}^N E_j$. However, if $t_D \sim \gamma^{-1}$, they are bypassed by another secondary bifurcation that leads to in-phase synchronized output with quasiperiodic laser intensities. Numerically, in-phase synchrony is then seen to persists even in the chaotic regimes.

Thus we can conclude that the effect of time delay is essentially to increase the complexity of the array dynamics by producing new branches of in-phase cw, periodic, quasiperiodic or chaotic solutions. The symmetry of the global coupling imposes that these solutions lie within the in-phase synchronization manifold where all the elements of the array behaves identically. For large delays, the bifurcations by which in-phase solutions are created precede antiphase instabilities. In this way, the phase trajectory may be kept in the in-phase synchronization manifold.

Appendix to Chapter 4

4.A Linear stability analysis with nonzero local coupling

4.A.1 In-phase cw state

The in-phase solutions of (4.3) with nonzero value of χ are given by $\phi_j = \phi_k = \omega t$ with the common frequency ω obeying the transcendental equation

$$\omega = \bar{\omega} - \sqrt{1 + \alpha^2} [\eta \sin(\omega t_D - \cot^{-1} \alpha) + \chi \sin(\zeta - \cot^{-1} \alpha)]. \quad (4.32)$$

Below the self-pulsing threshold, the linear stability analysis of the in-phase cw state can be performed by substituting

$$\phi_j = \omega t + \varepsilon \sum_{k=1}^N \delta\phi_k e^{2ijk/N}, \quad (4.33)$$

into (4.3) and collecting $\mathcal{O}(\varepsilon)$ terms. The linearized equations for $\delta\phi_k$ yield the stability conditions

$$\eta \cos(\omega t_D - \cot^{-1} \alpha) + 2\chi \cos(\zeta - \cot^{-1} \alpha) \sin^2\left(\frac{k\pi}{N}\right) > 0, \quad (4.34)$$

where $k = 1, \dots, N - 1$. The effect of the local coupling on the stability of the in-phase cw regimes depends on the relative phase between the global and local couplings. If the two cosine functions in (4.34) have the same sign, local coupling almost does not change the stability domain of the cw-inphase solution for large N . Otherwise this stability domain decreases with increasing local coupling strength χ . This was also observed in [26].

Letting $\chi \rightarrow 0$, the bifurcations defined by (4.34) merge into a single $(N - 1)$ -fold degenerate bifurcation. Then, solving successively (4.34) and (4.4), one finds the instability domains of the in-phase cw state in the $(\bar{\omega}t_D, \eta)$ parameter plane given by

$$\frac{\pi}{2} + \eta t_D \sqrt{1 + \alpha^2} \leq \bar{\omega}t_D - \cot^{-1} \alpha - 2n\pi \leq \frac{3\pi}{2} - \eta t_D \sqrt{1 + \alpha^2}, \quad (4.35)$$

Besides the desynchronization boundaries (4.35), a linear stability analysis of (4.9) and (4.10) reveals the existence of two different types of Hopf bifurcations leading to self-pulsing solutions. The bifurcations of the first type are associated with perturbations transverse to the synchronization manifold $\{E_1 = \dots = E_N, Z_1 = \dots = Z_N\}$. In the limit $\eta, \chi, \gamma \ll 1$, these bifurcations are defined by the condition

$$\eta = \eta_{H1}(k) \equiv \sec(\omega t_D + \cot^{-1} \alpha) \left[\frac{\gamma(1 + 2\bar{P})}{\sqrt{1 + \alpha^2}} - 2\chi \sin^2\left(\frac{\pi k}{N}\right) \cos(\zeta + \cot^{-1} \alpha) \right], \quad (4.36)$$

with $k = 1, \dots, N - 1$. The associated relaxation oscillation frequency is $(2\gamma\bar{P})^{1/2}$. If

$$\cos(\zeta + \cot^{-1} \alpha) < 0,$$

the lowest bifurcation threshold (4.11) corresponds to $k = 1$. In the limit $N \rightarrow \infty$ it coincides with the threshold in the absence of local coupling. On the contrary, if

$$\cos(\zeta + \cot^{-1} \alpha) > 0,$$

the self-pulsing threshold is lowered by the local coupling, even for large N . As $\chi \rightarrow 0$ the bifurcation given by (4.36) merge into a single $(N - 1)$ -fold Hopf bifurcation.

4.A.2 Anti-phase cw state

The stability of the state (4.6) can be assessed using a discrete Fourier transformation similar to (4.33). This gives

$$\chi \cos(\zeta - \cot^{-1} \alpha) \cos\left(\frac{2M\pi}{N}\right) \sin^2\left(\frac{k\pi}{N}\right) > 0, \quad (4.37)$$

with $k = 1, \dots, N, k \neq M, N - M$ and

$$\eta \cos(\omega t_D - \cot^{-1} \alpha) - 4\chi \cos(\zeta - \cot^{-1} \alpha) \cos\left(\frac{2M\pi}{N}\right) \sin^2\left(\frac{M\pi}{N}\right) < 0, \quad (4.38)$$

where ω verifies the transcendental equation

$$\omega = \bar{\omega} - \sqrt{1 + \alpha^2} \left[\frac{\eta}{2} \sin(\omega t_D - \cot^{-1} \alpha) + 2\chi \sin^2\left(\frac{M\pi}{N}\right) \sin(\zeta - \cot^{-1} \alpha) \right]. \quad (4.39)$$

The stability boundaries defined by (4.37) and (4.38) correspond to Hopf bifurcations with the frequency $\omega - \bar{\omega}$. According to the stability condition (4.37), the local coupling selects the antiphase states with M such that $\cos(\zeta - \cot^{-1} \alpha) \cos(2M\pi/N) > 0$. It then follows from (4.38) that the stability domain of these states increases with χ .

Letting $\chi \rightarrow 0$ in (4.37), one obtains $N - 2$ zero eigenvalues. In addition, there is a zero eigenvalue associated with the invariance of (4.3) under the global phase shift $\phi_j \rightarrow \phi_j + \text{const.}$ Finally, combining expressions (4.38) and (4.39), we find the triangular regions (4.7) in the $(\bar{\omega}t_D, \eta)$ parameter space where the antiphase state is neutrally stable.

4.B Derivation of the generalized phase equations

Substituting (4.15) and (4.16) into (4.1) and (4.2) yields

$$\frac{dx_j}{dt} = -\gamma(1 + 2P_j)x_j - \Omega_j y_j + O(\sqrt{\gamma}/\alpha), \quad (4.40)$$

$$\begin{aligned} \frac{dy_j}{dt} = & \Omega_j x_j + \frac{\alpha\eta}{N} \sum_{n=1}^N \sin[\delta_{jn} + \Phi_j - \Phi_n(t - t_D)] + \frac{\alpha\chi}{2} \sum_{p=j-1, j+1} \sin(\zeta + \Phi_j - \Phi_p) \\ & + O(\sqrt{\gamma}/\alpha, \eta, \chi, \alpha\eta\delta P_j, \alpha\chi\delta P_j), \end{aligned} \quad (4.41)$$

$$\frac{d\Phi_j}{dt} = \omega_j + \Omega_j x_j + O(\eta, \chi). \quad (4.42)$$

where $\delta P_j = P_j/\bar{P} - 1$. In these equations, we keep terms of order $\alpha\eta$, $\alpha\chi$, and γ because they are of the same order at the bifurcation points (4.11) and (4.12). Differentiating Eq. (4.42) twice with respect to time and using (4.40) and (4.41), one obtains Eqs. (4.17).

Next, we introduce the two time scales in (4.18) and expand the dependent variables in (4.40)-(4.42) as

$$\begin{aligned} x_j &= x_j^{(0)}(s, \tau) + \sqrt{\gamma}x_j^{(1)}(s, \tau) + \dots, \\ y_j &= y_j^{(0)}(s, \tau) + \sqrt{\gamma}y_j^{(1)}(s, \tau) + \dots, \\ \Phi_j &= \bar{\omega}t + \Phi_j^{(0)}(s, \tau) + \sqrt{\gamma}\Phi_j^{(1)}(s, \tau) + \dots. \end{aligned} \quad (4.43)$$

Collecting $O(\gamma^0)$ terms, we get

$$\left(\frac{\partial}{\partial s} - \mathcal{L} \right) \begin{pmatrix} x_j^{(0)} \\ y_j^{(0)} \\ F_j^{(0)} \end{pmatrix} = 0, \quad \mathcal{L} = \begin{pmatrix} 0 & -1 & 0 \\ 1 & 0 & 0 \\ 1 & 0 & 0 \end{pmatrix}. \quad (4.44)$$

This equation has the solution

$$x_j^{(0)} = -\text{Im}[z_j(\tau)e^{is}], \quad y_j^{(0)} = \text{Re}[z_j(\tau)e^{is}], \quad \Phi_j^{(0)} = \phi_j(\tau) + \text{Re}[z_j(\tau)e^{is}]. \quad (4.45)$$

Next, equating the terms of order $\gamma^{1/2}$, we obtain

$$\left(\frac{\partial}{\partial s} - \mathcal{L} \right) \begin{pmatrix} x_j^{(1)} \\ y_j^{(1)} \\ F_j^{(1)} \end{pmatrix} = \frac{\bar{P} + 1/2}{\sqrt{2\bar{P}}} \vec{\mathcal{B}}. \quad (4.46)$$

The quantity $\vec{\mathcal{B}}$ in the r.h.s. of (4.46) is computed using the following properties of Bessel functions:

$$\sin[\bar{\omega}t_D + \vartheta_{jn} + \Phi_j^{(0)} - \Phi_n^{(0)}(s - s_D)] = J_0(|z_{jn}|) \sin \phi_{jn} + \frac{J_1(|z_{jn}|)}{|z_{jn}|} (z_{jn}e^{is} + c.c.) \cos \phi_{jn} + h.h.,$$

and

$$\sin(\zeta + \Phi_j^{(0)} - \Phi_q^{(0)}) = J_0(|w_{jq}|) \sin \xi_{jq} + \frac{J_1(|w_{jq}|)}{|w_{jq}|} (w_{jq}e^{is} + c.c.) \cos \xi_{jq} + h.h.,$$

where *c.c.* and *h.h.* means “complex conjugate” and “higher harmonics”, respectively. This yields

$$\begin{aligned} \vec{\mathcal{B}} &= -\frac{\partial}{\partial \tau} \begin{pmatrix} x_j^{(0)} \\ y_j^{(0)} \\ \Phi_j^{(0)} \end{pmatrix} + \begin{pmatrix} -2x_j^{(0)} - \delta\Omega_j y_j^{(0)} \\ \delta\Omega_j x_j^{(0)} \\ \delta\omega_j \end{pmatrix} + \begin{pmatrix} 0 \\ 1 \\ 0 \end{pmatrix} \left\{ \frac{K}{N} \sum_n \left[\sin \phi_{jn} J_0(|z_{jn}|) \right. \right. \\ &\quad \left. \left. + \cos \phi_{jn} \frac{J_1(|z_{jn}|)}{|z_{jn}|} (z_{jn}e^{is} + c.c.) \right] + \frac{X}{2} \sum_{q=j-1, j+1} \left[\sin \xi_{jq} J_0(|w_{jq}|) \right. \right. \\ &\quad \left. \left. + \cos \xi_{jq} \frac{J_1(|w_{jq}|)}{|w_{jq}|} (w_{jq}e^{is} + c.c.) \right] \right\} + h.h. \end{aligned}$$

The existence of non trivial solutions of Eq. (4.46) implies the orthogonality conditions or solvability conditions

$$\int_0^{2\pi} \vec{v}_0 \cdot \vec{\mathcal{B}} ds = 0, \quad \int_0^{2\pi} \vec{v}_\pm \cdot \vec{\mathcal{B}} e^{\pm is} ds = 0,$$

where $\vec{v}_0 = (0, 1, -1)$ and $\vec{v}_\pm = (\mp i, 1, 0)$ are the left eigenvectors of \mathcal{L} associated with the eigenvalues 0 and $\pm i$, respectively. These solvability conditions lead to Eqs. (4.20).

The error in Eqs. (4.20) related to the assumption $\alpha \gg 1$ can be estimated near the Hopf bifurcation points. To this end, we introduce a small parameter ε by

$$K = K_H + \varepsilon^2 K_2,$$

and seek periodic solution of the form

$$f_j = \operatorname{Re}(\varepsilon f_{j,1} e^{is} + \dots), \quad f_j = x_j, y_j, \Phi_j - \bar{\omega}t.$$

This produces a set of linear differential equations at each order in ε . At third order, the solvability condition yields the corrected version of Eq. (4.20) in the vicinity of the bifurcation point:

$$\begin{aligned} \frac{dz_j}{d\tau} &= -\frac{i\sqrt{2\bar{P}}}{12\alpha^2\sqrt{\gamma}(2\bar{P}+1)} z_j |z_j|^2 \\ &+ \frac{K_H \cos \psi}{16N} \sum_n z_{jn} \left(8 \frac{K - K_H}{K_H} - |z_{jn}|^2 \right) + O(\alpha^{-1}). \end{aligned}$$

The principal correction to Eq. (4.20) close to the bifurcation point is thus $O(\alpha^{-2}\gamma^{-1/2})$. Since it is imaginary, it only affects the relaxation frequency and not the amplitude of the oscillations. The next corrections are only $O(\alpha^{-1})$, which explains the good agreement between numerical and theoretical curves in Figs. 4.5 and 4.10.

References

- [1] M. Tamburini, L. Goldberg, D. Mehuys, *Appl. Phys. Lett.* **60**, 1292 (1992); H. Adachibara, O. Hess, E. Abraham, P. Ru, and J. V. Moloney, *J. Opt. Soc. Am. B* **10**, 658 (1993); J. R. Marciano and G. P. Agrawal, *IEEE J. Quant. Electron.* **32**, 590 (1996).
- [2] O. Hess, *Fundamental issues of nonlinear laser dynamics*, AIP Conference proceedings, Vol. **48** (Melville, New York 2000), 128-149; J. V.J. G. McInerney et al., *ibid.* 173-191.
- [3] H.G. Winful and S.S. Wang, *Appl. Phys. Lett.* **53**, 1894 (1988).
- [4] S.S. Wang and H.G. Winful, *Appl. Phys. Lett.* **52**, 1774 (1988).
- [5] R.-D. Li and T. Erneux, *Opt. Comm.* **99**, 196 (1993).
- [6] S. Y. Kourtchatov, V. V. Likhanskii, A. P. Napartovich, F. T. Arecchi, and A. Lapucci, *Phys. Rev. A* **52**, 4089 (1995).
- [7] S. Wolff and H. Fouckhardt, *Optics Express* **7**, 222 (2000).
- [8] B. Chann, I. Nelson, and T. G. Walker, *Opt. Lett.* **25**, 1352 (2000).
- [9] J. Garcia-Ojalvo, J. Casademont, C. R. Mirasso, M. C. Torrent, and J. M. Sancho, *Int. J. of Bif. and Chaos* (2000).
- [10] J. Yaeli, W. Streifer, D. R. Scifres, and P. S. Cross, *Appl. Phys. Lett.* **47**, 89 (1985); C. Chang-Hasnain, D. F. Welch, D. R. Scifres, J. R. Whinnery, A. Dienes, and R. D. Burnham, *Appl. Phys. Lett.* **49**, 614 (1986); C. J. Chang-Hasnain, J. Berger, D. R. Scifres, W. Streifer, J. R. Whinnery, and A. Dienes, *Appl. Phys. Lett.* **50**, 1465 (1987); J. R. Leger, *Appl. Phys. Lett.* **55**, 334 (1989); F. X. D'Amato, E. T. Siebert, and C. Roychoudhuri, *Appl. Phys. Lett.* **55**, 816 (1989); J. R. Leger, M. L. Scott, and W. B. Veldkamp, *Appl. Phys. Lett.* **52**, 1771 (1988); V. P. Kandidov and A. V. Kondratev, *Laser Physics*, **10**, 1089 (2000); A.F.Glova, *Laser Physics*, **10**, 975 (2000).
- [11] K. Wiesenfeld, C. Bracikowski, G. James, and R. Roy, *Phys. Rev. Lett.* **65**, 1749 (1990); C. Bracikowski and R. Roy, *Chaos* **1**, 49 (1991); K. Otsuka, *Phys. Rev. Lett.* **67**, 1090 (1991); S. Bielawski, D. Derozier, and P. Glorieux, *Phys. Rev. A* **46**, 1692 (1992). J.-Y. Wang and P. Mandel, *Phys. Rev. A* **48**, 671 (1993); J.-Y. Wang, P. Mandel, and T. Erneux, *Quantum Semiclassic. Opt.* **7**, 169 (1994); J.-Y. Wang and P. Mandel, *Phys. Rev. A* **52**, 1474 (1995).
- [12] A.G. Vladimirov, E.A. Viktorov, and P. Mandel, *Phys. Rev. E* **60**, 1616 (1999).
- [13] K. Wiesenfeld, P. Colet, and S. H. Strogatz, *Phys. Rev. Lett.* **76**, 404 (1996).
- [14] Y. Kuramoto, *Chemical Oscillations, Waves, and Turbulence* (Springer-Verlag, Berlin, 1984).
- [15] H. Sompolinsky, D. Golomb, and D. Kleinfeld, *Proc. Nat. Acad. Sci. USA* **87**, 7200 (1990).

- [16] Z. Neda, E. Ravasz, T. Vicsek, Y. Brechet, and A. L. Barabasi, Phys. Rev. E **61**, 6987 (2000).
- [17] S. H. Strogatz, Physica D **143**, 1 (2000).
- [18] M. K. S. Yeung and S. H. Strogatz, Phys. Rev. Lett. **82**, 648 (1999).
- [19] M. Y. Choi, H. J. Kim, D. Kim, and H. Hong, Phys. Rev. E **61**, 371 (2000).
- [20] S. Kim, S. H Park, and C. S. Ryu, Phys. Rev. Lett. **79**, 2911 (1997).
- [21] D. V. Ramana Reddy, A. Sen, and G. L. Johnston, Phys. Rev. Lett. **80**, 5109 (1998).
- [22] G. Kozyreff, A. G. Vladimirov, and P. Mandel, Phys. Rev. Lett. **85**, 3809 (2000).
- [23] R. Lang and K. Kobayashi, IEEE J. Quantum Electron. **QE-16**, 347 (1980).
- [24] Motoichi Ohtsu, *Highly Coherent Semiconductor Lasers*, pp. 124-140 (Artech House, Bristol, 1992).
- [25] D. Lenstra, B.H. Verbeek, and A.J. den Boef, IEEE J. Quantum Electron. **QE-21**, 674 (1985); Y. Cho and T. Umeda, Opt Commun. **59**, 131 (1986); J. Mork, B. Tromborg, and J. Mark, IEEE J. Quantum Electron. **28**, 93 (1992); G.H.M. van Tartwijk and D. Lenstra, Quantum Semiclass. Opt. **7**, 87 (1995); D. Pieroux, T. Erneux, K. Otsuka, Phys. Rev. A **54**, 3409 (1994); P. Saboureau, J.-P. Foing, and P. Schanne, IEEE J. Quantum Electron. **33**, 1582 (1997).
- [26] M. Silber, L. Fabiny, and K. Wiesenfeld, J. Opt. Soc. Am. **B10**, 1121 (1993).
- [27] S. Nichols and K. Wiesenfeld, Phys. Rev. A **45**, 8430 (1992).
- [28] S.H. Strogatz and R.E. Mirollo, Phys. Rev. E **47**, 220 (1993).
- [29] T. W. Carr, D. Pieroux, and P. Mandel, Phys. Rev. A **63**, 033817 (2001).
- [30] J. A. Acebrón and R. Spigler, Phys. Rev. Lett. **81**, 2229 (2000); J. A. Acebrón, L. L. Bonilla, and R. Spigler, Phys. Rev. E **62**, 3437 (2000).
- [31] L.L. Bonilla, Phys. Rev. E **62**, 4862 (2000).
- [32] P.M. Alsing, V. Kovanis, A. Gavrielides, and T. Erneux, Phys. Rev. A **53**, 4429 (1996).
- [33] P. Hadley and M.R. Beasley, Appl. Phys. Lett. **50**, 621 (1987); K. Wiesenfeld and P. Hadley, Phys. Rev. Lett. **62**, 1335 (1989); K. Yoshimoto, K. Yoshikawa, Y. Mori, and I. Hanazaki, Chem. Phys. Lett. **189**, 18 (1992); W.J. Freeman and C.A. Skarda, Brain Res. Rev. **10**, 47 (1985).
- [34] P. Mandel 1997 *Theoretical Problems in Cavity Nonlinear Optics* (Cambridge: Cambridge University Press).
- [35] Numerical simulations were performed with "Dynamics Solver" by J.M. Aguirregabiria available at <http://tp.lc.ehu.es/jma.html>

Chapter 5

Atomic interference in a microchip laser

5.1 Introduction

Much attention has been devoted in the last decade to atomic interference as a mechanism mediating light-matter interaction [1, 2, 3, 4, 5]. This resulted from a shift of emphasis from the two-level atomic system to a three-level atomic system with at least two fields or lasing cavity modes in a Λ or V scheme. Both founding papers [6, 7] exploited atomic interference to prove that there is a domain in which gain and even lasing could be achieved without population inversion, as clearly explained in [8]. Starting from these premisses, the work that followed focused on inversionless atomic systems, adding atomic levels and/or driving and probe fields to the original models.

In this chapter, we consider another situation connected to the same family of processes: atomic interference in a laser with population inversion. Experimental results have been reported recently on the lasing properties of the $\text{LiNdP}_4\text{O}_{12}$ (LNP in short) crystal prepared in the form of a microchip. First, it has been shown numerically and experimentally that this laser displays an unusual input-output power characteristics (the quadratic-to-quartic, or Q2Q, transition[9]) followed by a self-pulsing instability [10]. It was also found that beyond the Q2Q transition, the number of lasing modes decreases and the laser eventually becomes single mode for high pumping rates (typically seven times above the lasing threshold) [11]. Spectroscopic data indicate that these multimode regimes are generated by transitions that connect N levels of the $^4I_{11/2}$ manifold of neodymium to a single level of the more energetic $^4F_{3/2}$ manifold. Each transition is in general single mode. Thus, the two-mode regime is associated with the usual Λ scheme. The regimes with more than two branches emanating from the upper level will be referred to as n- Λ schemes. The dynamics of an LNP laser operating in this multimode regime is by no means simple. First, it has been shown experimentally and numerically that there is a self-pulsing threshold corresponding to the instability of a low-frequency relaxation oscillation. This indicates that the usual rate equations are inadequate to describe this regime since they predict the complete absence of instability. Second, the selfpulsing regime is characterized by a strong manifestation of antiphase dynamics resulting in a total intensity which is practically constant despite large amplitude oscillations of the modal intensities. In a recent publication [10], the modelisation of this laser has been discussed for three-mode operation. Based on numerical evidence, it appears that a sufficient description is obtained if the optical atomic coherences are adiabatically eliminated while retaining the low frequency atomic coherence among the sublevels of the $^4I_{11/2}$ manifold, in

addition to the modal intensities and the atomic population dynamics. A further simplification derives from the fact that the levels in $^4I_{11/2}$ are short-lived compared to those in $^4F_{3/2}$ [12]. Hence the population inversions between these two manifolds are all given essentially by the population in $^4F_{3/2}$. Lasing without population inversion is therefore excluded in this system. We do not mean, however, that the populations in the manifold $^4I_{11/2}$ vanish; otherwise, there could be no atomic coherence in it. Another consequence of this fact is that the population inversion cannot be negative. Hence, spatial variations of the pump profile can not be the cause of sustained relaxation oscillations, through the mechanism described in Chapter II. Starting from these conclusions, this chapter presents a theoretical study of the n- Λ scheme that is applicable to the LNP microchip laser.

In the experimental setup [9], the laser cavity is end-pumped by a laser diode. In contrast with [10], we do not attempt to discuss the influence of the penetration depth of the pump beam. Rather, we concentrate on the role of the atomic coherence between the low levels of the system on the laser dynamics.

This chapter is organized as follows. In Sec. 5.2, we introduce the n- Λ model. We derive the steady states and discuss their stability for an arbitrary number of atomic transitions. In order to go one step further in the analysis, in Sec. 5.3, we focus our attention to the case of two transitions. With this simplification and the assumption that the two atomic lines have the same strength, we can explicitly analyze the self-pulsing solution. We draw our conclusions in the next section.

These results were published in [13].

5.2 Derivation of the model

We consider an atomic system having N optical transitions between an energy level $|0\rangle$ and a set of closely spaced lower energy levels $|p\rangle$ with $p = 1, \dots, N$, as shown in Fig. 5.1. From the above discussion, we assume that the low levels remain almost unpopulated so that we approximate the difference $\rho_{00} - \rho_{pp}$ by ρ_{00} , where ρ is the density operator. In addition, we assume that the Fabry-Perot cavity, of length L , supports a resonant field mode with each optical transition $0 \leftrightarrow p$. We thus write the electric field as

$$E(z, t) = \sum_{p=1}^N (E_p(t) e^{i\omega_p t} + c.c.) \sin(k_p z). \quad (5.1)$$

where ω_p is the atomic frequency between levels $|0\rangle$ and $|p\rangle$, and k_p is the associated wave number. The relaxation rates of ρ_{pq} , ρ_{p0} , and ρ_{00} are noted Γ_{pq} , γ_{\perp} , and γ_{\parallel} , respectively, while the cavity damping rate is noted Γ_c . A lower bound of Γ_{pq} is given by the population decay rates in levels $|p\rangle$ and $|q\rangle$. According to our hypothesis, they are short-lived compared to level $|0\rangle$, so we have $\Gamma_{pq} \gg \gamma_{\parallel}$. Spectroscopic data exist for the $^4I_{11/2}$ manifold of neodymium in glassy materials [14]. The decay rates of these levels are found to be comparable to the cavity damping rate Γ_c of the microchip laser in [10]. Rather than supposing that $\Gamma_{pq} \gg \Gamma_c$, we will assume that $\Gamma_{pq} = O(\Gamma_c)$ and define the ratio

$$\gamma_{pq} = \frac{\Gamma_{pq}}{\Gamma_c} = O(1). \quad (5.2)$$

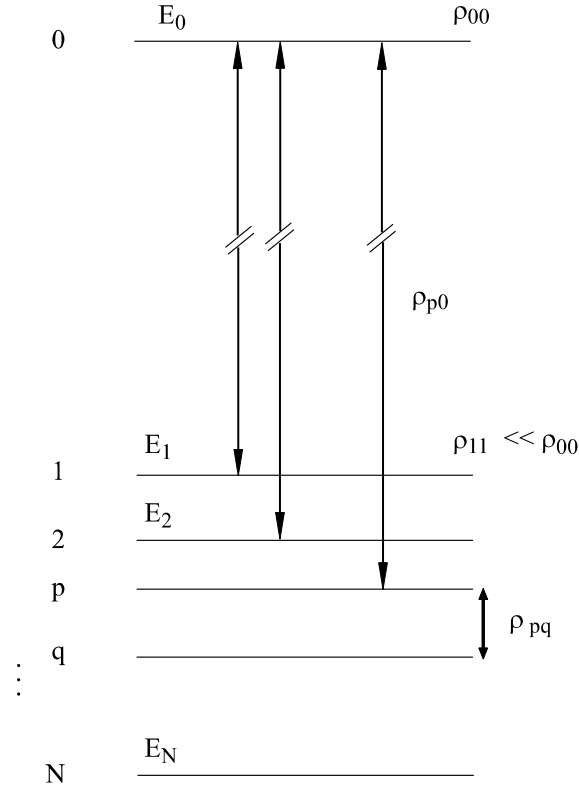


Figure 5.1: The n- Λ scheme. The figure is not to scale with respect to the energies: $E_0 - E_1 \gg E_1 - E_N$.

In order to treat quantities of order unity, we introduce the dimensionless variables

$$\mathcal{E}_p = \frac{d_p E_p}{\hbar \sqrt{\gamma_{\parallel} \gamma_{\perp}}}, \quad D = \frac{\mathcal{N} \omega |d|^2}{\varepsilon_0 \hbar \gamma_{\perp} \Gamma_c} \rho_{00}, \quad (5.3)$$

where $\omega |d|^2 = \max_p \{\omega_p |d_p|^2\}$, $d_p = \langle p | -e \vec{r} | 0 \rangle$, and \mathcal{N} is the density of atoms. On the other hand, the atomic coherence between states p and q is rescaled as

$$S_{pq} = \frac{\Gamma_{pq}}{\gamma_{\parallel}} \frac{\mathcal{N} \omega |d|^2}{\varepsilon_0 \hbar \gamma_{\perp} \Gamma_c} \rho_{pq} e^{i(\omega_q - \omega_p)t}. \quad (5.4)$$

Assuming that $\gamma_{\perp} \gg \gamma_{\parallel}, \Gamma_{pq}, \Gamma_c$, we can eliminate the optical polarization adiabatically in the Maxwell-Bloch equations. In addition, we rescale time as $t_{\parallel} = \gamma_{\parallel} t$. With the inversion lifetime as the time unit, the cavity damping rate is rescaled as $\kappa = \Gamma_c / \gamma_{\parallel}$. In the slowly varying envelope and rotating wave approximations, this yields a variant of the global rate

equations (3.2) and (3.3) encountered in Chapter II:

$$\begin{aligned} \frac{d\mathcal{E}_p(t_{||})}{dt_{||}} &= \frac{\kappa}{2} \left(-1 + \mathcal{L}_p \frac{1}{L} \int_0^L 2D(z, t_{||}) \sin^2(k_p z) dz \right) \mathcal{E}_p(t_{||}) \\ &\quad - \mathcal{L}_p \sum_{q \neq p} \frac{\mathcal{E}_q(t_{||})}{\gamma_{pq}} \frac{1}{L} \int_0^L S_{pq}(z, t_{||}) \sin(k_p z) \sin(k_q z) dz \end{aligned} \quad (5.5)$$

$$\frac{\partial D(z, t_{||})}{\partial t_{||}} = w - D(z, t_{||}) \left(1 + \sum_p 2 |\mathcal{E}_p(t_{||})|^2 \sin^2(k_p z) \right) + O(\kappa^{-1}), \quad (5.6)$$

$$\frac{\partial S_{pq}(z, t_{||})}{\partial t_{||}} = \kappa \gamma_{pq} [-S_{pq}(z, t_{||}) + 2D(z, t_{||}) \mathcal{E}_p(t_{||}) \mathcal{E}_q^*(t_{||}) \sin(k_p z) \sin(k_q z)] + O(1). \quad (5.7)$$

In Eq. (5.6), w is the pump parameter. To simplify this integro-differential system, we follow the same approach as in Chapter II and expand the atomic variables in Fourier series. Being primarily interested in the effect of low-frequency coherence, we take the simplest possible ansatz for the population inversion profile:

$$D(z, t_{||}) \simeq D(t_{||}) + \sum_p N_p(t_{||}) \cos(2k_p z). \quad (5.8)$$

As for the low-frequency atomic coherences, we assume that

$$S_{pq}(z, t_{||}) \simeq S_{pq}(t_{||}) \sin(k_p z) \sin(k_q z). \quad (5.9)$$

In this way, we are left with

$$\frac{d\mathcal{E}_p}{dt_{||}} = \frac{\kappa}{2} \left[-1 + \mathcal{L}_p \left(D - \frac{N_p}{2} \right) \right] \mathcal{E}_p - \frac{\mathcal{L}_p}{4} \sum_{q \neq p} \frac{\mathcal{E}_q S_{pq}}{\gamma_{pq}}, \quad (5.10)$$

$$\frac{dD}{dt_{||}} = w - \left(1 + \sum_q |\mathcal{E}_q|^2 \right) D + \frac{1}{2} \sum_q |\mathcal{E}_q|^2 N_q, \quad (5.11)$$

$$\frac{dN_p}{dt_{||}} = - \left(1 + \sum_q |\mathcal{E}_q|^2 \right) N_p + |\mathcal{E}_p|^2 D, \quad (5.12)$$

$$\frac{dS_{pq}}{dt_{||}} = \kappa \gamma_{pq} \left[-S_{pq} + 2\mathcal{E}_p \mathcal{E}_q^* \left(D - \frac{N_p + N_q}{2} \right) \right]. \quad (5.13)$$

We have checked that the contributions coming from the $O(\kappa^{-1})$ terms in Eq. (5.6) and the $O(1)$ terms in Eq. (5.7) influence negligibly the laser dynamics, so we omit them. Equations (5.10) to (5.13) constitute a first model of a laser operating on the n- Λ scheme. In the absence of low-frequency coherence, they reduce to the TSD equations for a multimode laser [15].

5.2.1 Effect of the low-frequency atomic coherence

In order to assess the physical effect of $S_{pq}(t_{||})$, we first consider its phase. Introducing the amplitude/phase decomposition $\mathcal{E}_p = |\mathcal{E}_p| \exp(i\varphi_p)$, $S_{pq} = |S_{pq}| \exp(i\psi_{pq})$, we get for the

phases

$$\begin{aligned}\frac{d\varphi_p}{dt_{||}} &= \frac{\mathcal{L}_p}{4} \sum_{q \neq p} \frac{|\mathcal{E}_q| |S_{pq}|}{\gamma_{pq} |\mathcal{E}_p|} \sin(\varphi_p - \varphi_q - \psi_{pq}), \\ \frac{d\psi_{pq}}{dt_{||}} &= 2\kappa\gamma_{pq} \frac{|\mathcal{E}_p| |\mathcal{E}_q|}{|S_{pq}|} \sin(\varphi_p - \varphi_q - \psi_{pq}).\end{aligned}\quad (5.14)$$

It follows from Eq. (5.14) that ψ_{pq} evolves rapidly until $\varphi_p - \varphi_q - \psi_{pq}$ is a multiple of 2π . On the other hand, the atomic coherence $S_{pq}(z, t_{||})$ is produced by a two-photon process that involves \mathcal{E}_p and \mathcal{E}_q . Consequently, it is fairly localized at positions z^* inside the cavity where $\sin^2(k_p z^*)$ and $\sin^2(k_q z^*)$ are both maximum. Let us examine the situation $\sin(k_p z^*) \simeq 1$ and $\sin(k_q z^*) \simeq 1$, so that $S_{pq}(z^*, t_{||})$ is given by $S_{pq}(t_{||}) \exp[i\psi_{pq}(t_{||})]$. There, the quantum state $|z^*\rangle$ of the medium is

$$|z^*\rangle = c_p e^{i\omega_p t} |p\rangle + c_q e^{i\omega_q t - i\psi_{pq}} |q\rangle + \sum_{j \neq p, q} c_j e^{i\omega_j t - i\theta_j} |j\rangle, \quad (5.15)$$

with

$$c_p c_q \propto S_{pq}(t_{||}). \quad (5.16)$$

At $z = z^*$, the electric field is essentially proportional to

$$\mathcal{E}_p \exp(i\omega_p t + \varphi_p) + \mathcal{E}_q \exp(i\omega_q t + \varphi_q) + c.c.$$

Therefore, neglecting fast oscillating contributions, the transition probability from this state to the upper state $|p\rangle$ induced by the electric field is, for short times:

$$\begin{aligned}P_{|z^*\rangle \rightarrow |0\rangle} &= \frac{t^2}{\hbar^2} |\langle z^* | erE(z^*, t) | 0 \rangle|^2 \\ &\propto \left| c_p \mathcal{E}_p + c_q \mathcal{E}_q e^{i(\varphi_p - \varphi_q - \psi_{pq})} \right|^2 \\ &\propto |c_p \mathcal{E}_p|^2 + |c_q \mathcal{E}_q|^2 + 2c_p c_q \mathcal{E}_p \mathcal{E}_q \cos(\varphi_p - \varphi_q - \psi_{pq})\end{aligned}\quad (5.17)$$

Since the phases lock to $\varphi_p - \varphi_q - \psi_{pq} = 2\pi$, the last term in (5.17) yields a maximum constructive interference and the absorption is enhanced by the coherence S_{pq} . In this way, the set of low frequency coherences $\{S_{pq}\}$ induces nonlinear absorptions of a purely quantum nature.

It follows from the phase Eq. (5.14) that the dynamics of the amplitudes becomes phase-independent. In the remainder of this chapter, we will therefore consider \mathcal{E}_p and S_{pq} as real.

5.2.2 Steady states

In this section, we study the steady states of the model and analyze their stability. The steady state solutions can be classified according to the set of lasing modes. As a convention, we shall use subscript l to designate a nonlasing mode and subscript m otherwise. The number of lasing mode will be noted N_m . Moreover, it is simpler algebraically to parametrize the steady states in terms of D rather than w . With that in mind, we introduce the quantities $\mathcal{F}_1 = \sum_m \mathcal{L}_m^{-1}$ and $\mathcal{F}_2 = \sum_m \mathcal{L}_m^{-2}$, where the summation is over the lasing modes only. The

parameter κ appearing in Eqs. (5.10) to (5.13) is usually very large, typically between 10^3 and 10^6 , a fact that we will exploit to write down the steady state and to perform the linear stability analysis. In steady state, the non lasing modes give, obviously

$$\mathcal{E}_l, N_l, S_{lm}, S_{ll'} = 0, \quad (5.18)$$

while for the excited mode, we have

$$\begin{aligned} \mathcal{E}_m^2 &= \frac{D - \mathcal{L}_m^{-1}}{\mathcal{F}_1 - (\mathcal{N}_m - 1/2)D} + O(\kappa^{-1}), \\ N_m &= 2(D - \mathcal{L}_m^{-1}) + O(\kappa^{-1}), \\ S_{mm'} &= 2\mathcal{E}_m\mathcal{E}_{m'}(\mathcal{L}_m + \mathcal{L}_{m'} - D) + O(\kappa^{-1}), \\ w &= D + \frac{D\mathcal{F}_1 - \mathcal{F}_2}{\mathcal{F}_1 - (\mathcal{N}_m - 1/2)D} + O(\kappa^{-1}). \end{aligned} \quad (5.19)$$

The leading order part of the steady state solution is identical to the TSD model [16], except for the coherence which do not appear in this model.

5.2.3 Linear stability analysis

Let us now study the linear stability of the solution (5.19). To this end, we define e_p , d , n_p , and s_{pq} as the deviations from the steady state values \mathcal{E}_p , D , N_p , and S_{pq} , respectively. Linearizing Eqs. (5.10) to (5.13), we are lead to solve an eigenvalue problem of the form

$$A.\mathbf{x} = (\kappa A_{-2} + A_0).\mathbf{x} = \lambda \mathbf{x} \quad (5.20)$$

where A is the Jacobian matrix and \mathbf{x} is the vector of deviations from the steady state. The fact that $\kappa \gg 1$ then suggests to introduce the perturbation expansions $\lambda = \kappa \sum_{n=0}^{\infty} \kappa^{-n/2} \lambda_n$ and $\mathbf{x} = \sum_{n=0}^{\infty} \kappa^{-n/2} \mathbf{x}_n$ and to solve the problem for each order in κ , until the desired accuracy is reached. The principal results are given below:

1. The solution (5.19) is stable only if $D < \mathcal{L}_l^{-1}$, which defines the lasing threshold for mode l :

$$w_l = \mathcal{L}_l^{-1} + \frac{\mathcal{L}_l^{-1}\mathcal{F}_1 - \mathcal{F}_2}{\mathcal{F}_1 - (\mathcal{N}_m - 1/2)\mathcal{L}_l^{-1}} + O(\kappa^{-1}). \quad (5.21)$$

2. For any pair of indices p and q , we find the eigenvalue $\lambda_{pq} = -\kappa\gamma_{pq}$. The associated fluctuations affect S_{pq} only and are decoupled from the rest of the system. Hence, any small departure of S_{pq} from its steady state is rapidly damped out.

3. Assuming for simplicity that all lasing modes have equal gain, i.e. $\mathcal{L}_m = 1$ for all m , we find a pair of complex conjugated eigenvalues associated to damped in-phase relaxation oscillations

$$\lambda_{R,\pm} = a \pm i\sqrt{\kappa}\Omega_R, \quad a < 0, \quad \Omega_R = \sqrt{w - 1}. \quad (5.22)$$

4. In the same limit of equal gains, we may write $\mathcal{E}_m^2 = I$ and $S_{mm'} = S$ in steady state. We find $\mathcal{N}_m - 1$ complex conjugate pairs of eigenvalues of the form

$$\lambda_{L,\pm} = \lambda_0 \pm i\sqrt{\kappa}\Omega_L, \quad \Omega_L^2 = \frac{DI}{2}. \quad (5.23)$$

The associated eigenvector is characterized by the constraint $\sum_m e_m = 0$, which is the signature of antiphase dynamics. If we assume that all the coherences decay with the same relaxation constant, $\gamma_{mm'} = \gamma$, the real part λ_0 is given by

$$\lambda_{0,L} = \frac{S}{2\gamma} - (1 + \mathcal{N}_m I), \quad (5.24)$$

and there is a degenerate Hopf bifurcation if $\lambda_{0,L} = 0$. This occurs at a finite pump intensity only if

$$\gamma < \gamma_{\max} = \frac{\mathcal{N}_m - 1}{\mathcal{N}_m(\mathcal{N}_m - 1/2)}. \quad (5.25)$$

This condition of existence for the Hopf instability depends on the cavity and coherence damping rates only through the ratio $\gamma = \Gamma_{pq}/\Gamma_c$.

We have thus found the existence of a Hopf bifurcation connected to the low-frequency atomic coherence in the n- Λ scheme. Indeed, in the absence of this coherence, the system (5.10)-(5.13) would reduce to the TSD equations, which admit only *cw* solutions. In the limit of identical gains, the bifurcation is $(\mathcal{N}_m - 1)$ -fold degenerate and the unstable eigenvectors of the system indicate that the resulting sustained relaxation oscillations are in antiphase. They are therefore not observable in the total intensity close to the bifurcation point. The condition (5.25) of existence of this instability justifies *a posteriori* our assumption that $\Gamma_{pq} = O(\Gamma_c)$ and not $\Gamma_{pq} \gg \Gamma_c$.

5.2.4 Reduction of the model

The second point in the linear stability analysis suggests that, unlike the field variables, we can eliminate S_{pq} adiabatically. This derives from the fact that $\Gamma_{pq} \gg \gamma_{\parallel}$. Such an elimination does not suppress the existence of the Hopf bifurcation point, as long as the ratio $\gamma = \Gamma_{pq}/\Gamma_c < \gamma_{\max}$. In this way, we obtain the simplest model for the n- Λ laser:

$$\begin{aligned} \frac{dI_p}{dt_{\parallel}} &= \kappa \left[-1 + \mathcal{L}_p \left(D - \frac{N_p}{2} \right) \right] I_p - \mathcal{L}_p \sum_{q \neq p} \frac{I_p I_q}{\gamma_{pq}} \left(D - \frac{N_p + N_q}{2} \right), \\ \frac{dD}{dt_{\parallel}} &= w - \left(1 + \sum_q I_q \right) D + \frac{1}{2} \sum_q I_q N_q, \\ \frac{dN_p}{dt_{\parallel}} &= - \left(1 + \sum_q I_q \right) N_p + I_p D. \end{aligned} \quad (5.26)$$

The enhancement of absorption induced by the low-frequency coherences is attested in the first equation of (5.26) by the minus sign before the sum.

5.3 Analysis of a two-transition laser

As in the study of the TSD⁺, we are forced to restrict our consideration to a specified number of modes if we want to go further in the analysis. The simplest case to study is a laser operating on two transitions. In the experiment reported on a microchip laser, this situation

was encountered with a pump power between 450 mW and 640 mW, while the laser first threshold was at 110 mW. We thus particularize Eqs. (5.26) to two modes. We simplify the problem further by assuming that $\mathcal{L}_1 = \mathcal{L}_2 = 1$. The antiphase nature of the periodic solution that emerges from the Hopf instability suggests the following change of variables

$$\begin{aligned} Y_1 &= I_1 + I_2, & Y_2 &= I_1 - I_2, \\ M_1 &= N_1 + N_2, & M_2 &= M_1 - M_2, \end{aligned} \quad (5.27)$$

in order to ease algebraic manipulations. Clearly, the variable Y_1 reflects the in-phase dynamics in the modal intensities, while Y_2 is related to antiphase dynamics. The same distinction applies to M_1 and M_2 . With these new variables, Eqs. (5.26) become

$$\frac{dD}{dt_{\parallel}} = w - (1 + Y_1)D + \frac{M_1 Y_1 + M_2 Y_2}{4}, \quad (5.28)$$

$$\frac{dM_1}{dt_{\parallel}} = -(1 + Y_1)M_1 + Y_1 D, \quad (5.29)$$

$$\frac{dM_2}{dt_{\parallel}} = -(1 + Y_1)M_2 + Y_2 D, \quad (5.30)$$

$$\frac{dY_1}{dt_{\parallel}} = \kappa \left[Y_1 (D - 1) - \frac{M_1 Y_1 + M_2 Y_2}{4} \right] - \frac{Y_1^2 - Y_2^2}{2\gamma} \left(D - \frac{M_1}{2} \right), \quad (5.31)$$

$$\frac{dY_2}{dt_{\parallel}} = \kappa \left[Y_2 (D - 1) - \frac{M_1 Y_2 + M_2 Y_1}{4} \right]. \quad (5.32)$$

The steady state solution corresponding to multimode solution is given by $Y_1 = Y_{1S}$, $Y_2 = 0$. In the limit $\kappa \rightarrow \infty$, the instability condition (5.24) is equivalent to $Y_{1S} = Y_H$ with

$$Y_H = \frac{7\gamma - 2 \pm \sqrt{4 - 12\gamma + \gamma^2}}{2(1 - 3\gamma)}. \quad (5.33)$$

This solution is physically acceptable only if it is positive, which imposes to choose the plus sign in (5.33). In addition, γ should be less than $1/3$, in agreement with (5.25).

At the Hopf bifurcation point, the frequency of the periodic solution is Ω_L (5.23). In order to construct this solution, we define a bifurcation parameter λ by $Y_{1S} = Y_H + \varepsilon^2 \lambda$, where $\varepsilon = \kappa^{-1/2}$. As λ is increased beyond the bifurcation point a periodic solution emerges with increasing amplitude. Since the oscillations are in antiphase, we seek a periodic solution that has the following scaling in the field variables:

$$Y_1(t_{\parallel}) = Y_H + \varepsilon^2 \lambda + \varepsilon^2 y_2^{(1)}(s, \tau, \sigma) + \dots, \quad (5.34)$$

$$Y_2(t_{\parallel}) = \varepsilon y_1^{(1)}(s, \tau, \sigma) + \varepsilon^2 y_2^{(2)}(s, \tau, \sigma) + \dots, \quad (5.35)$$

$$s = \varepsilon^{-1} \Omega_L t_{\parallel}, \quad \tau = \varepsilon \Omega_L t_{\parallel}, \quad \sigma = \varepsilon^2 t_{\parallel}. \quad (5.36)$$

In this expression we have defined the natural timescale of oscillation s and the two slower timescales τ and σ on which the envelope of the oscillations evolves. The fact that the amplitude of oscillations in the total intensity Y_1 is one order of magnitude smaller than in Y_2 is illustrated by the temporal timetrace in Fig. 5.2. The other variables are also expanded in powers of ε (see Appendix 5.A). By substitution of the perturbation expansion (5.34) and (5.35) into Eqs. (5.28) to (5.32), we find at the leading order that

$$y_1^{(1)}(s, \tau, \sigma) = \text{Re} [z(\tau, \sigma) e^{is}], \quad (5.37)$$

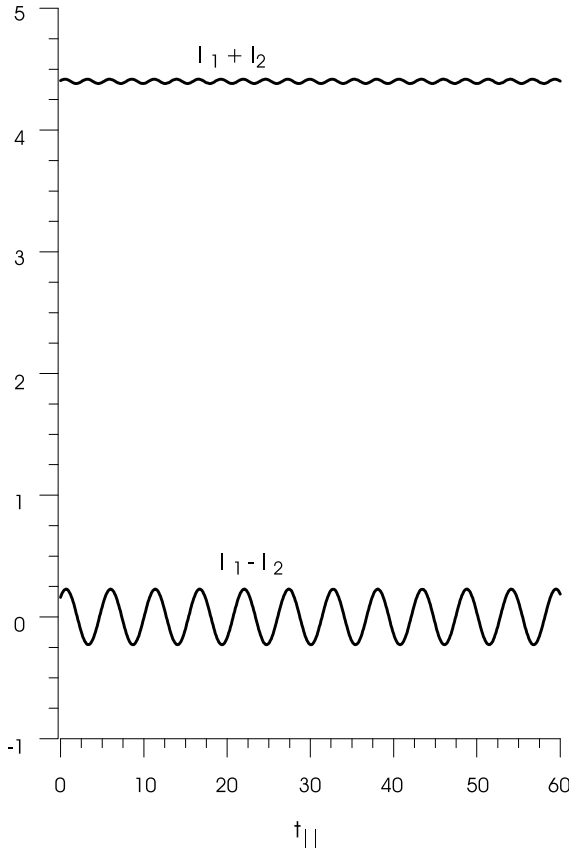


Figure 5.2: Temporal evolution of the total intensity and the difference between the modal intensities. Parameter values: $\varepsilon = 0.01$, $\gamma = 0.3$, $\mathcal{L}_1 = \mathcal{L}_2 = 1$, $Y_{1S} = 4.4$, which corresponds to $w \simeq 5.65$. The bifurcation point is $Y_H = 4$ ($w_H = 5.25$). While oscillations are well developed in the modal intensities, they are strongly attenuated in the total intensity.

where *c.c.* means “complex conjugate”. Using the method of multiple timescales, we find that $y_2^{(3)}(s, \tau, \sigma)$ remains bounded as s tends to infinity on condition that

$$\frac{\partial z}{\partial \tau} = iz(a_1 + a_2\lambda + a_3|z|^2), \quad (5.38)$$

where the a_i , given in Appendix 5.A, are real. This equation determines only partially the evolution of z . For a given amplitude of oscillations, the frequency of the solution is shifted from Ω_L by an amount $\varepsilon^2\Omega_L|z^{-1}\frac{\partial z}{\partial \tau}|$. However, the dependence of $|z|$ on the bifurcation parameter λ remains unspecified at this stage. This is done by considering the evolution of $y_2^{(4)}(s, \tau, \sigma)$. More specifically, we find that it remains bounded provided that

$$\frac{\partial z}{\partial \sigma} = z[b_1(\lambda - \lambda_H) - b_2|z|^2], \quad (5.39)$$

where the coefficients b_i , derived in Appendix 5.A, are real and positive. Equation (5.39) fixes the value of $|z|$ as a function of λ : it tends to $\sqrt{b_1(\lambda - \lambda_H)/b_2}$ as σ tends to infinity. Since both b_1 and b_2 are positive, the bifurcation is supercritical and the periodic solution is stable. This expression also contains a correction of order ε^2 to the position of the Hopf bifurcation

point: $Y_H \rightarrow Y_H + \varepsilon^2 \lambda_H + O(\varepsilon^4)$. Fig. 5.3 compares our theoretical prediction with the result of numerical integration of Eqs. (5.28) to (5.32) for $\gamma = 0.3$. The coefficient $\sqrt{b_1/b_2}$ is

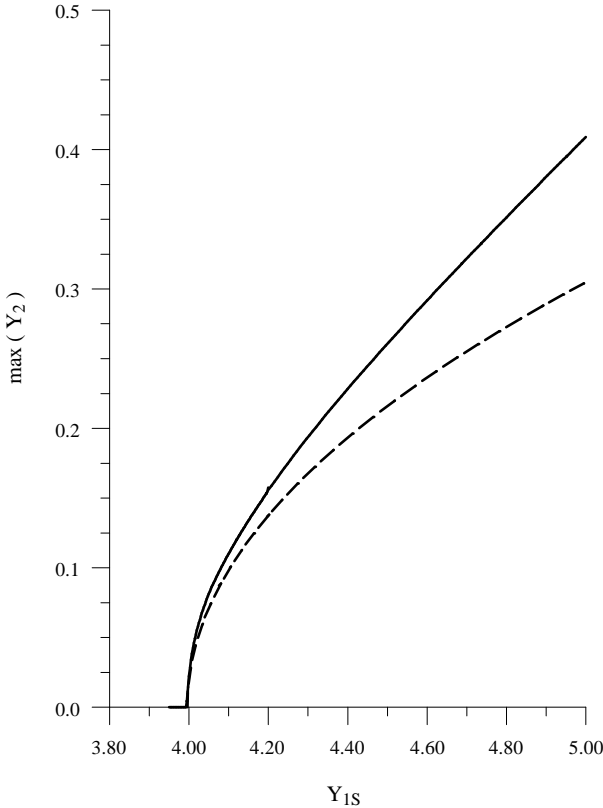


Figure 5.3: Bifurcation diagram showing the maxima of Y_2 versus Y_{1S} . Parameter values: $\varepsilon = 0.01$, $\gamma = 0.3$, $\mathcal{L}_1 = \mathcal{L}_2 = 1$. Full line: numerical integration of Eqs. (5.28) to (5.32). Broken line: analytical curve.

plotted as a function of γ in Fig. 5.4. We see that it vanishes for $\gamma = 3/14$. This value of γ corresponds to the situation $\Omega_R = 2\Omega_L$. Through this second order resonance, energy is transferred from the antiphase motion at frequency Ω_L to the attenuated mode of in-phase oscillations at frequency Ω_R . This suggests that a different perturbation scheme from the one used in Appendix 5.A could be more appropriate to study the laser dynamics for $\gamma \simeq 3/14$. However, numerical simulations in this region of parameters do not reveal any special feature in the dynamics.

5.4 Conclusion

A number of conclusions can now be drawn regarding the effect of low frequency atomic coherence on the laser dynamics if $\gamma_{||} \ll \Gamma_{pq} = O(\Gamma_c) \ll \gamma_{\perp}$ and if population differences can be approximated by the population in the highest level. The steady state field and population

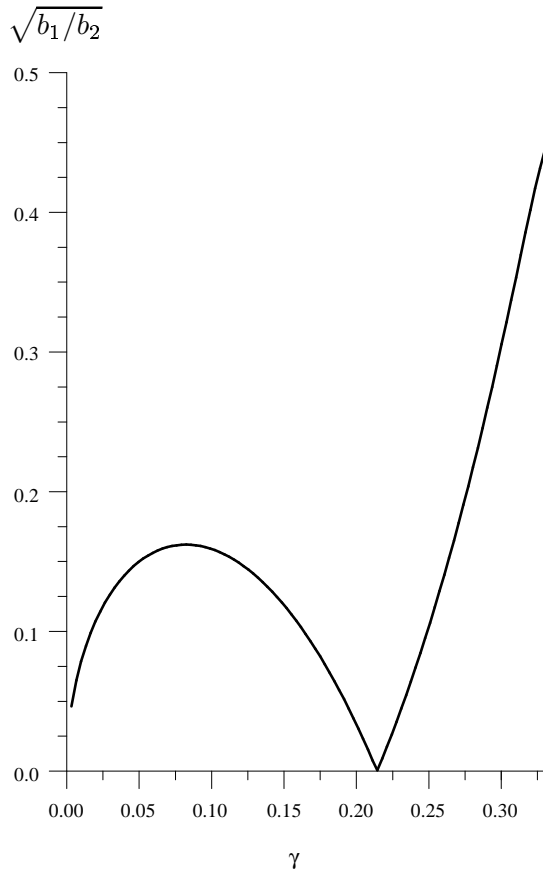


Figure 5.4: Coefficient $\sqrt{b_1/b_2}$ as a function of γ

variables are only slightly perturbed by the low frequency coherence. The corrections are $\mathcal{O}(\gamma_{\parallel}/\Gamma_{pq})$ compared with the TSD results. The simultaneous oscillation on different atomic transitions creates a coherence between the lower levels via a parametric interaction. After a time of the order of Γ_{pq}^{-1} , the amplitude and phase of the low frequency coherences S_{pq} reach their adiabatic states. The linear stability analysis indicates that it is valid to eliminate these atomic coherences adiabatically. This led us to derive the equations 5.26, which constitute a minimal generalization of the TSD model to describe quantum interference effect in the microchip LNP laser. These equations were recently used to explain experimental observations on an LNP laser with a KTP frequency-doubling crystal [18].

We have established that the coherence between the lowest atomic levels enhances the absorption via quantum interference. The sign in front of the new nonlinear term in Eq.(5.26) confirms this interpretation. Without this, stimulated emission stabilizes the laser steady state because any excess of intensity results in a diminution of the population inversion, and hence of the gain. However, the transient evolution towards steady state is not smooth. It consists of a large number of relaxation oscillations around the steady state because the escape rate of the photons from the cavity is large compared to the build-up rate of the population inversion ($\Gamma_c/\gamma_{\parallel} = \kappa \gg 1$). This feature is apparent in the linear stability analysis, which reveals

relaxation frequencies of the order of $\sqrt{\Gamma_c \gamma_{\parallel}}$ (Hz), i.e. large compared to the damping rate of order γ_{\parallel} . On the other hand, in this class of lasers, small population fluctuations typically give rise to $\sqrt{\Gamma_c / \gamma_{\parallel}}$ times larger intensity fluctuations [17]. Therefore, the stabilizing effect of stimulated emission is weak. In the presence of low frequency coherence it can even be suppressed by the enhancement of stimulated absorption. The balance between the two effects is at the origin of the instability condition $\lambda_{0,L} = 0$ in (5.24). A condition of the form $\gamma_{pq} = \Gamma_{pq}/\Gamma_c < \gamma_{\max}$ for the existence of a selfpulsing regime has been obtained. Otherwise, the low frequency coherence can never reach a sufficient level to significantly affect the absorption of the atoms. If the low frequency coherences vanish, the evolution equations (5.26) are the usual TSD rate equations whose steady state is stable above the lasing threshold [15]. This again indicates that the low frequency coherence is the source of the selfpulsing instability. Finally, the atomic coherence influences the amplification of the lasing modes only and therefore does not modify the lasing thresholds given by Eq. (5.21). In the particular case of a two-mode regime, we were able to construct the periodic solution in the neighborhood of the Hopf bifurcation and found that it is stable.

The closest experimental realization of this model is the microchip LNP laser studied by Otsuka et al. [10]. The cavity dimension ($L_c \simeq 1\text{mm}$) yields a particularly large value of Γ_c and realizes the important condition $\Gamma_{pq} = \mathcal{O}(\Gamma_c)$. In these experiments, the laser oscillates simultaneously on up to three atomic transitions. The central role played by atomic coherence was confirmed experimentally by comparing multimode regime on multiple and on single transitions. Self-pulsing behavior was observed in the former case whereas *cw* operation only was obtained in the latter case. Moreover, the experimental selfpulsing regime displayed antiphase dynamics as described in this theoretical work.

A completely different set of approximations for a similar energy level scheme was analyzed by Fu Hong and Haken [19] in an attempt to model some dye lasers. In their model, simultaneous oscillation on different transitions was not allowed. Furthermore, they considered the opposite limit in which the low frequency coherences were adiabatically eliminated while retaining the optical coherences. This set of approximations cannot be applied to the microchip LNP laser.

Appendix to Chapter 5

5.A Derivation of the amplitude equation

For a given value of the total intensity Y_{1S} the steady state is given by $Y_{2S} = M_{2S} = 0$ and

$$\begin{aligned} D_S &= \frac{4(1+Y_{1S})}{4 + 3Y_{1S} - \varepsilon^2 Y_{1S}(2+Y_{1S})/\gamma}, \\ M_{1S} &= \frac{Y_{1S}D_S}{1+Y_{1S}}, \\ w &= (1+Y_{1S})D_S - \frac{M_{1S}Y_{1S}}{4}, \end{aligned} \quad (5.40)$$

with $\varepsilon = \kappa^{-1/2}$. Close to the bifurcation, we write $Y_{1S} = Y_H + \varepsilon^2 \lambda$. Substituting this expression for Y_{1S} in (5.40) and expanding in powers of ε , we reexpress the steady state as

$$D_S(\varepsilon) = D_H + \varepsilon^2 D_S^{(2)} + \varepsilon^4 D_S^{(4)} + \dots, \quad (5.41)$$

$$M_{1S}(\varepsilon) = M_H + \varepsilon^2 M_{1S}^{(2)} + \varepsilon^4 M_{1S}^{(4)} + \dots, \quad (5.42)$$

$$w(\varepsilon) = w_0 + \varepsilon^2 w^{(2)} + \varepsilon^4 w^{(4)} + \dots \quad (5.43)$$

To describe antiphase oscillations, we seek a small amplitude periodic solution of the form

$$Y_2 = \varepsilon y_2^{(1)}(s, \tau, \sigma) + \varepsilon^2 y_2^{(2)}(s, \tau, \sigma) + \dots, \quad (5.44)$$

$$M_2 = \varepsilon^2 m_2^{(1)}(s, \tau, \sigma) + \varepsilon^3 m_2^{(2)}(s, \tau, \sigma) + \dots \quad (5.45)$$

In this expansion, we treat the time variables s , τ , and σ as if they were independent. This amounts to apply the chain rule

$$\frac{d}{dt_{\parallel}} \rightarrow \varepsilon^{-1} \Omega_L \frac{\partial}{\partial s} + \varepsilon \Omega_L \frac{\partial}{\partial \tau} + \varepsilon^2 \frac{\partial}{\partial \sigma}. \quad (5.46)$$

On the other hand, oscillations associated to D , M_1 , and Y_1 are one order of magnitude smaller because they correspond to in-phase dynamics. For these variables, we therefore use the perturbation expansion

$$Y_1 = Y_H + \varepsilon^2 \lambda + \varepsilon^2 y_1^{(1)}(s, \tau, \sigma) + \varepsilon^3 y_1^{(2)}(s, \tau, \sigma) + \dots, \quad (5.47)$$

$$M_1 = M_{1S}(\varepsilon) + \varepsilon^3 m_1^{(1)}(s, \tau, \sigma) + \varepsilon^4 m_1^{(2)}(s, \tau, \sigma) + \dots, \quad (5.48)$$

$$D = D_S(\varepsilon) + \varepsilon^3 d^{(1)}(s, \tau, \sigma) + \varepsilon^4 d^{(2)}(s, \tau, \sigma) + \dots \quad (5.49)$$

Substituting these perturbation expansions in the system (5.28)-(5.32), and collecting like powers of ε , we get a sequence of linear problems to solve. The leading order problem is

$$\left(\Omega_L \frac{\partial}{\partial s} - \mathcal{A} \right) \begin{pmatrix} m_2^{(1)} \\ y_2^{(1)} \end{pmatrix} = 0, \quad \mathcal{A} = \begin{pmatrix} 0 & D_H \\ -\frac{1}{4}Y_H & 0 \end{pmatrix}. \quad (5.50)$$

Its solution is

$$\begin{pmatrix} m_2^{(1)} \\ y_2^{(1)} \end{pmatrix} = \frac{z(\tau, \sigma) e^{is}}{2} \vec{v}_L + c.c., \quad \vec{v}_L = \begin{pmatrix} -i4\Omega_L/Y_H \\ 1 \end{pmatrix}. \quad (5.51)$$

Above, \vec{v}_L is the eigenvector of \mathcal{A} associated to the eigenvalue Ω_L . In order to evaluate solvability conditions in subsequent developments, we will need to use the expression of the adjoint eigenvector, $\vec{w}_L = (iY_H/(4\Omega_L), 1)$. It is solution to the adjoint eigenvalue problem $\vec{w}_L \cdot \mathcal{A} = i\Omega_L \vec{w}_L$.

At the next order, solution (5.51) is used to evaluate the inhomogeneous term in the two following problems:

$$\left(\Omega \frac{\partial}{\partial s} - \mathcal{B} \right) \begin{pmatrix} d^{(1)} \\ m_1^{(1)} \\ y_1^{(1)} \end{pmatrix} = \mathcal{R}_1, \quad \left(\Omega \frac{\partial}{\partial s} - \mathcal{A} \right) \begin{pmatrix} m_2^{(2)} \\ y_2^{(2)} \end{pmatrix} = \mathcal{R}_2, \quad (5.52)$$

where

$$\begin{aligned} \mathcal{B} &= \begin{pmatrix} 0 & 0 & -1 \\ 0 & 0 & D_H - M_H \\ Y_H & -\frac{1}{4}Y_H & 0 \end{pmatrix}, \quad \mathcal{R}_1 = \begin{pmatrix} 0 \\ 0 \\ -\frac{1}{4}m_2^{(1)}y_2^{(1)} \end{pmatrix}, \\ \mathcal{R}_2 &= \begin{pmatrix} -(1+Y_H)m_2^{(1)} \\ (D_S^{(2)} - \frac{1}{4}M_{1S}^{(2)})y_2^{(1)} \end{pmatrix}. \end{aligned}$$

The right hand side \mathcal{R}_2 is periodic with frequency 1 (on the rescaled time s). It causes therefore a secular divergence of $m_2^{(2)}$ and $y_2^{(2)}$, unless $\int_0^{2\pi} \vec{w}_L \cdot \mathcal{R}_2 e^{-is} ds = 0$, which is precisely the Hopf condition (5.33). The solutions of the problems (5.52) are

$$\begin{pmatrix} d^{(1)}, & m_1^{(1)}, & y_1^{(1)} \end{pmatrix} = \frac{(1+Y_H)ze^{is}}{4(Y_H-1)Y_H\Omega_L} \left(i, \frac{-i}{4+3Y_H}, 2\Omega_L \right) + c.c., \quad (5.53)$$

$$\begin{pmatrix} m_2^{(2)}, & y_2^{(2)} \end{pmatrix} = \frac{(1+Y_H)ze^{is}}{Y_H\Omega_L} \left(\Omega_L, \frac{-i}{4}Y_H \right) + c.c. \quad (5.54)$$

With this, we can compute the right hand sides in the two next problems. They are

$$\left(\Omega \frac{\partial}{\partial s} - \mathcal{B} \right) \begin{pmatrix} d^{(2)} \\ m_1^{(2)} \\ y_1^{(2)} \end{pmatrix} = \mathcal{R}_3, \quad \left(\Omega \frac{\partial}{\partial s} - \mathcal{A} \right) \begin{pmatrix} m_2^{(3)} \\ y_2^{(3)} \end{pmatrix} = \mathcal{R}_4, \quad (5.55)$$

with

$$\mathcal{R}_3 = \begin{pmatrix} -(1+Y_H)d^{(1)} + \frac{1}{4}Y_Hm_1^{(1)} + \frac{1}{4}m_2^{(1)}y_2^{(1)} \\ Y_Hd^{(1)} - (1+Y_H)m_1^{(1)} \\ -(1+Y_H)y_1^{(1)} - \frac{1}{4}m_2^{(2)}y_2^{(1)} + \frac{1}{4}m_2^{(1)}y_2^{(2)} + \frac{1+Y_H}{Y_H}y_2^{(1)2} \end{pmatrix}, \quad (5.56)$$

$$\begin{aligned}\mathcal{R}_4 &= -\Omega \frac{\partial}{\partial \tau} \begin{pmatrix} m_2^{(1)} \\ y_2^{(1)} \end{pmatrix} \\ &\quad + \begin{pmatrix} -(1+Y_H)m_2^{(2)} + D_S y_2^{(1)} \\ -\frac{1}{4}m_2^{(1)}(\lambda + y_1^{(1)}) + (d^{(1)} - \frac{1}{4}m_1^{(1)})y_2^{(1)} + (1+Y_H)y_2^{(2)} \end{pmatrix}. \end{aligned} \quad (5.57)$$

Here again, \mathcal{R}_4 is susceptible to lead to a secular divergence in $m_2^{(3)}$ and $y_2^{(3)}$. To avoid this fact, we require that $\int_0^{2\pi} \hat{w}_L \mathcal{R}_4 e^{-is} ds = 0$, which yields

$$\frac{\partial z}{\partial \tau} = iz(a_1 + a_2\lambda + a_2|z|^2), \quad (5.58)$$

with the coefficients

$$a_1 = -\frac{(2+Y_H)(1+Y_H)}{Y_H}, \quad (5.59)$$

$$a_2 = \frac{(2+Y_H)(2+3Y_H)}{2Y_H(1+Y_H)(4+3Y_H)}, \quad (5.60)$$

$$a_3 = \frac{(3+Y_H)}{8(Y_H-1)Y_H}. \quad (5.61)$$

Once condition (5.58) is satisfied, the solutions of the problem (5.55) are, on the one hand,

$$d^{(2)} = -\frac{160+392Y_H+324Y_H^2+97Y_H^3}{32(Y_H-1)^2Y_H}z^2e^{2is} + c.c., \quad (5.62)$$

$$m_1^{(2)} = \frac{40+Y_H(8+Y_H)(8+3Y_H)}{8(Y_H-1)^2Y_H}z^2e^{2is} + c.c., \quad (5.63)$$

$$y_1^{(2)} = \frac{i(1+Y_H)[44+Y_H(68+27Y_H)]}{16(Y_H-1)^2Y_H\Omega_L}z^2e^{2is} + c.c., \quad (5.64)$$

and, on the other hand,

$$\begin{aligned}m_2^{(3)} &= \frac{i\Omega_L}{2} \left[\frac{4+6Y_H+3Y_H^2}{Y_H(1+Y_H)(4+3Y_H)}\lambda - 1 - Y_H + \frac{(3+Y_H)|z|^2}{4(Y_H-1)Y_H} \right]ze^{is} \\ &\quad - \frac{i\Omega_L(7+5Y_H)}{16(Y_H-1)Y_H}z^3e^{3is} + c.c.,\end{aligned} \quad (5.65)$$

$$\begin{aligned}y_2^{(3)} &= \frac{1}{8} \left[\frac{4+6Y_H+3Y_H^2}{Y_H(1+Y_H)(4+3Y_H)}\lambda - 1 - Y_H + \frac{(3+Y_H)|z|^2}{4(Y_H-1)Y_H} \right]ze^{is} \\ &\quad + \frac{3(7+5Y_H)}{64(Y_H-1)Y_H}z^3e^{3is} + c.c.\end{aligned} \quad (5.66)$$

Finally, $m_2^{(4)}$ and $y_2^{(4)}$ obey the following equation:

$$\left(\Omega \frac{\partial}{\partial s} - \mathcal{A} \right) \begin{pmatrix} m_2^{(4)} \\ y_2^{(4)} \end{pmatrix} = \mathcal{R}_5, \quad (5.67)$$

where

$$\mathcal{R}_5 = -\Omega \frac{\partial}{\partial \tau} \begin{pmatrix} m_2^{(2)} \\ y_2^{(2)} \end{pmatrix} - \frac{\partial}{\partial \sigma} \begin{pmatrix} m_2^{(1)} \\ y_2^{(1)} \end{pmatrix} + \mathcal{R}'_5, \quad (5.68)$$

$$\begin{aligned}\mathcal{R}'_5 &= \begin{pmatrix} -(1+Y_H)m_2^{(3)} - m_2^{(1)}(\lambda + y_1^{(1)}) \\ -m_2^{(2)\frac{\lambda+y_1^{(1)}}{4}} - m_2^{(1)}y_1^{(2)} + \left(D_S^{(4)} + d^{(2)} - \frac{M_{1S}^4 + m_1^{(2)}}{4}\right)y_2^{(1)} \end{pmatrix} \\ &\quad + \begin{pmatrix} d^{(1)}y_2^{(1)} + D_S^{(2)}y_2^{(2)} \\ d^{(1)}y_2^{(2)} - \frac{m_1^{(1)}y_2^{(2)}}{4} + (1+Y_H)y_2^{(3)} \end{pmatrix},\end{aligned}\tag{5.69}$$

and secular divergence is avoided, provided that $\int_0^{2\pi} \vec{w}_L \cdot \mathcal{R}_5 e^{-is} ds = 0$. We thus obtain

$$\frac{\partial z}{\partial \sigma} = z [b_1(\lambda - \lambda_H) - b_2|z|^2],\tag{5.70}$$

with the coefficients

$$b_1 = \frac{8 + 8Y_H + Y_H}{2Y_H(2 + Y_H)(4 + 3Y_H)},\tag{5.71}$$

$$b_2 = \frac{24 + Y_H(56 + 46Y_H + 13Y_H^2)}{16(Y_H - 1)^2 Y_H},\tag{5.72}$$

$$\lambda_H = -\frac{Y_H(2 + Y_H)(4 + 3Y_H)(1 + Y_H)^2}{8 + 8Y_H + Y_H}.\tag{5.73}$$

Since Y_H must be positive, we immediately see that b_1 and b_2 are positive too, which proves the stability of the emerging periodic solution.

References

- [1] O. Kocharovskaya, Phys. Rep. **219**, 175 (1992).
- [2] P. Mandel, Contemporary Physics **34**, 235 (1993).
- [3] M.O. Scully, Quantum & Semiclassical Opt. **6**, 203 (1994).
- [4] E. Arimondo, in *Progress in Optics*, E. Wolf ed., Elsevier Science, Amsterdam (1996), p.257.
- [5] S.E. Harris, Physics Today, July 1997, p.36.
- [6] O. Kocharovskaya and Ya. I. Khanin, Pis'ma Zh. Eksp. Teor. Fiz. **48**, 581 (1988) [JETP Lett. **48**, 630 (1988)].
- [7] S.E. Harris, Phys. Rev. Lett. **62**, 1033 (1989).
- [8] M.O. Scully, S.-Y. Zhu, and A. Gavrielides, Phys. Rev. Lett. **62**, 2813 (1989).
- [9] K. Otsuka, P. Mandel, and E.V. Viktorov, Phys. Rev. A **56**, 3226 (1997).
- [10] K. Otsuka, E.A. Viktorov, and P. Mandel, EuroPhys. Lett. **45**, 307 (1999).
- [11] K.Otsuka, R. Kawai, Y. Asakawa, P. Mandel, and E.A. Viktorov, Opt. Lett. **23**, 201 (1998).
- [12] A. E. Siegman, *Lasers* (University Sciences Books, 1986), p. 36.
- [13] G. Kozyreff and P. Mandel, Phys. Rev. A **61**, 033813 (2000).
- [14] W. Koechner, *Solid-state laser engineering*, fourth edition (Springer, Heidelberg, 1996).
- [15] C.L. Tang, H. Statz, and G. deMars, J. Appl. Phys. **34**, 2289 (1963).
- [16] P. Mandel 1997 *Theoretical Problems in Cavity Nonlinear Optics* (Cambridge: Cambridge University Press).
- [17] D. Pieroux, Ph. D. Thesis: *Contribution à la dynamique des lasers multimodes et des lasers contrôlés par rétroaction*, Université Libre de Bruxelles, 1997.
- [18] K. Otsuka, J.-Y. Ko, S.-I. Higashihara, and J.-L. Chern, Opt. Lett. **26**, 536 (2001).
- [19] Hong Fu and H. Haken, Phys. Rev. A **36**, 4802 (1987).

Chapter 6

Inversionless amplification and propagation in an electro-nuclear level-mixing scheme

6.1 Introduction

The hope to realize laser amplification on nuclear transitions is at the origin of much theoretical and experimental research (see the recent reviews [1, 2]). The main difficulty that arises in this context is the technical impossibility to create an inversion of population between adequate pairs of levels. To explain this, the frequency dependence of the spontaneous emission rate is usually put forward. Indeed, for a transition with frequency ω and dipolar moment μ , it is given by the Einstein coefficient:

$$A = \frac{\omega^3}{3\pi\varepsilon_0\hbar c^3} |\mu|^2.$$

Therefore, as we increase the frequency of the laser transition, it becomes harder to realize the necessary population inversion. As in [2], though, we note that the value of the dipole moment should also be taken into account so that, in general, the statement that a larger spontaneous emission rate corresponds to a larger frequency is not true. It is a fact, however, that no electromagnetic source is available to pump efficiently nuclear transitions and realize a gamma laser in the traditional way.

In principle, this obstacle can be overcome by exploiting quantum interference. Amplification without population inversion (AWI) was predicted [3, 4, 5] and demonstrated experimentally [6, 7, 8, 9, 10, 11, 12, 13] on atomic transitions. For application of these ideas to gamma optics, it was proposed to couple a radio-frequency electromagnetic field with the Hyperfine levels of a nuclear ground state in order to create the necessary quantum coherence [14]. However, it was later realized that, due to the equal population of all Hyperfine levels for a sample at room temperature, this coherence cannot be achieved [15], so that the extension of the principles of atomic AWI to nuclear transitions remains problematic. In response to this problem, we discuss an electro-nuclear scheme where atomic and nuclear transitions are coupled by the Hyperfine interaction. Two electromagnetic fields, one optical and the other in the gamma range, interact with this system. It involves Mössbauer nuclei, i.e., nuclei that emit or absorb electromagnetic radiation without recoil [16]. Another

proposition to create nuclear coherence in Mössbauer nuclei was given in [17]. We show that it is possible to cancel the absorption of gamma radiation by preparing the nuclei into an appropriate superposition of the lowest levels. In this case, any population in the nuclei excited state is sufficient to amplify the gamma field by stimulated emission, which leads to AWI. This quantum preparation can be done through the coherent excitation of the atomic transition by the optical field.

After having established the possibility of AWI of a gamma field in the continuous wave regime, we note that part of the optical field energy is dissipated in this process. Therefore, the quality of AWI is altered in the course of propagation. This leads us to estimate the optimal length of amplification as a function of the input drive field intensity and the rate of incoherent excitation. Beyond this length, the amplifying medium turns into an absorbing medium, which makes this point a crucial piece of information to set up an experiment. In [18], a similar study was done for a V-scheme in rubidium, with special attention to Doppler broadening in vapor cells.

Because a high optical field amplitude is favorable to AWI, it is natural to expect that an optical pulse can only improve the amplification. Indeed, short pulses provide high peak intensity. We therefore reconsider propagation in this situation. Two types of pulses are identified, depending on their duration relative to the other characteristic times of the system. Specifically, we use the terms “adiabatic pulse” if the polarization variables can be eliminated adiabatically on the pulse time scale and “ultrashort pulse” otherwise. In the former case, the mechanism of AWI is basically the same as for the continuous wave regime. In the latter case, AWI rests on a different mechanism, namely the creation of a temporal window of inversion on the gamma transition through Rabi oscillations. Throughout this study, we assume that the gamma field is weak in the sense that it perturbs negligibly the quantum populations. Our theory is therefore linear in the gamma field, while nonlinear in the optical field.

This chapter is organized as follows. In Sec. 6.2, we introduce the electro-nuclear system and present the model equations. We then analyze successively the inversionless amplification of continuous waves, adiabatic pulses and ultrashort pulses in sections 6.3 to 6.5. Finally, we conclude.

The results presented in this chapter were published in [19, 20].

6.2 The level Mixing scheme

In general, a nucleus that emits a gamma photon experiences a recoil, which broadens the emission line. This has the effect of reducing the nuclear resonant cross sections. In solids, some nuclei, called Mössbauer nuclei, depart from this rule, as their recoil is absorbed by the lattice vibrations. This makes them the best candidates for gamma-ray lasers. Following the proposition in [14], let us consider a density \mathcal{N} of such nuclei in a noncubic uniaxial crystal. The ionic arrangement associated to the symmetry of the crystal induces a static electric field gradient parallel to the c-axis. Moreover, any nucleus generally possesses some ellipticity, characterized by the quadrupole moment. The interaction of the quadrupole moment with this gradient lifts some degeneracies among the nuclear levels. Specifically, if the ground state of the nucleus is a multiplet $I = 3/2$, it is split by the quadrupole interaction into the degenerate doublets $M_I = \pm 1/2$ and $M_I = \pm 3/2$ (see Fig. 6.1).

In the system we consider, a magnetic field \mathbf{H}_z is applied parallel to the c-axis. Due to the

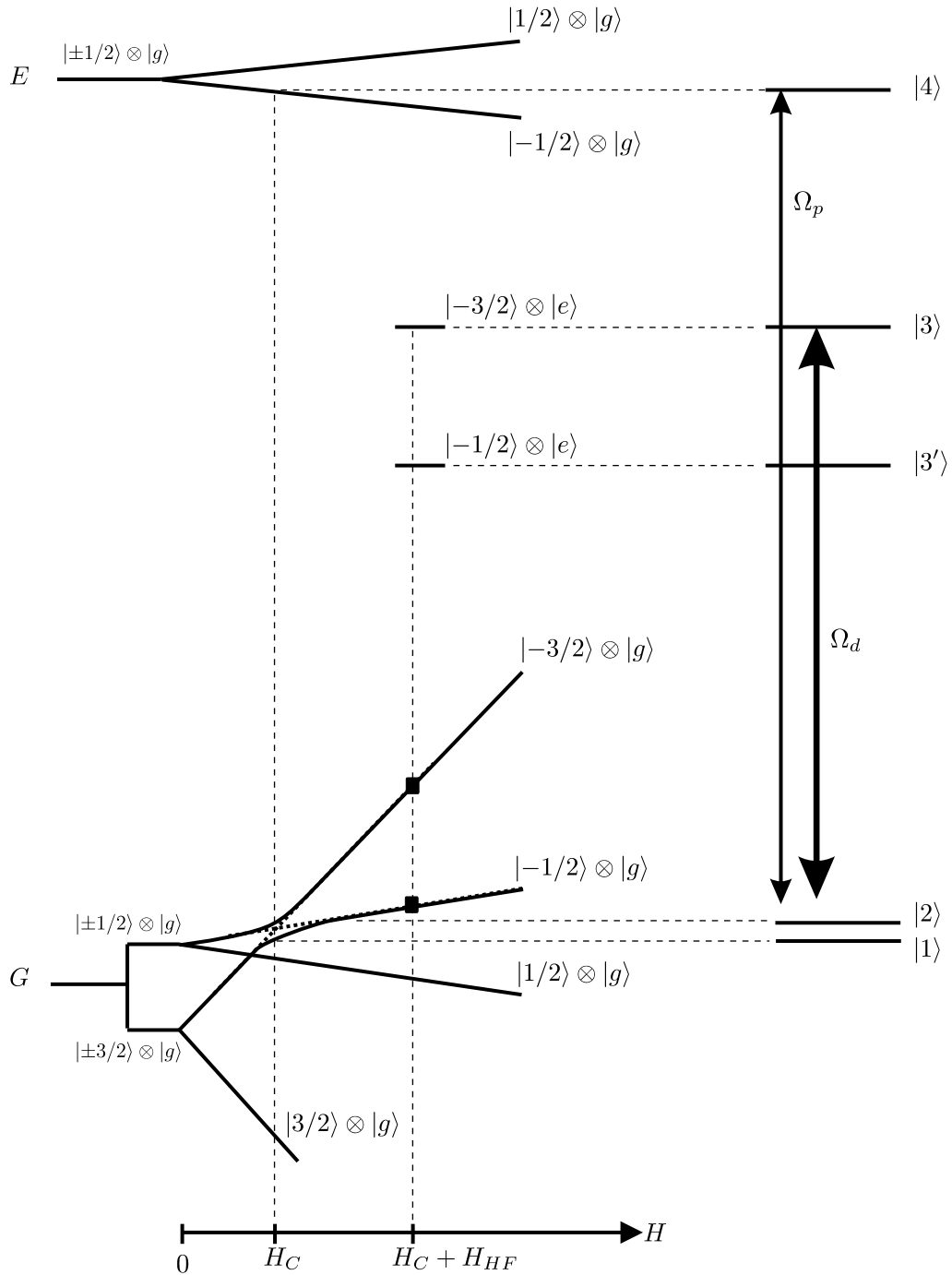


Figure 6.1: Energy diagram of the nucleus interacting with the gamma-probe and laser-pump. G and E (g and e) denote the ground and excited nuclear (atomic) state, respectively. H is the static magnetic field experienced by the nucleus in the c-direction. At $H = 0$, the ground nuclear state is split by the interaction of the quadrupolar moment with the static electric field gradient. Level mixing occurs at $H = H_C$. Due to the transverse magnetic field H_\perp , the levels do not cross but repel each others. If the electron shell is excited, the local magnetic field differs from H_C by the Hyperfine field H_{HF} . The diagram is not to scale: $\epsilon_2 - \epsilon_1 \ll \epsilon_3 - \epsilon_3' \ll \epsilon_3 - \epsilon_1 \ll \epsilon_4 - \epsilon_1$.

Zeeman effect and the quadrupole interaction, there exists a critical field $\mathbf{H}_z = \mathbf{H}_C$ for which the ground levels $|G, -1/2\rangle$ and $|G, -3/2\rangle$ coincide (see Fig. 6.1). If one adds to \mathbf{H}_z a transverse component \mathbf{H}_\perp , then the circular symmetry of the system is broken and the degeneracy is removed. The eigenstates of the perturbed hamiltonian are, in first approximation, of the form

$$|1\rangle = (S_1 |G, -3/2\rangle + S_2 |G, -1/2\rangle) \otimes |g\rangle, \quad (6.1)$$

$$|2\rangle = (S_2 |G, -3/2\rangle - S_1 |G, -1/2\rangle) \otimes |g\rangle. \quad (6.2)$$

In these expression the second part $|g\rangle$ of the tensorial products refers to the ground state of the electron shell. In the nucleus part, $|G, -1/2\rangle$ and $|G, -3/2\rangle$ are mixed. The corresponding coefficients S_1 and S_2 are experimental parameters that are adjustable via \mathbf{H}_\perp . This level mixing is useful for spectroscopy because it modifies the angular distribution of radiations emitted by the nucleus. By examining this angular distribution, experimentalists can thus detect the level crossing and, via \mathbf{H}_z , deduce the initial splitting due to the quadrupole interaction [21].

The excited state of the nucleus is chosen to have a total nuclear spin number $I = 1/2$ and the associated magnetic number $M_I = -1/2$. We label it

$$|4\rangle = |E, -1/2\rangle \otimes |g\rangle. \quad (6.3)$$

Gamma photons propagating parallel to the c-axis have a polarization transverse to the direction of quantization and can therefore induce transitions only with $\Delta M_I = \pm 1$. Thanks to the level mixing produced by the transverse magnetic field \mathbf{H}_\perp , both $1 \leftrightarrow 4$ and $2 \leftrightarrow 4$ transitions are allowed by the selection rules.

Let us now consider the atomic excitation. In its excited state, the electron shell has a different orbital angular momentum than in its ground state. Therefore, for an applied magnetic field $\mathbf{H}_z = \mathbf{H}_C$ the magnetic field felt by the nucleus in the direction of quantification generally differs from \mathbf{H}_C . As a result, the possible excited states are (See Fig. 6.1)

$$|3\rangle = |G, -3/2\rangle \otimes |e\rangle, \quad (6.4)$$

$$|3'\rangle = |G, -1/2\rangle \otimes |e\rangle, \quad (6.5)$$

where “e” stands for “excited”. Let us stress that, in the absence of this Hyperfine interaction, the optically excited states would be

$$(S_1 |G, -3/2\rangle + S_2 |G, -1/2\rangle) \otimes |e\rangle,$$

and

$$(S_2 |G, -3/2\rangle - S_1 |G, -1/2\rangle) \otimes |e\rangle,$$

so that nucleus and electron shell would be uncoupled. By estimating the potential energy of the nuclear magnetic moment in the magnetic field created by the electron shell, the energy difference between states $|3\rangle$ and $|3'\rangle$ is of the order of [22].

$$\epsilon_3 - \epsilon_{3'} \sim \frac{e^2 \hbar^2}{m_e m_p c^2 a_0^3} \sim 10^{-6} \text{eV} \gg \epsilon_2 - \epsilon_1. \quad (6.6)$$

In this expression, m_e is the mass of the electron, m_p is the mass of the proton, and a_0 is the Bohr radius. To be distinguishable, the transitions $1 \leftrightarrow 3$ and $1 \leftrightarrow 3'$ should therefore be narrower than $(\epsilon_3 - \epsilon_{3'})/\hbar \sim 10^9 \text{ s}^{-1}$. Such spectral narrowness requires to reduce significantly the phonon broadening. This situation can be approached at the liquid nitrogen temperature [23]. Thanks to the Hyperfine interaction, one can thus isolates levels $|1\rangle$, $|2\rangle$, $|3\rangle$, and $|4\rangle$ from the rest of the spectrum. These states constitute our electro-nuclear model.

We complete this system by the addition of a resonant bichromatic field

$$E(z, t) = E_d e^{i(\omega_d t - k_d z)} + E_p e^{i(\omega_p t - k_p z)} + c.c., \quad (6.7)$$

where “c.c.” means “complex conjugate”. The optical field E_d is nearly resonant with the $1 \leftrightarrow 3$ and $2 \leftrightarrow 3$ transitions. Hereafter, we call it the “drive field”. The other spectral component, E_p , is coupled to the nuclear transitions $1 \leftrightarrow 4$ and $2 \leftrightarrow 4$. We call it the “probe field”. The drive and probe transitions are characterized by the dipole matrix elements μ_d and μ_p , respectively. To treat the interaction between $E(z, t)$ and the medium, it is useful to express the spectral components of the electric field in terms of the Rabi frequencies

$$\Omega_d \equiv \frac{\mu_d E_d}{\hbar}, \quad \Omega_p \equiv \frac{\mu_p E_p}{\hbar}. \quad (6.8)$$

Ω_d is the frequency associated to the energy of interaction between the optical dipole and the drive field, while Ω_p corresponds to the potential energy of the nuclear dipole in the probe electric field. On the other hand, with Γ_d and Γ_p denoting the drive and probe polarization decay rates, the intensities are most conveniently described by the two stimulated transition rates

$$J_d \equiv \frac{|\Omega_d|^2}{\Gamma_d}, \quad J_p \equiv \frac{|\Omega_p|^2}{\Gamma_p}. \quad (6.9)$$

Let us now examine the evolution equations of the matter and field variables. In the rotating wave and slowly varying envelope approximations, the spatio-temporal evolution of the two fields is governed by the wave equations

$$\left(\frac{\partial}{\partial z} + \frac{n_p}{c} \frac{\partial}{\partial t} \right) \Omega_p = -i \frac{\mathcal{N} \omega_p |\mu_p|^2}{2 \varepsilon_0 \hbar n_p c} P_p, \quad (6.10)$$

$$\left(\frac{\partial}{\partial z} + \frac{n_d}{c} \frac{\partial}{\partial t} \right) \Omega_d = -i \frac{\mathcal{N} \omega_d |\mu_d|^2}{2 \varepsilon_0 \hbar n_d c} P_d. \quad (6.11)$$

In these, $P_{d,p}$ are the microscopic polarizations rescaled to the dipole matrix elements, and $n_{p,d}$ are the refractive indices at the two frequencies ω_p and ω_d . Furthermore, the Hamiltonian of interaction between the electromagnetic field and the atom is, in the dipole approximation, $\mathcal{H}_{int} = -\mu E$, where we have noted the dipole operator μ to avoid confusion with the subscript “ d ” of the drive field. With this Hamiltonian, the equations for the fields are completed by

Table 6.1: List of parameter values

symbol	signification	value
Γ_d	relaxation rate of P_d	$3.0 \cdot 10^9 s^{-1}$
Γ_p	relaxation rate of P_p	$10^6 s^{-1}$
$2\gamma_d$	relaxation rate of ρ_{33}	$10^3 s^{-1}$
$2\gamma_p$	relaxation rate of ρ_{44}	$10^6 s^{-1}$
$2R$	incoherent excitation of ρ_{44}	$< 10^6 s^{-1}$
Γ_{12}	relaxation rate of ρ_{12}	$150 s^{-1}$
ω_{21}	frequency separation between $ 1\rangle$ and $ 2\rangle$	$10^3 s^{-1}$
Γ_{34}	relaxation rate of σ_{34}	$3.0 \cdot 10^9 s^{-1}$

the semiclassical density matrix equations

$$P_d = S_1\sigma_{13} + S_2\sigma_{23}, \quad P_p = S_1\sigma_{14} + S_2\sigma_{24}, \quad (6.12)$$

$$\frac{\partial \rho_{\eta\eta}}{\partial t} = -R\rho_{\eta\eta} + \gamma_p\rho_{44} + \gamma_d\rho_{33} + iS_\eta(\Omega_p\sigma_{4\eta} + \Omega_d\sigma_{3\eta} - c.c.), \quad (6.13)$$

$$\frac{\partial \rho_{33}}{\partial t} = -2\gamma_d\rho_{33} - i(\Omega_d P_d^* - c.c.), \quad (6.14)$$

$$\frac{\partial \rho_{44}}{\partial t} = -2\gamma_p\rho_{44} + R \sum_{\eta=1,2} \rho_{\eta\eta} - i(\Omega_p P_p^* - c.c.), \quad (6.15)$$

$$\frac{\partial \rho_{\eta\eta'}}{\partial t} = -(\Gamma_{12} + i\omega_{\eta\eta'})\rho_{\eta\eta'} + iS_\eta(\Omega_p\sigma_{4\eta'} + \Omega_d\sigma_{3\eta'}) - iS_{\eta'}(\Omega_p\sigma_{4\eta} + \Omega_d\sigma_{3\eta})^*, \quad (6.16)$$

$$\frac{\partial \sigma_{3\eta}}{\partial t} = -(\Gamma_d + i\delta_\eta)\sigma_{3\eta} + i\Omega_d^*(S_\eta n_{\eta 3} + S_{\eta'}\rho_{\eta'\eta}) - iS_\eta\Omega_p^*\sigma_{34}, \quad (6.17)$$

$$\frac{\partial \sigma_{4\eta}}{\partial t} = -(\Gamma_p + i\Delta_\eta)\sigma_{4\eta} + i\Omega_p^*(S_\eta n_{\eta 4} + S_{\eta'}\rho_{\eta'\eta}) - iS_\eta\Omega_d^*\sigma_{43}, \quad (6.18)$$

$$\frac{\partial \sigma_{34}}{\partial t} = -[\Gamma_{43} + i(\delta_1 - \Delta_1)]\sigma_{34} + i(\Omega_d^*P_p - \Omega_p P_d^*). \quad (6.19)$$

In these equations, we have noted $n_{ij} = \rho_{ii} - \rho_{jj}$. The indices η and η' designate the ground state 1 or 2 with $\eta \neq \eta'$. R quantifies the incoherent pumping rate of state $|4\rangle$ starting from the ground states $|1\rangle$ and $|2\rangle$. Conversely, γ_d and γ_p are spontaneous decay rates of the excited levels. An important parameter in the present analysis is the ratio

$$r \equiv \frac{R}{\gamma_p}. \quad (6.20)$$

$r < 1$ means that there is no population inversion between level $|4\rangle$ and the ground levels. As already mentioned, Γ_d and Γ_p denote the decay rates of the optical and nuclear polarizations, respectively; Γ_{12} is the decay rate of the quantum coherence between the ground levels. The rate Γ_{34} is associated to the coherence between levels $|3\rangle$ and $|4\rangle$ and equals $\Gamma_d + \Gamma_p$. The relaxation transition probabilities between the states $|1\rangle$ and $|2\rangle$ are assumed to be small and hence are disregarded in the equations. Typical values of the relaxation rates are given in Table 6.1. The detuning parameters are $\Delta_\eta = \omega_{4\eta} - \omega_p$ and $\delta_\eta = \omega_{3\eta} - \omega_d$.

We shall assume throughout this study that the probe field is too weak to noticeably

perturb the populations. The criterion for a weak probe is thus

$$\boxed{J_p \ll \gamma_p.} \quad (6.21)$$

By extension, since $\gamma_p \leq \Gamma_p \leq \Gamma_{34}$, we also have $J_d \ll \Gamma_p, \Gamma_{34}$.

6.3 Continuous wave amplification and propagation

6.3.1 Amplification mechanism

In this section, we assume constant input fields and study their spatial evolution in the direction of propagation after atoms have reached their steady states. If the drive field is off and no incoherent excitation is applied to the medium, the probe intensity decays exponentially in the direction of propagation. Momentarily neglecting the detunings Δ_η , the associated attenuation coefficient $\alpha_p^{(0)}$, deduced from (6.10), (6.12), and (6.18), is

$$\alpha_p^{(0)} = -\frac{\mathcal{N}\omega_p |\mu_p|^2}{\epsilon_0 \hbar n_p c} \text{Im} \frac{P_p}{\Omega_p} = \frac{\mathcal{N}\omega_p |\mu_p|^2}{\epsilon_0 \hbar n_p c \Gamma_p}. \quad (6.22)$$

In general, we may write the gain of the probe field as

$$\alpha_p = \alpha_p^{(0)} \text{Im} \frac{\Gamma_p P_p}{\Omega_p}. \quad (6.23)$$

Similarly, we define $\alpha_d^{(0)}$ and α_d .

It is important to note that, in the closed system $\{|1\rangle, |2\rangle, |3\rangle, |4\rangle\}$, the state

$$|-\rangle = S_2 |1\rangle - S_1 |2\rangle \quad (6.24)$$

is non absorbent for gamma and optical photons that propagate in the c-direction of the crystal. Because it is decoupled from the electromagnetic field, it is often referred to as the “dark state”. By opposition, its orthogonal counterpart

$$|+\rangle = S_1 |1\rangle + S_2 |2\rangle \quad (6.25)$$

is called the “bright state”*. The amplification of the probe field in the absence of a population inversion between the state $|4\rangle$ and any of the state $|1\rangle$ and $|2\rangle$ becomes possible if part of the ground state population is transferred to the dark state. This amounts to create a coherence ρ_{12} between $|1\rangle$ and $|2\rangle$. Indeed, Eq. (6.18) together with (6.12) and (6.23) yields in steady

*These names are somewhat misleading. Indeed, the state that leaves light unabsorbed, $|-\rangle$, should more sensibly be called “transparent”. As for the state $|+\rangle$, it does absorb light and henceforth should be called “dark”. Whether the commonly accepted terminology is philosophical or psychological is a question that will not be addressed in the present thesis.

state the following expression for the gain:

$$\alpha_p = \alpha_p^{(0)} (\bar{\alpha}_{14} + \bar{\alpha}_{24} + \bar{\alpha}_{34}), \quad (6.26)$$

$$\bar{\alpha}_{14} = \Gamma_p \operatorname{Re} \left[\frac{S_1^2(\rho_{44} - \rho_{11}) - S_1 S_2 \rho_{12}}{\Gamma_p - i\Delta_1} \right], \quad (6.27)$$

$$\bar{\alpha}_{24} = \Gamma_p \operatorname{Re} \left[\frac{S_2^2(\rho_{44} - \rho_{22}) - S_1 S_2 \rho_{21}}{\Gamma_p - i\Delta_2} \right], \quad (6.28)$$

$$\bar{\alpha}_{34} = \Gamma_p \operatorname{Re} \left[\left(\frac{S_1^2}{\Gamma_p - i\Delta_1} + \frac{S_2^2}{\Gamma_p - i\Delta_2} \right) \sigma_{34} \right]. \quad (6.29)$$

The terms $\bar{\alpha}_{14}$ is the contribution of the $1 \leftrightarrow 4$ transition to the gain, while $\bar{\alpha}_{24}$ stems from the $2 \leftrightarrow 4$ transition. Their expressions show that they can both be positive even if $\rho_{44} < \rho_{11}, \rho_{22}$, provided that ρ_{12} is adequately prepared. The last term, $\bar{\alpha}_{34}$, results essentially in a saturation of the gain with respect to the drive intensity.

The quantum coherence between the ground states is produced by the drive field. Through stimulated absorption, it brings the ground state population to the state $|3\rangle$ with a rate that is approximately J_d . This population subsequently comes back into the ground states with a rate γ_d . In this latter process, any superposition of $|1\rangle$ and $|2\rangle$ can be reached, including the dark state. The population that is not in the dark state can again absorb drive photons and, after some cycles, is eventually transferred to the dark state. Stimulated absorption followed by spontaneous emission thus form the mechanism by which coherence is created. The rate of this composite process is the slowest of the rates J_d and γ_d . Simultaneously, ρ_{12} decays spontaneously with a rate Γ_{12} due to parasitic interactions of the nucleus with its environment. Moreover, the states $|1\rangle$ and $|2\rangle$ should be populated simultaneously by the spontaneous decay from level $|3\rangle$. Since, these states have different energies, this decay should be affected by a minimal uncertainty. Specifically, one should have $\hbar J_d, \hbar \gamma_d \gg \epsilon_2 - \epsilon_1$, where ϵ_1 and ϵ_2 are the energies of states $|1\rangle$ and $|2\rangle$, respectively. Introducing the notation

$$J_{12} \equiv \sqrt{\Gamma_{12}^2 + \omega_{21}^2}, \quad (6.30)$$

we are thus led to state the trapping condition

$$J_d, \gamma_d \gg J_{12}. \quad (6.31)$$

This condition is illustrated in Fig. 6.2 where $\alpha_p(\omega_p)$ is plotted for different values of J_d and γ_d . The complete steady state solution of Eqs. (6.13) to (6.19) is computed in Appendix 6.A. The maximal value of the normalized gain approaches the steady state value of ρ_{44} , indicating that the ground state population does not absorb the probe field.

For the chosen set of parameters, Fig. 6.2 indicates that the gain is maximum if the probe detunings $\Delta_{1,2}$ are negligible compared to the linewidth of the nuclear transitions. The same is true for the optical transitions. Therefore, in order to simplify the analysis, we assume in the remainder of this chapter that the detunings are negligible compared to the polarization decay rates:

$$\omega_{21}, |\Delta_\eta|, |\delta_\eta| \ll \Gamma_d, \Gamma_p. \quad (6.32)$$

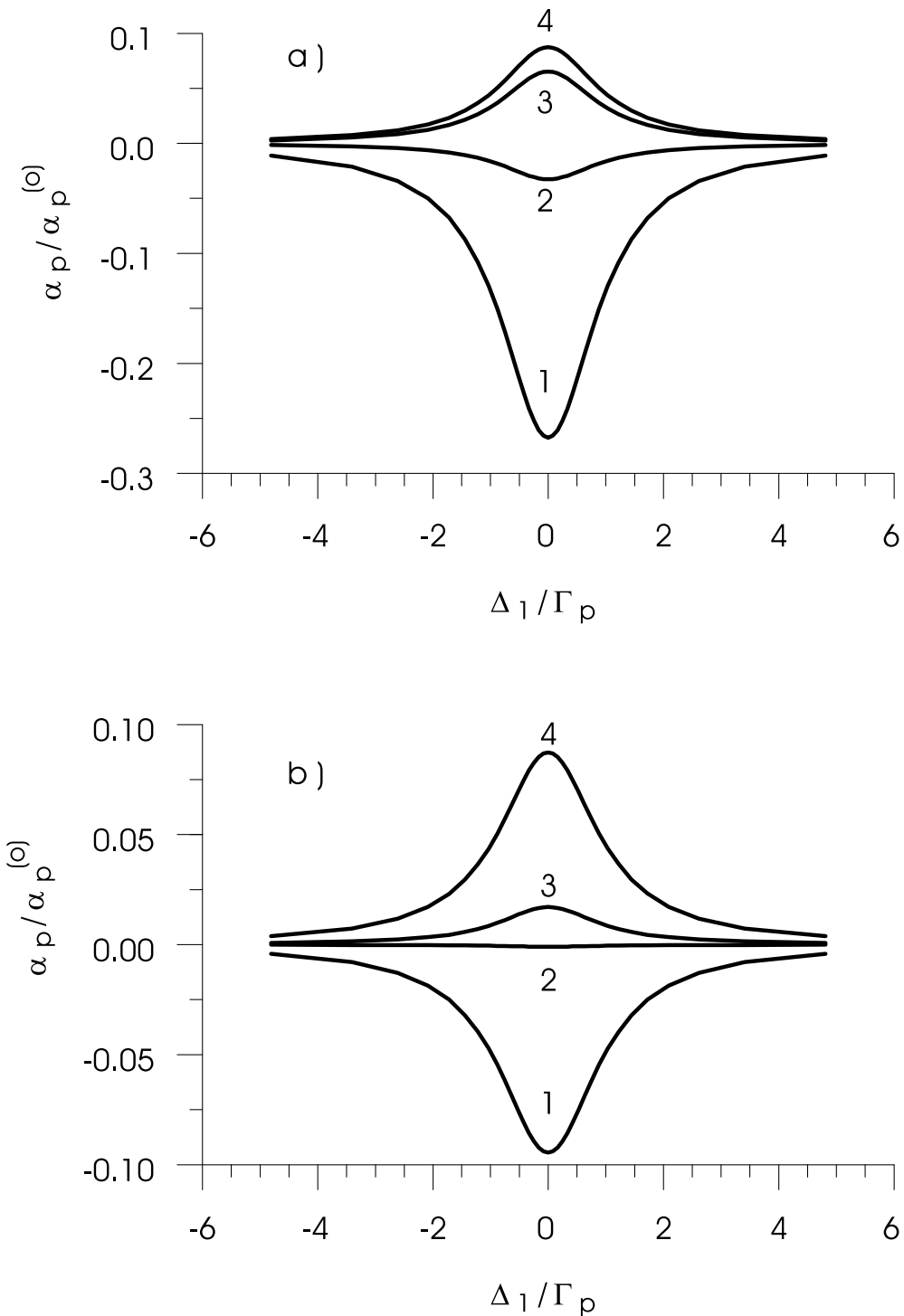


Figure 6.2: spectral gain of the probe intensity α_p normalized by $\alpha_p^{(0)}$. Γ_d , Γ_p , Γ_{12} , ω_{12} , γ_p are given in Table 6.1. $J_{12} \approx 1000 \text{ s}^{-1}$. In Fig. (a), γ_d is fixed to 3000 s^{-1} and Ω_d equals successively, from curve 1 to 4: 2.10^6 s^{-1} , 3.10^6 s^{-1} , 5.10^6 s^{-1} , 10^7 s^{-1} . These values correspond to $J_d = 1300 \text{ s}^{-1}$, 3000 s^{-1} , 8000 s^{-1} , and 33000 s^{-1} , respectively. In Fig. (b), Ω_d is fixed to 10^7 s^{-1} and γ_d equals successively, from curve 1 to 4: 250 s^{-1} , 750 s^{-1} , 1000 s^{-1} , and 3000 s^{-1} .

In addition, we assume for simplicity that $S_1 = -S_2 = -1/\sqrt{2}$. Consequently, by symmetry, if ρ_{11} and ρ_{22} are initially equal, they remain equal for all times. We therefore set

$$\rho_{11} = \rho_{22}. \quad (6.33)$$

Finally, we assume that

$$J_d \ll \Gamma_{34}. \quad (6.34)$$

Inasmuch as $\Gamma_{34} \gg J_{12}$, this assumption is not very restrictive. Under approximations (6.32), (6.33), and (6.34), the polarizations are

$$P_d = -i\Omega_d \frac{n_{13} - \text{Re}\rho_{12}}{\Gamma_d}, \quad (6.35)$$

$$P_p = -i\Omega_p \frac{n_{14} - \text{Re}\rho_{12}}{\Gamma_p (1 + J_d J_{34}^{-1})}, \quad (6.36)$$

$$J_{34} \equiv \Gamma_{34} \Gamma_p \Gamma_d^{-1}. \quad (6.37)$$

As we show it in Appendix 6.A, $\text{Re}\rho_{12}$ tends to a maximum value equal to n_{13} under the influence of the drive field. The absorption of the drive field is thus suppressed while the probe polarization becomes proportional to $i(\rho_{44} - \rho_{33})$. This means that the ultimate condition on gamma amplification rests on population inversion between states $|3\rangle$ and $|4\rangle$. From this fact, the spontaneous decay of ρ_{33} acts in favor of gamma amplification by increasing the population inversion $\rho_{44} - \rho_{33}$. The same inversion condition will be found for adiabatic pulses, for which formula's (6.35) and (6.36) also hold.

6.3.2 Propagation

The steady state solution of Eqs. (6.13) to (6.19) under the approximations (6.32), (6.33), and (6.34) is computed in the Appendix 6.A. Substituting this solution in the field propagation equations (6.10) and (6.11), we obtain:

$$\frac{dJ_d}{dz} = \frac{-\alpha_d^{(0)} \mathcal{F} \gamma_d J_d}{(2+r)\gamma_d + (3+r)\mathcal{F} J_d}, \quad (6.38)$$

$$\frac{dJ_p}{dz} = \frac{\alpha_p^{(0)} [(r-\mathcal{F})\gamma_d - (1-r)\mathcal{F} J_d] J_p}{(1+J_d J_{34}^{-1})[(2+r)\gamma_d + (3+r)\mathcal{F} J_d]}, \quad (6.39)$$

where

$$\mathcal{F} \equiv \frac{\Gamma_{12} J_d + J_{12}^2}{J_d^2 + 2\Gamma_{12} J_d + J_{12}^2}. \quad (6.40)$$

The function \mathcal{F} is connected to the creation of low frequency coherence by

$$\text{Re}\rho_{12} = (1 - \mathcal{F}) n_{13},$$

and varies from 1 to 0 with increasing J_d . The sign of the numerator in Eq. (6.39) determines whether the medium is amplifying or absorbent for the probe field. In the strong drive field

limit $J_d \gg J_{12}$, we note that $\mathcal{F} \rightarrow \Gamma_{12}/J_d$. From this, we deduce the minimum incoherent excitation r_{\min} required for the probe amplification:

$$\lim_{J_d \rightarrow \infty} (r_{\min} - \mathcal{F}) \gamma_d - (1 - r) \mathcal{F} J_d = 0$$

$$\Rightarrow r_{\min} = \frac{\Gamma_{12}}{\Gamma_{12} + \gamma_d}. \quad (6.41)$$

The value of r_{\min} decreases with increasing γ_d , which confirms the beneficial role of the level $|3\rangle$ spontaneous decay in inversionless amplification. Alternatively, one can consider propagation in a medium subjected to uniform incoherent excitation r and calculate the minimum value of the drive intensity J_d^{\min} such that the probe field is amplified

$$(r - \mathcal{F}) \gamma_d - (1 - r) \mathcal{F} J_d = 0$$

$$\Rightarrow J_d = J_d^{\min}(r) \equiv \frac{k_1 + \sqrt{k_3}}{k_2}, \quad (6.42)$$

with

$$\begin{aligned} k_1 &= (1 - r)(2\gamma_d^2 + J_{12}^2) - \gamma_d \Gamma_{12}, \quad k_2 = 2r\gamma_d - 2(1 - r)\Gamma_{12}, \\ k_3 &= 4(1 - r)[r\gamma_d - (1 - r)\Gamma_{12}] \gamma_d J_{12}^2 + [(2r - 1)\gamma_d \Gamma_{12} - (1 - r)J_{12}^2]^2. \end{aligned} \quad (6.43)$$

Considering Eqs. (6.38) and (6.39), we note that $\frac{dz}{dJ_d}$ and $\frac{dJ_p}{dJ_d}$ are analytically integrable with respect to J_d . The knowledge of J_d^{\min} then allows us to compute the maximum amplification length z^{\max} and the corresponding probe intensity J_p^{\max} . Given the input intensities J_d^{in} and J_p^{in} and the incoherent excitation r , we obtain

$$\begin{aligned} \alpha_d^{(0)} z^{\max} &= \left(\frac{3+r}{\gamma_d} + \frac{2+r}{\Gamma_{12}} \right) (J_d^{in} - J_d^{\min}) \\ &\quad + (2+r) \left(\ln \frac{J_d^{in}}{J_d^{\min}} - \frac{\omega_{21}^2}{\Gamma_{12}} \ln \frac{J_{12}^2 + \Gamma_{12} J_d^{in}}{J_{12}^2 + \Gamma_{12} J_d^{\min}} \right), \end{aligned} \quad (6.44)$$

$$\frac{\alpha_d^{(0)}}{\alpha_p^{(0)}} \ln \frac{J_p^{\max}}{J_p^{in}} = l_1 \ln \frac{J_d^{in}}{J_d^{\min}} + l_2 \ln \frac{J_{34} + J_d^{in}}{J_{34} + J_d^{\min}} + l_3 \ln \frac{J_{12}^2 + \Gamma_{12} J_d^{in}}{J_{12}^2 + \Gamma_{12} J_d^{\min}}. \quad (6.45)$$

The coefficients l_j in (6.45) are given by

$$l_1 = r - 1, \quad l_2 = \frac{(1 - r)(\gamma_d - J_{34})}{\gamma_d} + \frac{J_{34}^2 - J_{34}\Gamma_{12}}{J_{34}\Gamma_{12} - J_{12}^2}, \quad l_3 = \frac{-rJ_{34}\omega_{21}^2}{\Gamma_{12}(J_{34}\Gamma_{12} - J_{12}^2)}. \quad (6.46)$$

This solution is illustrated in Fig. 6.3. Since the criterion of an efficient drive is $J_d \gg J_{12}$, the stimulated transition rate J_d is scaled to J_{12} . To interpret the formulas (6.44) and (6.45), let us suppose that the input drive field intensity is much larger than J_{12} and J_d^{\min} . The first term in the right hand side of Eq. (6.44) is then dominant, indicating that the optimal length scales linearly with the input drive intensity. This follows from the fact that each segment of the medium dissipates a certain amount of energy as it reaches the dark state. Once in the

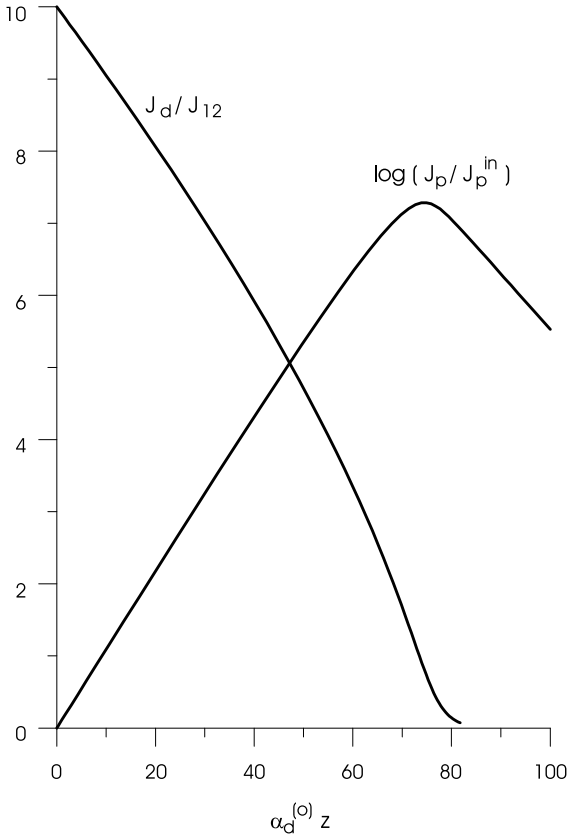


Figure 6.3: Steady state intensity versus distance of propagation. The drive field intensity is rescaled to J_{12} . Initial condition: $J_d^{in} = 10J_{12}$. Incoherent excitation $r = R/\gamma_p = 0.6$. The propagation constants are taken equal: $\alpha_p^{(0)} = \alpha_d^{(0)}$. The other parameters are given in Table 6.1.

dark state, the medium becomes transparent to the drive beam anymore, while it amplifies the probe beam through the population in $|4\rangle$. Supposing in addition that $J_d^{in} \ll J_{34}$, the right hand side of the probe propagation equation (6.39) becomes independent of J_d and the probe intensity grows exponentially up to $z = z^{\max}$. This yields

$$J_p^{\max} = J_p(z^{\max}) \sim J_p^{in} \exp \left[\frac{\alpha_p^{(0)}}{\alpha_d^{(0)}} \left(\frac{r}{\Gamma_{12}} - \frac{1-r}{\gamma_d} \right) (J_d^{in} - J_d^{\min}) \right]. \quad (6.47)$$

This last formula shows that the maximum probe field depends exponentially on the input drive intensity. This conclusion holds as long as the probe field is weak in the sense given by (6.21).

6.4 Adiabatic pulse amplification

We now examine the dynamical response of the medium to a drive pulse of duration τ that is short compared to the atomic population lifetime, while sufficiently long to justify the adiabatic elimination of the polarizations P_d and P_p . Specifically, with the average input intensity $\langle J_d \rangle$ defined as $\tau^{-1} \int_{-\infty}^{\infty} J_d(0, t') dt'$, we assume that

$$\Gamma_{12}, \omega_{12}, \gamma_d \ll \tau^{-1}, \langle J_d \rangle \ll \Gamma_d, \Gamma_{34}, J_{34}. \quad (6.48)$$

Initially, the populations are distributed according to the incoherent excitation and the quantum coherences vanish:

$$\rho_{11}^0 = \rho_{22}^0 = \frac{1}{2+r}, \quad \rho_{44}^0 = \frac{r}{2+r}, \quad \rho_{33}^0 = \rho_{12}^0 = \sigma_{ij}^0 = 0. \quad (6.49)$$

Substituting (6.35) in Eqs. (6.13) to (6.16) and making use of approximation (6.48), we find that

$$\frac{n_{13} - \text{Re}\rho_{12}}{n_{13}^0 - \text{Re}\rho_{12}^0} = \exp\left(-4 \int_{-\infty}^t J_d(z, t') dt'\right) \equiv \mathcal{K}(z, t). \quad (6.50)$$

The function \mathcal{K} measures the degree of quantum coherence produced by the driving field. It indicates that the low frequency coherence $\text{Re}\rho_{12}$ tends a maximum value equal to n_{13} at a rate $\mathcal{K}^{-1} \partial \mathcal{K} / \partial t = -4J_d(z, t)$. From (6.35) and (6.36), the absorption of the drive field is thus suppressed while the probe polarization becomes proportional to $i(\rho_{44} - \rho_{33})$. In the present situation, the creation of the dark state is a purely stimulated process, since its rate is proportional to the number of photons in the drive field. Maximum quantum interference is produced if $\mathcal{K} \ll 1$. The details of this process are most easily understood in the basis formed by the dark and bright states $|-\rangle$ and $|+\rangle$. Initially, there is equipartition of the population in these two states, so that $\rho_{12} = 0$. The drive field J_d excites population from state $|+\rangle$ to state $|3\rangle$, leaving $|-\rangle$ unaffected. For a sufficiently intense drive field, the states $|+\rangle$ and $|3\rangle$ become equipopulated. In this way, the fraction of the ground state population prepared in the dark state $|-\rangle$ by the drive field is maximized. This results in an increase of the low frequency coherence $\text{Re}\rho_{12}$.

By substituting the time dependent solution of Eqs. (6.13) to (6.19) into the field equation (6.10) and (6.11), we get:

$$\left(\frac{\partial}{\partial z} + \frac{n_d}{c} \frac{\partial}{\partial t}\right) J_d = \frac{-\alpha_d^{(0)} \mathcal{K} J_d}{2+r}, \quad (6.51)$$

$$\left(\frac{\partial}{\partial z} + \frac{n_p}{c} \frac{\partial}{\partial t}\right) J_p = \frac{\alpha_p^{(0)} (2r - 1 - \mathcal{K}) J_p}{2(2+r)}, \quad (6.52)$$

The propagation equation for the drive field J_d was already analyzed in [4]. It has the solution

$$J_d(z, t) = \frac{J_d(0, t - \frac{n_d}{c} z)}{1 + \left[\exp\left(\frac{2}{2+r} \alpha_d^{(0)} z\right) - 1\right] \mathcal{K}(0, t - \frac{n_d}{c} z)}, \quad (6.53)$$

which is used to solve Eq. (6.52). If the probe and drive pulse propagate at the same velocity, $n_d = n_p$, we find an analytical solution for the probe pulse

$$J_p(z, t) = \frac{J_p(0, t - \frac{n_d}{c} z) \exp\left(\frac{r-1/2}{2+r} \alpha_p^{(0)} z\right)}{\left\{1 + \left[\exp\left(\frac{1}{2+r} \alpha_d^{(0)} z\right) - 1\right] \mathcal{K}(0, t - \frac{n_d}{c} z)\right\}^{\alpha_p^{(0)} / (2\alpha_d^{(0)})}}. \quad (6.54)$$

This solution is illustrated in Fig. 6.4. If the coherence between the ground levels is maximum, $\mathcal{K} \ll 1$, it follows from Eq. (6.54) that $J_p(z) \simeq J_p(0) \exp\left(\frac{r-1/2}{2+r} \kappa_p z\right)$. Therefore r must at least exceed $1/2$ in order to obtain amplification, which means $\rho_{44}^0 > 0.2$. Although this result is significant from the point of view of amplification without inversion, it might not be sufficient in practice. Indeed, if one can bring 20% of the population in level $|4\rangle$ without damage for the amplifying medium, then one can probably create an inversion of population too.

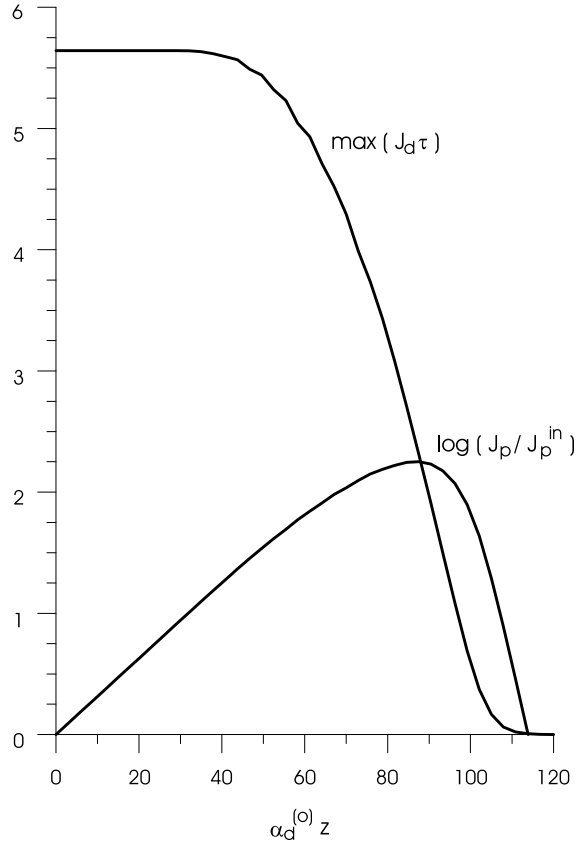


Figure 6.4: Peak intensity as a function of the propagation distance in the adiabatic pulse regime. Input condition: $\int_{-\infty}^{+\infty} J_d(0, t) dt = 10$. Same parameters as in Fig. 6.3.

6.5 Ultrashort pulse amplification

Another regime of propagation exists if the pulse duration is shorter than all other characteristic times. The electro-nuclear scheme then becomes an effective *V*-scheme, composed of the states $|3\rangle$ and $|4\rangle$ as the excited states and the bright state $|+\rangle = (|1\rangle - |2\rangle)/\sqrt{2}$ as the ground state (see Fig. 6.5). The propagation of ultrashort pulses in such a scheme was analyzed in [24]. The population in the bright state is given by

$$\rho_{++} = \frac{1}{2} (\rho_{11} + \rho_{22} - \rho_{12} - \rho_{21}).$$

In the weak probe limit and neglecting all relaxation processes in Eqs. (6.13) to (6.19), we obtain for the drive field the closed set of equations

$$\begin{aligned} \frac{\partial}{\partial t} (\rho_{33} - \rho_{++}) &= -4\Omega_d(z, t) \text{Im}P_d, \\ \frac{\partial}{\partial t} \text{Im}P_d &= \Omega_d(z, t) (\rho_{33} - \rho_{++}). \end{aligned}$$

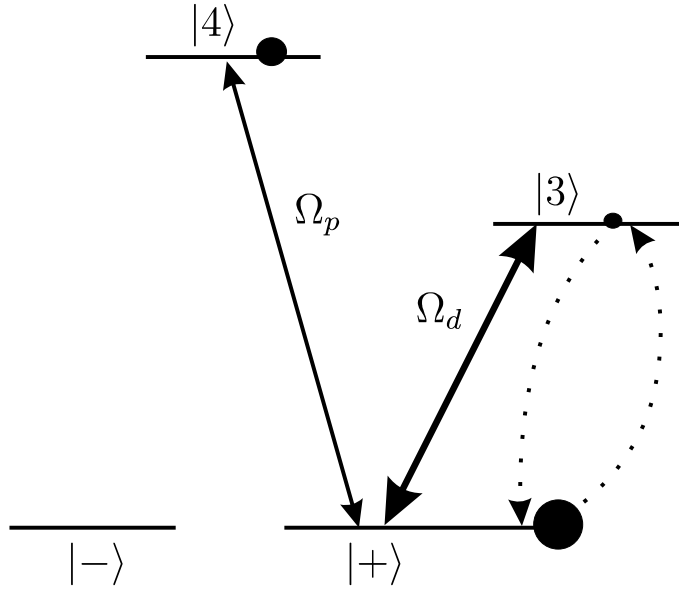


Figure 6.5: Reduced level scheme for ultrashort pulses. States $|3\rangle$ and $|4\rangle$ are coupled to state $|+\rangle$ only. The resonant drive field induces cyclic exchange of population between states $|3\rangle$ and $|+\rangle$. These are the Rabi oscillations.

These equations are identical to those governing the resonant interaction of an electromagnetic field with a two-level system. The solution is

$$\rho_{33} - \rho_{++} = (\rho_{33}^0 - \rho_{++}^0) \cos \theta_d(z, t), \quad (6.55)$$

$$\text{Im}P_d = (\rho_{33}^0 - \rho_{++}^0) \sin \theta_d(z, t), \quad (6.56)$$

where ρ_{33}^0 and ρ_{++}^0 denote the initial state of the electro-nuclear system and

$$\theta_d(z, t) = \int_{-\infty}^t 2\Omega_d(z, t') dt'. \quad (6.57)$$

The solution (6.55) shows that the population flows in a cyclic way between the states $|+\rangle$ and $|3\rangle$, with an instantaneous frequency $2\Omega_d(z, t)$. These are the “Rabi oscillations”. The factor 2 in $2\Omega_d(z, t)$ is related to the way we have defined E_d and E_p in (6.7). The variable $\theta_d(z, t)$ is the area of the drive field. If the total area of the pulse, $\theta_d(z, \infty)$, is 2π , then the medium is in the same state prior and after the passage of the pulse. In this case, the net exchange of energy between the drive field and the medium vanishes, which renders possible the lossless propagation of the drive pulse. This phenomenon is called Self-Induced-Transparency (SIT) [25]. When the pulse area is π , the population in the bright state is temporarily ρ_{33}^0 , so that the population inversion between the states $|4\rangle$ and $|+\rangle$ is $\rho_{44}^0 - \rho_{33}^0$. This allows to open a temporal window of population inversion on the probe transition, as fully described in [24]. It was numerically shown in [24] that eventually all the drive photons can be converted into probe photons, with the conservation of energy being assured by the inversion $\rho_{44}^0 - \rho_{33}^0$. There is, however, a dynamical limitation on the number of photons that

can propagate in a single pulse. The equation for the drive field can be written as

$$\frac{\partial^2 \theta_d(\xi, \eta)}{\partial \xi \partial \eta} = \Gamma_d \alpha_d^{(0)} (\rho_{33}^0 - \rho_{++}^0) \sin \theta_d(\xi, \eta). \quad (6.58)$$

$$\xi = z, \quad \eta = z - \frac{c}{n_d} t.$$

This equation, known as the Sine-Gordon equation, possesses soliton solutions having a total area equal to $0, 2\pi, 4\pi, 6\pi \dots$ [26]. Among these, only the 2π -area solution consists of a single pulse. If, initially, the drive area well exceeds 2π , the pulse breaks up in multiple 2π -area pulses in the course of propagation, each giving rise to a separate probe pulse. Furthermore, since the velocity of each pulse depends on its peak intensity, light can be expected to exit the amplifying medium in a very irregular fashion. Finally, we note that, as all the pump photons of a pulse are transformed into probe photons, the field resonant with the $+ \rightleftharpoons 4$ transition becomes a drive field for the $+ \rightleftharpoons 3$ transition. The flow of energy between the fields can thus be reversed for long propagation distances.

6.6 Summary and Conclusion

In view of applying the principles of quantum interference to gamma amplification, we have studied an electro-nuclear system. We have shown that the Hyperfine interaction allows to couple the nucleus with its electron shell. Thanks to this coupling, it is possible to create the necessary nuclear coherence for Amplification Without Inversion by the application of an optical “drive” field. In the continuous wave limit, stimulated absorption of the drive photons and spontaneous emission form a composite process by which the ground state is trapped into the non absorbent state. A simple condition was found for efficient population trapping

$$J_d, \gamma_d \gg J_{12}.$$

In addition, the minimum rate of incoherent nuclear excitation was found to be

$$r_{\min} = \frac{R_{\min}}{\gamma_p} = \frac{\Gamma_{12}}{\Gamma_{12} + \gamma_d}.$$

Furthermore, we showed that the optimal amplification length is in first approximation proportional to the input drive intensity. Since a weak “probe” gamma field grows exponentially with distance, the maximum output gamma intensity scales exponentially with the input drive intensity.

Next, we have studied the propagation of pulses of duration τ . The case $\tau^{-1} \ll \Gamma_{12}, \gamma_d, \gamma_p$ corresponds approximately to a continuous wave and has just been discussed. In the case of adiabatic pulses, τ is intermediate between the populations and the polarizations lifetimes. The mechanism of inversionless amplification is essentially the same as before. Indeed, Figs. 6.3 and 6.4 illustrate qualitatively similar propagation behaviors in the cw and adiabatic pulse regimes, respectively. However, the spontaneous decay of the atomic excited state is negligible over the duration of the adiabatic pulse, which makes population trapping less efficient. The minimum pump rate is, in this regime of propagation, $r_{\min} = 0.5$. Accordingly, at least 20% of population should be in the state 4, but if this was technically possible, then a population inversion would be feasible too.

Comparing continuous waves with ultrashort pulses, the ultimate amplification condition is in both cases to have a population inversion between the upper states $|3\rangle$ and $|4\rangle$. While population is driven irreversibly to the dark state in the cw regime, it flows periodically between states $|+\rangle$ and $|3\rangle$ in the latter regime, at the instantaneous frequency $2\Omega_d$. The periodic exchange of population between states $|+\rangle$ and $|3\rangle$, or Rabi oscillations, temporarily establishes an inversion $\rho_{44}^0 - \rho_{33}^0$ on the probed transition. Short pulse propagation benefits from the distortionless Self-Induced Transparency. However, we pointed out that the maximum amount of energy that can be obtained in a single probe pulse is limited by the 2π -area of the drive pulse. This limitation does not exist in the cw regime.

The best way to amplify gamma photon by stimulated emission seems therefore to resort to continuous waves. It is now the turn of nuclear physicists to find a nucleus that fits the scheme in Fig.6.1.

Appendix to Chapter 6

6.A Steady state solution

In this Appendix, we derive the steady state response of the electro-nuclear system. Setting the time-derivatives to zero in Eqs. (6.13) to (6.19), we get an algebraic system to solve. To this end, it is convenient to introduce the Lorentzian factors

$$\begin{aligned}\mathcal{L}_{\eta 3} &\equiv \frac{\Gamma_d}{\Gamma_d - i\delta_\eta}, \quad \mathcal{L}_{\eta 4} \equiv \frac{\Gamma_p}{\Gamma_p - i\Delta_j}, \quad \mathcal{L}_{34} \equiv \frac{\Gamma_{34}}{\Gamma_{34} + i(\delta_1 - \Delta_1)}, \\ \mathcal{L}_{12} &\equiv \frac{\Gamma_{12}}{\Gamma_{12} + i\omega_{12}}, \quad \mathcal{L}_{ji} \equiv \mathcal{L}_{ji}^*\end{aligned}\quad (6.59)$$

Working in the weak probe limit, we neglect quadratic terms in Ω_p . Solving successively Eqs. (6.19), (6.18) and (6.17) then gives:

$$P_p = -i\frac{\Omega_p}{\Gamma_p} \mathcal{L}_p \sum_{\eta=1,2} \left(S_\eta^2 \mathcal{L}_{\eta 4} n_{\eta 4} + S_\eta S_{\eta'} \mathcal{L}_{\eta 4} \rho_{\eta \eta'} + S_\eta^2 \mathcal{L}_{\eta 4} \mathcal{L}_{34} \frac{\Omega_d P_d^*}{\Gamma_{34}} \right), \quad (6.60)$$

$$P_d = -i\frac{\Omega_d}{\Gamma_d} \sum_{\eta=1,2} (S_\eta^2 \mathcal{L}_{\eta 3} n_{\eta 3} + S_\eta S_{\eta'} \mathcal{L}_{\eta 3} \rho_{\eta \eta'}), \quad (6.61)$$

where

$$\mathcal{L}_p \equiv \frac{1}{1 + \sum_{\eta=1,2} S_\eta^2 \mathcal{L}_{\eta 4} \mathcal{L}_{34} J_d / J_{34}}, \quad J_{34} \equiv \frac{\Gamma_{34} \Gamma_p}{\Gamma_d}. \quad (6.62)$$

Substituting the expression of the polarization into Eqs. (6.13) to (6.16) we are left with

$$1 = \rho_{11} + \rho_{22} + \rho_{33} + \rho_{44}, \quad (6.63)$$

$$0 = -R\rho_{\eta\eta} + \gamma_p \rho_{44} + \gamma_d \rho_{33} - 2J_d \operatorname{Re} [\mathcal{L}_{\eta 3} (S_\eta^2 n_{\eta 3} + S_\eta S_{\eta'} \rho_{\eta \eta'})], \quad (6.64)$$

$$0 = -\gamma_d \rho_{33} + J_d \operatorname{Re} \left[\sum_{\eta=1,2} \mathcal{L}_{\eta 3} (S_\eta^2 n_{\eta 3} + S_\eta S_{\eta'} \rho_{\eta \eta'}) \right], \quad (6.65)$$

$$0 = -2\gamma_p \rho_{44} + R \sum_{\eta=1,2} \rho_{\eta\eta}, \quad (6.66)$$

$$\rho_{12} = -\frac{\mathcal{L}_{12} J_d \sum_{\eta=1,2} S_\eta S_{\eta'} \mathcal{L}_{\eta 3} n_{\eta 3}}{\Gamma_{12} + \mathcal{L}_{12} \sum_{\eta=1,2} S_\eta^2 \mathcal{L}_{\eta 3} J_d}. \quad (6.67)$$

We solved the set of Eqs. (6.63) to (6.67) numerically for different values of the detuning parameters. Using expressions (6.60) and (6.23), we then evaluated α_p and obtained Fig. 6.2.

Next, we consider the limits $|\Delta_\eta|, |\delta_\eta| \ll \Gamma_d, \Gamma_p$, which implies $\mathcal{L}_{\eta 4}, \mathcal{L}_{\eta 3} \simeq 1$. Supposing for simplicity that $S_1^2 = S_2^2 = -S_1 S_2 = 1/2$, the polarizations become

$$P_p = -i \frac{\Omega_p}{\Gamma_p} \left[n_{14} - \operatorname{Re} \rho_{12} + O\left(\frac{J_d}{\Gamma_{34}}, \frac{J_d}{J_{34}}\right) \right], \quad (6.68)$$

$$P_d = -i \frac{\Omega_d}{\Gamma_d} (n_{13} - \operatorname{Re} \rho_{12}). \quad (6.69)$$

On the other hand, the system of Eqs. (6.63) to (6.67) reduces to

$$\begin{aligned} \rho_{11} &= \rho_{22}, \quad \rho_{44} = r \rho_{11}, \quad 1 = 2\rho_{11} + \rho_{33} + \rho_{44}, \\ \gamma_d \rho_{33} &= J_d \mathcal{F} n_{13}, \quad \operatorname{Re} \rho_{12} = (1 - \mathcal{F}) n_{13}, \end{aligned} \quad (6.70)$$

with

$$\mathcal{F} \equiv \frac{\Gamma_{12} J_d + J_{12}^2}{J_d^2 + 2\Gamma_{12} J_d + J_{12}^2}, \quad J_{12} \equiv \sqrt{\Gamma_{12}^2 + \omega_{21}^2}. \quad (6.71)$$

It is thus easy to compute n_{13} , n_{14} , and $\operatorname{Re} \rho_{12}$, and then P_d and P_p to derive the propagation equations (6.38) and (6.39). Let us note that, by substituting the last relation of (6.70) in (6.68) and considering the limit $\mathcal{F} \rightarrow 0$, the gain condition in steady state becomes:

$$\rho_{44} - \rho_{33} > 0.$$

References

- [1] G. C. Baldwin and J. C. Solem, Rev. Mod. Phys. **69**, 1085 (1997).
- [2] J. Mompart and R. Corbalán, J. Opt. B: Quantum Semiclass. Opt. **2**, R7 (2000).
- [3] S. E. Harris, Phys. Rev. Lett. **62**, 1033 (1989).
- [4] O. A. Kocharovskaya and Ya. I. Khanin, Sov. Phys. JETP Lett. **48**, 630 (1989).
- [5] M. O. Scully, S.-Y. Zhu, and A. Gavrielides, Phys. Rev. Lett. **62**, 2813(1989).
- [6] A. Nottelmann, C. Peters and W. Lange, Phys. Rev. Lett. **70**, 1783 (1993).
- [7] E.S. Fry, X. Li, D. Nikonov, G.G. Padmabandu, M.O. Scully, A.V. Smith, F.K. Tittel, C. Wang, S.R. Wilkinson and S.-Y. Zhu, Phys. Rev. Lett. **70**, 3235 (1993).
- [8] W.E. van der Veer, R.J.J. van Diest, A. Dönszelmann and H.B. van Linden van den Heuvell, Phys. Rev. Lett. **70**, 3243 (1993).
- [9] J.A. Kleinfeld and D.A. Streater Phys.Rev. A **49**, 4301 (1994).
- [10] A.S. Zibrov, M.D. Lukin, D.E. Nikonov, L. Hollberg, M.O. Scully, V.L. Velichansky and H.G. Robinson, Phys. Rev. Lett. **75**, 1499 (1995).
- [11] G.G. Padmabandu, G.R. Welch, I.N. Shubin, E.S. Fry, D.E. Nikonov, M.D. Lukin and M.O. Scully, Phys. Rev. Lett. **76**, 2053(1996).
- [12] C. Peters and W. Lange, Appl. Phys. B **62**, 221 (1996).
- [13] C. Fort, F.S. Cataliotti, T.W. Hänsch, M. Ingucio and M. Prevedelli, Opt. Commun. **139**, 31 (1997).
- [14] R. Coussement, M. Van den Bergh, G. S'heeren, G. Neyens, R. Nouwen, P. Boolchand, Phys. Rev. Lett. **71**, 1824 (1993).
- [15] J. Odeurs, R. Coussement, and G. Neyens, Proc. Int. Conf. on Lasers, Ed. V. J. Corcoran, T. A. Goldman, STS Press, McLean, 1997, p. 266.
- [16] N. N. Greenwood and T. C. Gibb, Mössbauer Spectroscopy, Chapman and Hall, 1971.
- [17] O. A. Kocharovskaya, R. Kolesov, and Y. Rostovstev, Phys. Rev. Lett. **82**, 3593 (1999).
- [18] J. Mompart, V. Ahufinger, R. Corbalán, and F. Prati, J. Opt. B: Quantum Semiclass. Opt. **2**, 359 (2000).
- [19] R. N. Shakhmuratov, G. Kozyreff, R. Coussement, J. Odeurs, and P. Mandel, Opt. Comm. **179**, 525 (2000).
- [20] G. Kozyreff, R. N. Shakhmuratov, J. Odeurs, R. Coussement, and P. Mandel, Phy. Rev. A (2001), in press.

- [21] F. Hardeman, G. Schevemeels, G. Neyens, R. Nouwen, and R. Coussement, *Hyperfine Interactions* **59**, 13 (1990).
- [22] C. Cohen-Tanoudji, B. Diu, and F. Laloë, *Mécanique Quantique II* (Hermann 1993), p. 1211.
- [23] A. E. Siegman, *Lasers* (University Sciences Books, 1986), p. 131.
- [24] V.V. Kozlov, P.G. Polynkin, and M.O. Scully, *Phys. Rev. A* **59**, 3060 (1999).
- [25] S.L. McCall and E.L. Hahn, *Phys. Review* **183**, 457 (1968).
- [26] G.L. Lamb Jr, *Element of soliton theory* (Wiley, New York, 1980).

Chapter 7

Conclusions

In this thesis, we have analyzed laser problems using methods that were developed in the wider scope of nonlinear science. Being eventually confronted with sets of nonlinear differential equations to solve, we have each time pointed out their underlying physical meaning. Let us review our main results.

In our study of a microchip laser with a weakly saturable absorber (LSA), we characterized the bifurcation layer over which harmonic intensity oscillations evolve into pulsating oscillations. In particular, we determined the dependence of the size of this bifurcation layer on the laser parameters. We could therefore indicate ways to design a microchip LSA with a sufficiently smooth bifurcation layer to be experimentally studied. A potential advantage of this would be the ability to tune the shape of the intensity pulse via the pump parameter. From a fundamental viewpoint, we showed that the underlying LSA dynamics close to the Hopf bifurcation is intimately related to the Lotka-Volterra problem, which is well known in ecology and chemistry. This is also the first example of a singular Hopf bifurcation in a laser system. The LSA problem dramatically illustrates how the gain dynamics can disturb the quiet behavior of a laser.

In a free-running multimode laser with spatially modulated pump, part of the medium may act as a saturable absorber. If the laser operates in the multimode regime, a similar self-pulsing behavior as in the microchip LSA can arise. Here again, the transition from harmonic to pulsating oscillations occurs over a very small range of parameters, although not as abruptly as in the LSA case. Viewed as individual oscillators, the lasing cavity modes are globally coupled by the mean longitudinal gain. This gives rise to antiphase dynamics, resulting in a smoother behavior in the total intensity output than in each modal intensity. An interesting continuation of this work would be to study to which extend such a self-organization survives in the self-pulsating domain of this system. Preliminary numerical simulations seem to indicate that this property is very robust. This suggests to design highly multimode self-pulsating lasers that function on the present mechanism. The required strong spatial modulation of the pump could easily be achieved with semiconductor lasers. Another consequence of an inhomogeneous gain distribution over the cavity axis is the existence of bistability between steady states.

After having encountered the antiphase type of synchronization in multimode lasers, we studied the conditions for in-phase synchronization in a semiconductor laser (SCL) array with an external mirror. A connection was found with the Kuramoto set of equations, which is a generic model for globally coupled oscillators. We extended this model to investigate the

synchronization properties of the array with respect to both optical and relaxation oscillations. The time delay is found to produce many solutions, all displaying in-phase synchronization. These solutions can be viewed as nonlinear modes of the composite cavity formed by the SCL array and the external mirror. Indeed, they satisfy resonance conditions expressed by transcendental equations for the optical and relaxation frequency. The number of nonlinear in-phase modes increases with the external cavity length, which favors in-phase synchronization both in steady and time-dependent states. They are analog, though different, to the linear eigenmodes of the composite cavity in the absence of the semiconductor material. Therefore, using an external cavity, one can improve the beam quality obtained from a SCL array and broaden its range of applications. In the future, it would be interesting to investigate the array dynamics for larger coupling strength. This would allow to achieve in-phase synchronization with broader distributions of natural optical frequencies in the array. Another direction of research would be to study the dynamics of a broad area laser with the same coupling scheme.

Following the idea that low frequency atomic coherence effects could play a role in the dynamics of the microchip LNP laser, we built a theory for a multi-transition laser. We derived the minimal set of equations to describe these effects and gave them a physical interpretation: the multimode electromagnetic field brings the ground state population into a quantum superposition of states where stimulated absorption is enhanced. The resulting model explains the experimentally observed oscillatory output of the LNP laser. Recently, this model was successfully used to describe an experiment carried out on a microchip LNP laser with a KTP frequency-doubling crystal.

Finally, we have derived the necessary conditions to achieve inversionless amplification of gamma radiation in an electro-nuclear scheme. These conditions involve not only the intensity of an optical drive field, but also impose constraints on the characteristic decay rates of the medium. If these conditions are fulfilled, the required pump power can be decreased by orders of magnitudes with respect to conventional laser systems. It remains to find a Mössbauer nuclear candidate that matches these conditions. This would pave the way to the construction of the first gamma ray-laser.

By this work, we hope to have convinced the reader that nonlinear aspects are not only of fundamental but also of practical importance in dealing with light-matter interaction. Through a proper comprehension and characterization of the related phenomena, we have shown on multiple instances that new or better coherent optical sources can be developed.